



UNIVERSITAT POLITÈCNICA DE CATALUNYA  
BARCELONATECH

Departament de Teoria del Senyal  
i Comunicacions

---

# Mobile 5G Millimeter-wave Multi-antenna Systems

---

Ph.D. Thesis

*Author:* Christian Ballesteros Sánchez



*Thesis director:* Luis Jofre Roca

*A thesis submitted as a compendium of publications in fulfillment of the requirements of the Signal Theory and Communications program from the Universitat Politècnica de Catalunya (UPC)*

On June, 2022

## Abstract

Massive antenna architectures and millimeter-wave bands appear on the horizon as the enabling technologies of future broadband wireless links, promising unprecedented spectral efficiency and data rates. In the recently launched fifth generation of mobile communications, millimetric bands are already introduced but their widespread deployment still presents several feasibility issues.

In particular, high-mobility environments represent the most challenging scenario when dealing with directive patterns, which are essential for the adequate reception of signals at those bands. Vehicular communications are expected to exploit the full potential of future generations due to the massive number of connected users and stringent requirements in terms of reliability, latency, and throughput while moving at high speeds. This thesis proposes two solutions to completely take advantage of multi-antenna systems in those cases: beamwidth adaptation of cellular stations when tracking vehicular users based on positioning and Doppler information and a tailored radiation diagram from a panel-based system of antennas mounted on the vehicle.

Apart from cellular base stations and vehicles, a third entity that cannot be forgotten in future mobile communications are pedestrians. Past generations were developed around the figure of human users and, now, they must still be able to seamlessly connect with any other user of the network and exploit the new capabilities promised by 5G. The use of millimeter-waves is already been considered by handset manufacturers but the impact of the user (and the interaction with the phone) is drastically changed. The last part of this thesis is devoted to the study of human user dynamics and how they influence the achievable coverage with different distributed antenna systems on the phone.

## Acknowledgements

This thesis would not have been possible without the effort and involvement of many people to some extent. Completing a Ph.D. is a large journey in which you may encounter difficulties and tasks you cannot overcome alone. In the following lines, I would like to thank all those people who helped me during the last four years.

First, my supervisor and thesis director, Prof. Luis Jofre Roca. We had many interesting discussions and I have learned more than I ever thought, not only about antennas but also about many aspects to apply in my academic and professional life. I would also like to thank the rest of professors from our research group. You all contributed to this thesis: Profs. Jordi Romeu, Sebastián Blanch, Juan Manuel Rius, Maria Concepción (Conchi) Santos, and Lluís Pradell. Also the technical staff that suffered us with impossible designs but they always found the best solution

Thank you to the Department of Electronics and Nanoengineering (ELE) from Aalto University for letting me spend three months there with Prof. Katsuyuki Haneda, D.Sc. Clemens Icheln and many team mates that helped me enjoying that time in Finland as I was at home. I want also to thank the Fraunhofer Heinrich-Hertz-Institut, and in particular Dr.-Ing. Michael Peter, Dr.-Ing. Lars Thiele, and the mm-Wave group. Despite the bad times, I really felt part of the team during my stay in Berlin.

I cannot forget my friends and colleagues in Barcelona. Other Ph.D. students that, like me, suffer the same issues every day. The pandemic sent us home and it was difficult to keep in touch sometimes, but we managed to create a very nice team. And, as soon as things were getting back to normal, we could recover our lunch time together and other team building activities (now you all know how to eat calçots).

The last paragraph is devoted to those who know me better and have to suffer me at home. My family, and in particular my mum, have raised me to be who I am today. They taught me the value of doing your best on everything you do and stay always humble. But life is unexpected. Just started my thesis, my world went upside-down and a new person showed me the so many colors and views you can see in everything. My partner in life, Alejandra, deserves the best of prizes for helping me during my bluest times and sharing always the biggest smile to make my day shine again.

# CONTENTS

---

<b>Abstract</b>	<b>ii</b>
<b>Acknowledgements</b>	<b>iii</b>
<b>Research Outcome</b>	<b>vii</b>
<b>List of Figures</b>	<b>ix</b>
<b>List of Tables</b>	<b>xi</b>
<b>Glossary</b>	<b>xi</b>
<b>1 Introduction</b>	<b>1</b>
1.1 Framework of the Thesis . . . . .	1
1.2 Motivation and Background . . . . .	2
1.3 Objectives . . . . .	6
1.3.1 Hypotheses . . . . .	7
1.4 Contributions and Thesis Structure . . . . .	8
<b>2 The Journey Towards mmWave Mobile Connectivity</b>	<b>10</b>
2.1 A Not-so-Brief History of mmWave Research . . . . .	10
2.2 Mobility in Future Cities Will Be Connected or Won't Be . . . . .	12
2.3 The Landscape of Standardization: WiFi, 5G, and Beyond . . . . .	16
2.3.1 The New Generation of Cellular Communications . . . . .	16
2.3.2 Standardization in the World of Vehicular Communications . . . . .	19
2.4 Beamforming in 5G Networks . . . . .	23
2.4.1 Synchronization signals . . . . .	25
2.4.2 Channel-state information signals . . . . .	25

<b>3</b>	<b>Modeling Millimeter-wave Communications in High-Mobility Environments</b>	<b>27</b>
3.1	Millimeter-wave Channels: Opportunities and Challenges . . . . .	27
3.2	The System-Level Simulator of Beamforming High-Mobility Scenarios . . . . .	29
3.2.1	Framework Overview . . . . .	30
3.2.2	Custom modules . . . . .	32
3.2.3	Data Structures . . . . .	34
3.3	The Object-Oriented SLoBMo . . . . .	35
3.3.1	Classes . . . . .	37
3.3.2	Resource Allocation . . . . .	39
3.3.3	Interference Calculations . . . . .	42
<b>4</b>	<b>Optimization of V2N Beams with Positioning and Doppler Estimation</b>	<b>43</b>
4.1	Publication . . . . .	43
<b>5</b>	<b>Vehicle Antenna Design Based on Wireless Channel Performance</b>	<b>54</b>
5.1	Publication . . . . .	54
<b>6</b>	<b>Assessment of mmWave Beamforming Handsets in Presence of the User</b>	<b>65</b>
6.1	Motivation and Related Work . . . . .	65
6.2	Methodology . . . . .	67
6.2.1	Numerical Modeling . . . . .	67
6.2.2	Experimental Validation . . . . .	70
6.3	Publication . . . . .	73
<b>7</b>	<b>Conclusion</b>	<b>80</b>
7.1	Summary . . . . .	80
7.2	Open Research and Future Work . . . . .	83
<b>References</b>		<b>85</b>

## CONTENTS

---

# RESEARCH OUTCOME

---

Here, all journal and conference manuscripts as the first author can be found. They represent the core contribution of this thesis to spread the knowledge acquired from its beginning.

## Journal Articles

[J1] C. Ballesteros, A. Pfadler, L. Montero, J. Romeu and L. Jofre-Roca, "Adaptive Beamwidth Optimization under Doppler ICI and Positioning Errors at mmWave Bands," in Elsevier Vehicular Communications, vol. 34, article 100456, April 2022, doi: 10.1016/j.vehcom.2022.100456.

[J2] C. Ballesteros, L. Montero, G. A. Ramírez, and L. Jofre-Roca, "Multi-Antenna 3D Pattern Design for Millimeter-Wave Vehicular Communications," in Elsevier Vehicular Communications, vol. 35, article 100473, June 2022, doi: 10.1016/j.vehcom.2022.100473.

[J3] C. Ballesteros, L. Vähä-Savo, K. Haneda, C. Icheln, J. Romeu and L. Jofre, "Assessment of mmWave Handset Arrays in the Presence of the User Body," in IEEE Antennas and Wireless Propagation Letters, vol. 20, no. 9, pp. 1736-1740, September 2021, doi: 10.1109/LAWP.2021.3095352.

## Conference Papers

[C1] C. Ballesteros, A. Pfadler, J. Romeu and L. Jofre, "5G Vehicle MIMO Antenna Capacity Based on a Rigorous Electromagnetic Channel Modeling," 2018 48th European Microwave Conference (EuMC), 2018, pp. 1077-1080, doi: 10.23919/EuMC.2018.8541637.

## CONTENTS

---

[C2] C. Ballesteros, M. Maestre, M. C. Santos, J. Romeu and L. Jofre, "An Architecture Analysis for Millimeter-Wave Optically Steerable Antenna Array," 2019 13th European Conference on Antennas and Propagation (EuCAP), 2019, pp. 1-5.

[C3] C. Ballesteros, M. Maestre, M. C. Santos, J. Romeu and L. Jofre, "A 3D Printed Lens Antenna for 5G Applications," 2019 IEEE International Symposium on Antennas and Propagation and USNC-URSI Radio Science Meeting, 2019, pp. 1985-1986, doi: 10.1109/APUSNCURSINRSM.2019.8889092.

[C4] C. Ballesteros, G. Ramírez, L. Montero, J. Romeu and L. Jofre, "Study on Beamforming V2I Scenarios for Sub-6 GHz and mmWave Channels," 2020 14th European Conference on Antennas and Propagation (EuCAP), 2020, pp. 1-5, doi: 10.23919/EuCAP48036.2020.9135473.



# LIST OF FIGURES

---

1.1	Average atmospheric attenuation of millimeter waves. . . . .	3
2.1	Instruments used by J.C. Bose during his investigations. . . . .	11
2.2	Wireless network metrics by Cisco. . . . .	15
2.3	Classification of 5G applications. . . . .	16
2.4	5G NR Configurations: NSA and SA. . . . .	17
2.5	Available access layer standards for ITS communications. . . . .	20
2.6	ITS Spectrum and channel distribution in main regions. . . . .	22
2.7	Resource allocation of 5G NR synchronization signals . . . . .	26
3.1	Diagram of the software framework. . . . .	31
3.2	Structure of the source code in the V2X Simulator. . . . .	37
3.3	Pseudo-UML diagram with class properties. . . . .	38
3.4	Resource distribution in a time-frequency grid. . . . .	40
3.5	Scheduling stack for cell-based or sensing types. . . . .	41
3.6	Simulation flowchart for the calculation of interferences. . . . .	42
6.1	Models of the two grip modes. . . . .	68
6.2	Human body modeling and simulation steps. . . . .	69
6.3	Different cuts in human body model. . . . .	70
6.4	Measured complex permittivity of a phantom sample up to 20 GHz. . . . .	71
6.5	Reflection coefficient between air and the phantom material up to 20 GHz. . . . .	72
6.6	Two-hand phantom ready to mount in the anechoic chamber. . . . .	73
6.7	Design of the millimeter-wave (mmWave) mobile handset. . . . .	74
6.8	Manufactured prototype of the millimeter-wave (mmWave) handset. . . . .	74

## LIST OF FIGURES

---

# LIST OF TABLES

---

2.1	Requirements for various vehicle-to-everything (V2X) use cases. . . . .	14
2.2	5G supported numerologies. . . . .	18
2.3	5G physical resources organization. . . . .	19
2.4	Comparison of IEEE 802.11p and 802.11bd. . . . .	21
3.1	Fields in the <i>mobility</i> struct. . . . .	34
3.2	Fields in the <i>antennaConfig</i> struct. . . . .	35
6.1	Metrics of the body simulations for different cut levels. . . . .	70
6.2	Skin phantom composition per 100 g of water. . . . .	71

## GLOSSARY

---

# GLOSSARY

---

<b>3GPP</b>	3rd Generation Partnership Project
<b>5G</b>	the fifth generation of mobile communications
<b>5GAA</b>	5G Automotive Association
<b>ADAS</b>	advanced driver assistance systems
<b>AI4CSM</b>	Automotive Intelligence for Connected and Shared Mobility
<b>AR</b>	augmented reality
<b>BS</b>	base station
<b>BSM</b>	basic safety messages
<b>C-ITS</b>	cooperative intelligent transport systems (ITS)
<b>C-V2X</b>	cellular vehicle-to-everything (V2X)
<b>CAGR</b>	compound annual growth rate
<b>CAM</b>	cooperative awareness messages
<b>CCAM</b>	cooperative, connected, and automated mobility
<b>CP</b>	cyclic prefix
<b>CP-OFDM</b>	cyclic prefix OFDM
<b>CSI</b>	channel-state information
<b>CSI-RS</b>	channel-state information reference signal
<b>CSMA/CA</b>	carrier-sense multiple access with collision avoidance
<b>D2D</b>	device-to-device
<b>DAS</b>	distributed antenna systems
<b>DCM</b>	dual carrier modulation
<b>DFTS-OFDM</b>	discrete Fourier transform spread OFDM
<b>DL</b>	downlink
<b>DMRS</b>	demodulation reference signal
<b>DSRC</b>	dedicated short-range communications

## GLOSSARY

---

<b>EC</b>	European Commission
<b>EIRP</b>	effective isotropic radiated power
<b>EIT</b>	European Institute of Innovation and Technology
<b>eMBB</b>	enhanced mobile broadband
<b>EMF</b>	electromagnetic field
<b>EPC</b>	evolved packet core
<b>ETSI</b>	European Telecommunications Standards Institute
<b>FBW</b>	fractional bandwidth
<b>FCC</b>	Federal Communications Commission
<b>FR1</b>	frequency range 1
<b>FR2</b>	frequency range 2
<b>GBSCM</b>	geometry-based stochastic channel model
<b>GCPW</b>	grounded coplanar waveguide
<b>gNB</b>	next generation NodeB
<b>GPT</b>	general purpose technology
<b>HHI</b>	Heinrich-Hertz-Institut
<b>ICI</b>	inter-carrier interference
<b>ICNIRP</b>	International Commission on Non-Ionizing Radiation Protection
<b>IMT</b>	International Mobile Telecommunications
<b>IoT</b>	Internet of Things
<b>ITS</b>	intelligent transport systems
<b>ITU-R</b>	International Telecommunications Union Radiocommunications Sector
<b>IVHS</b>	intelligent vehicle highway systems
<b>LOS</b>	line of sight
<b>LTE</b>	Long Term Evolution
<b>M2M</b>	machine-to-machine
<b>MAC</b>	medium access control
<b>MAE</b>	mean average error
<b>MCS</b>	modulation and coding scheme
<b>MIMO</b>	multiple input multiple output
<b>mMTC</b>	massive machine-type communications
<b>mmWave</b>	millimeter-wave
<b>NDRC</b>	National Development and Reform Commission
<b>NLOS</b>	non-line of sight

---

<b>NLOS<sub>v</sub></b>	vehicular NLOS
<b>NR</b>	new radio
<b>OFDM</b>	orthogonal frequency division multiplexing
<b>OFDMA</b>	orthogonal frequency division multiple access
<b>OOP</b>	object-oriented programming
<b>OSI</b>	Open Systems Interconnection
<b>OTFS</b>	orthogonal time frequency space
<b>PAA</b>	phased array antenna
<b>PBCH</b>	physical broadcast channel
<b>PCB</b>	printed circuit board
<b>PDF</b>	probability density function
<b>PEC</b>	perfect electric conductor
<b>PSS</b>	primary synchronization signal
<b>QuaDRiGa</b>	QUAsi Deterministic RadIo channel GenerAtor
<b>RAT</b>	radio access technology
<b>RB</b>	resource block
<b>RSU</b>	road side unit
<b>SAR</b>	specific absorption rate
<b>SCS</b>	subcarrier spacing
<b>SINR</b>	signal-to-interference-plus-noise ratio
<b>SLoBMo</b>	System-Level simulator of Beamforming high-Mobility scenarios
<b>SNR</b>	signal-to-noise ratio
<b>SS</b>	synchronization signal
<b>SSB</b>	synchronization signal block
<b>SSS</b>	secondary synchronization signal
<b>SUMO</b>	Simulation of Urban Mobility
<b>TD</b>	time domain
<b>TDL</b>	tapped delay line
<b>UE</b>	user equipment
<b>UHD</b>	ultra high definition
<b>UPC</b>	Universitat Politècnica de Catalunya
<b>URLLC</b>	ultra-reliable and low latency communications
<b>V2C</b>	vehicle-to-cloud
<b>V2G</b>	vehicle-to-grid

## GLOSSARY

---

<b>V2I</b>	vehicle-to-infrastructure
<b>V2N</b>	vehicle-to-network
<b>V2P</b>	vehicle-to-pedestrian
<b>V2V</b>	vehicle-to-vehicle
<b>V2X</b>	vehicle-to-everything
<b>VRU</b>	vulnerable road user
<b>WAVE</b>	Wireless Access for Vehicular Environments
<b>WPAN</b>	wireless personal area network



## CHAPTER 1

# INTRODUCTION

---

All stories have a beginning, not all of them necessarily have an end. Here is where this particular one starts. In this chapter, you can find the reasons and consequences of the work encompassed by this thesis. A bird's-eye view of the project is provided so it is easier to understand the steps followed during the process. Like rapids, this thesis makes its way through the hill of knowledge and takes the required deviations to overcome unforeseen circumstances and reach the final outcome more or less as expected. I hope you enjoy the ride.

## 1.1 Framework of the Thesis

It is 2018 when this thesis begins to become a reality and the world has not yet realized the real effects of globalization and what a global pandemic is. Connectivity starts to be talked about everywhere and the fifth generation of mobile communications (5G) is promising network capabilities never seen before. In this new generation, many applications and sectors are expected to take the wave of connectivity, which is expected to boost a breakthrough at several levels (mobility, healthcare, smart cities and homes, infotainment...) [1–3].

Given the broad range of fields being covered, it is quite difficult to estimate the real impact of 5G but some studies already forecast \$3.5 trillion output generated by its global value chain and more than 22 million jobs by 2035 [4]. Like the electricity or the internet, 5G is seen as a general purpose technology (GPT), enabling the development of many new industries and being adopted by a wide variety of sectors.

Two particular features of 5G new radio (NR) networks stand out among others: the use of massive amounts of antennas to provide beamforming capabilities to wireless devices and the use of the millimeter-waves (mmWaves) to alleviate the stringent bandwidth

requirements of the overcrowded sub-6 GHz spectrum. These two key points are to be assessed in this thesis putting the focus on special cases in which their potential benefits may suppose a step forward compared to current solutions. This is particularly the case of vehicle communications and urban mobility, which are discussed in the next chapter.

## 1.2 Motivation and Background

Given the novelties at physical-layer level introduced by 5G, a new horizon opens in front of us to discover the real potential of mmWave multi-antenna systems. A massive deployment of such technology implies new challenges to study. Some of them have been partially addressed in the past by the academy, like the use of a massive number of antennas to shape the antenna radiation according to the environment [5]. Many practical concerns appear when dealing with multi-antenna systems, especially when implementing them on low-cost, low-consumption devices (e.g., a smartphone).

One of the main driving forces to increase complexity of antenna systems with more elements is the need for more spectrum, associated to the use of mmWave frequencies. There is an enormous potential to be exploited to establish ultra-fast and massive links, but its most limiting factor are losses. Figure 1.1, extracted from [6], depicts the attenuation of electromagnetic waves at different frequencies, ranging from 10 to 400 GHz. The peaks in the graph are associated to the presence of atmospheric gases, especially oxygen and water vapor. For example, the oxygen molecules resonate at 60 GHz and they absorb great amounts of energy. This is a limiting factor for long-distance communications. The free-space transmission equation introduced by Friis [7] already defines a direct relation between frequency and path loss. Moreover, lower penetration in objects at mmWave frequencies when compared to lower bands [8,9] turn the direct view between transceivers into a critical issue. Some innovative solutions have been proposed to extend the cellular coverage to the inside of buildings without the need of an active repeater [10] but they are still far from a practical implementation.

It is worth mentioning at this point a common misconception when considering mmWave bands for long range communications. Under the assumption of a free, lossless environment, it is true that the power density scales down with the second power of the distance. However, the role of the frequency is tightly related to the concept of effective aperture. The actual power at the output of a receiving antenna ( $P_L$ , assuming a certain load) can be expressed in two ways, with quite surprising conclusions for each case [11]:

$$P_L = P_R \left( \frac{\lambda}{4\pi r} \right)^2 D_{Tx} D_{Rx}, \text{ and} \quad (1.1)$$

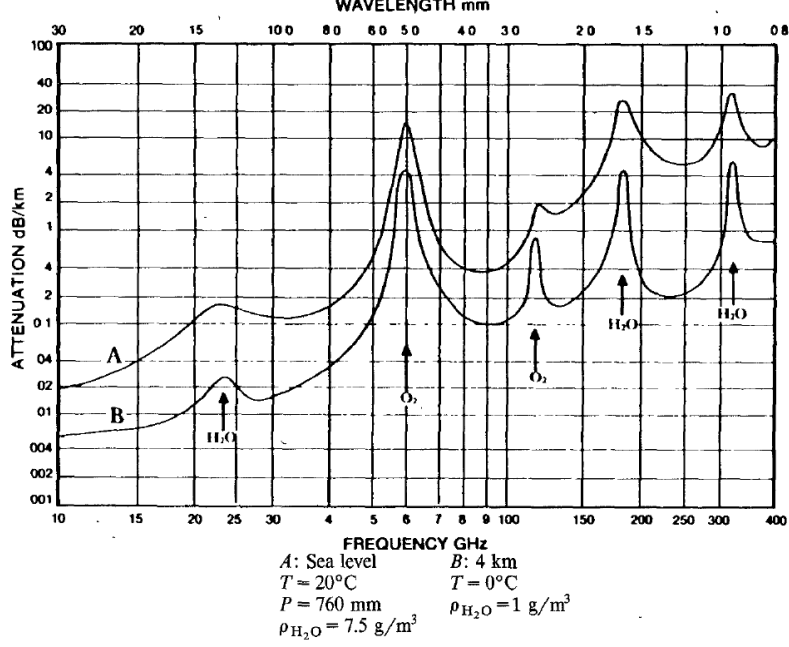


Figure 1.1: Average atmospheric attenuation of millimeter waves [6].

$$P_L = \frac{P_R A_{T_x} A_{R_x}}{(\lambda r)^2}, \quad (1.2)$$

where  $D_{T_x}$  and  $D_{R_x}$  are the directivity of both transmitting and receiving antennas,  $A_{T_x}$  and  $A_{R_x}$  are their respective effective apertures,  $r$  is the magnitude of the distance between them, and  $P_R$  is the total radiated power by the first one. As it can be stated, the impact of the frequency (or wavelength) is the opposite in the two expressions. And here is where the magic of antenna arrays happens. In the case of equally directive antennas, it is evident that larger frequencies lead to higher propagation losses, as seen in (1.1). This is the main fear when moving from conventional sub-6 GHz to mmWave bands. On the other hand, if one looks at (1.2), it is also true that keeping equal size radiators also scales the effective antenna size with frequency and, hence, its directivity. Then, it can be stated that the received power is not decreasing but increasing with frequency. Here lies the reasoning to make use of such frequencies, since many small radiators fit in the same physical space of a single low-frequency antenna and one can build highly directive structures to compensate (and even improve) the impact of moving up to higher bands with the additional benefit of larger available bandwidth.

As described in the following chapters, mmWave technologies are not completely new but their use has been restricted to remote sensing, security, and radars until now [12–14]. The

## 1. INTRODUCTION

---

ever-growing bandwidth requirements to allocate larger data rates and more user channels, given the crowded sub-6 GHz spectrum, and the technological advances at those frequencies have pushed mmWaves to the spotlight of mobile communications. In that regard, the 3rd Generation Partnership Project (3GPP) introduced new bands in this region from release 15, known as FR2, in contrast to FR1 that only considers up to 7 GHz [15].

Multi-antenna geometries are able to improve the performance of wireless systems in different ways to achieve faster data rates, and more energy efficient systems. As part of the new paradigm of mobile communications, they are a scope of research for the new generation of cellular systems. The consequence at physical level is the need of new electromagnetic models of the channel propagation and improved designs of the antennas.

The wireless channel is characterized by means of five main properties [16]:

1. **Pathloss:** The power is decreasing with distance and frequency.
2. **Signal fading:** Fluctuations at large (seconds) and small (milliseconds or below) scale due to the environment.
3. **Delay spread:** Different echoes of the signal arrive to the receiver at different times.
4. **Doppler spread:** The relative velocity between transmitter and receiver is translated to a shift in frequency, which varies along the band of interest.
5. **Angular spread:** Multipath propagation is given with a certain angular distribution.

Smart multi-antenna systems should be able to take advantage of some of these channel properties to exploit its capacity. The waveform employed by 5G is based on orthogonal frequency division multiplexing (OFDM), similar to that in Long Term Evolution (LTE). In particular, NR physical layer makes use of cyclic prefix OFDM (CP-OFDM) with flexible numerologies (subcarrier spacing) for both uplink and downlink, besides discrete Fourier transform spread OFDM (DFTS-OFDM) is left as an option for single-layer uplink transmissions when coverage is more critical than data rate [17]. The suitability of OFDM waveforms in NR is supported by the high achievable spectral efficiency to meet the most data-hungry applications, its compatibility with high-order multiple input multiple output (MIMO) schemes, robustness against time and frequency selectivity in large cell deployments, respectively, and it is also flexible and scalable to support a wide range of use cases and frequency bands [18]. However, sub-carrier orthogonality can be compromised in high-mobility scenarios, which are usually unfriendly for wideband communications given their

rapidly changing properties, leading to Doppler effect issues. Those issues are intended to be mitigated thanks to the flexibility of subcarrier spacing, but even in the case of widest separation may not be enough at very high speeds, especially if very high signal-to-interference-plus-noise ratio (SINR) is desired. This is the case of doubly-selective fading channels, such as those involving vehicular communications, which are prone to inter-carrier interference (ICI) and this should be considered when designing adequate solutions for such kind of communications [19].

In terms of channel capacity, a multi-antenna configuration is able to enhance the achievable rate [20], but there is a tight dependence on the proposed geometry for the design, which must consider all the surrounding elements as part of the structure. In order to study the effect of these new configurations, the analysis of the environment (at channel level and antenna design level) must be performed. Then, the well-known Shannon's channel capacity can be expressed in terms of the channel matrix for an arbitrary MIMO system as in [21]:

$$C = \log_2 \left( \det \left[ \mathbf{I}_N + \frac{P_T \mathbf{H} \mathbf{H}^*}{P_N} \right] \right) \quad (1.3)$$

where  $\mathbf{I}_N$  is the identity matrix of size  $N \times N$ ,  $\mathbf{H} \in \mathbb{C}^{N \times M}$  corresponds to the M-input and N-output channel matrix between the antenna ports, and  $P_T$  and  $P_N$  represent the transmission and noise power.

In  $\mathbf{H}$ , two main contributions are included. On the one hand, the impact of the wireless channel where the wireless link takes place. On the other hand, the radiation characteristics of both transmitting and receiving antennas. When both contributions are properly combined, the expression in 1.3 can be maximized.

For that purpose, two main ideas come into play:

- Spatial multiplexing allows to split the data to be transmitted into multiple streams. This is particularly evident when the previous capacity equation is expressed in terms of its eigenvalues,  $C = \sum_{i=1}^N \log_2(1 + \rho_R \lambda_i)$ , being  $\rho_R$  the signal-to-noise ratio (SNR) at the receiving site.
- Beamforming has gained momentum thanks to the use of massive architectures. They allow the use of tailored sharp beams to focus the radiated energy towards the intended user instead of wasting part of it when it is spread all around.

Higher frequency bands, when compared to sub-6 GHz, also allow a reduction of the radiating elements size. Multi-antenna solutions were already introduced in previous generations for MIMO purposes but 5G promises to fully exploit the potential of such archi-

## 1. INTRODUCTION

---

tures. This is a particular innovation, and challenge, for user equipment (UE) devices such as mobile phones or vehicles.

Massive MIMO and hybrid beamforming architectures are expected to take channel capacity and spectral efficiency to unprecedented levels. The use of a large number of radiators allows to focus the energy towards the intended users. It implies an improvement of the received power and a reduction of the interference towards non-desired directions, which is translated into a higher SINR. On the other hand, the uncorrelated transmission of simultaneous signals from the same antenna array can be exploited thanks to the hybrid precoding of symbols (digital and analog) [22,23]. This approach is particularly interesting in the case of massive arrays since it tries to find the balance between number of RF chains and analog phase shifters and amplifiers.

Beam determination algorithms should be employed to establish suitable pairs of beams between both link ends, but more sophisticated strategies than beam sweeping are to be studied to overcome overhead-related issues and make use of additional channel information available from different sources. In high-mobility scenarios, this is particularly critical. Wide beams tend to relax the update rate requirements but their associated gain may not be enough to overcome the losses at mmWaves. Wider beamwidths are also prone to larger Doppler spread. A relationship between the angular probability density function (PDF) of the multipath components at the receiver and the Doppler spectrum is demonstrated in [24, 25]. The divergence in Doppler shift of each multipath degrades the system performance, potentially causing significant impairments between replicas that lead to beam steering inaccuracy [26,27]. Then, a trade-off between system complexity and antenna gain must be found for each case.

Some flaws of current mobile solutions to deal with the abovementioned issues are to be identified and novel proposals to overcome them are to be proposed in the following chapters. Adequate geometries to maximize performance under realistic operation conditions, considering the impact of the physical carrier (human user or vehicle), is also an open topic to be studied to assess the validity of certain antenna designs in both vehicular and pedestrian communications.

### 1.3 Objectives

As mentioned above, 5G is expected to introduce to major novelties that suppose a change on the paradigm of mobile communications: massive antenna arrays and mmWave bands.

These novelties require adequate evaluation frameworks to assess new types of communications, as well as innovative solutions to address the issues related to higher frequencies and directive beams, especially when dealing with high-mobility scenarios. For that reason, this thesis tries to tackle those issues and achieve the following goals:

- Design of a standard-agnostic, system-level simulator of beamformed mobile users (downlink, uplink and sidelink).
- Study the effect of high-mobility scenarios on 5G communications and propose countermeasures based on the channel knowledge to fight undesired effects such as Doppler or signal blockage in
  - fixed stations with massive number of array elements, and
  - mobile users with limited space for multi-panel arrays (vehicular and handset).
- Study the impact of the user (vehicle bodywork and human tissue) on the radiation characteristics of multi-antenna arrays with adequate metrics to assess their performance in realistic scenarios. Given typical users and scenarios, propose the best array geometry for each case based on those metrics.

### 1.3.1 Hypotheses

There are several considerations that are used as starting point at the beginning of this work. The following list includes some hypotheses that are to be proven (or refuted) regarding the previous objectives.

- When modeling a wireless channel, several approaches can be followed. For a given scenario, ray tracing tools provide an accurate estimation of the impulse response, especially for very high frequencies. Their main drawback is the computational cost and the need of precise modeling of the environment. On the other hand, purely stochastic models are more repeatable and easy to compare. In order to build our simulator, an approach close to the second type is seen as a more suitable option given the need of testing hundreds of simultaneous links between random mobile users.
- The feasibility of massive MIMO with highly directive beams is tightly dependent on an accurate and fast update of the channel status. Hence, predicting the users behavior can ease the adaptation of the beam to its trajectory and the surrounding

environment. For that purpose, some side-band information should be needed. Common beam sweeping strategies are expected to fail when fast updates are required, leading to unacceptable outage probabilities.

- The distribution of the antenna panels on mobile handsets and vehicles has a paramount importance when beamforming is to be used. Antennas located close to the edge of the vehicle or the phone should help to create sharp pencil beams with minimum effect of the scattering due to the users themselves. Furthermore, covering the vehicle (or handset) surroundings with more antennas should improve the achievable coverage, at the expense of more complex and expensive systems.

### 1.4 Contributions and Thesis Structure

It is evident that mmWaves and multi-antenna solutions go hand in hand. Given the still immature state of those technologies regarding its deployment for ubiquitous mobile coverage, it is required to provide adequate metrics and an evaluation framework to assess such scenarios. In addition, generally accepted solutions are to be proven under realistic operation circumstances to validate their suitability. Next chapters will delve into the current state of standards and 5G mmWave solutions for future cellular communications as well as into the proposed methodology and solutions to the open challenges.

**Chapter 2** provides to the reader some useful background to understand the importance of mmWave multi-antenna systems in nowadays networks and the near-future projection of their usage connecting mobile devices. The history of mmWaves is presented to give credit to who actually began this revolution. Also the expected evolution of future cities and connected mobility is presented, as well as some necessary points about the current standards to understand how this thesis fits into the real picture.

Once bases have been settled, the methodology used throughout the work is explained in **Chapter 3**. More details about the channel models for mmWave 5G are discussed. The chapter includes also the ins and outs about the custom-made software framework developed to evaluate realistic wireless channels with tailored antenna solutions.

**Chapter 4** presents a solution for optimum base station (BS) beam determination in vehicle-to-network (V2N) scenarios. The analytical expressions behind the optimization algorithm and assumptions are detailed, as well as the main results provided by the evaluation tool previously presented. For the first time in the literature, the joint effect of side-information (positioning) and vehicle dynamics (Doppler) are considered to optimize



the directive radiation of a massive antenna array station towards the intended mobile user.

Regarding mobile users, **Chapter 5** first depicts the main requirements of vehicular multi-antenna systems. Useful metrics are provided to assess the actual performance of such architectures and some proposals are presented and compared. Contrary to commonly used models, the system-level performance of a set of vehicle-to-vehicle (V2V) links consider the impact of the vehicle on the antenna radiation, as well as a particular panel distribution and array geometry previously optimized for such scenarios.

In **Chapter 6**, a similar analysis is carried out concerning mobile mmWave handsets. In this case, the impact of the human user is studied considering its dynamics and scattering properties. The validity and repeatability of the results are ensured by means of realistic human-like user measurements together with different handset prototypes. For the user part, a phantom shape mimics the electromagnetic scattering properties of human tissues.

Finally, the main outcomes are summarized in **Chapter 7**. Some guidelines for future work and a brief discussion to further improve the present results are provided.

The work related in chapters 4 to 6 is presented as a compendium of journal articles which are the main outcome of the topics described by each one. The significance of the work is supported by peer-reviewed publications in prestigious Q1 journals such as Elsevier's Vehicular Communications and IEEE Antennas and Wireless Propagation Letters. Given the limited length of [J3], additional material is provided to the reader in Chapter6 to completely grasp the ins and outs of the methodology behind the results presented in the manuscript.

## CHAPTER 2

# THE JOURNEY TOWARDS MMWAVE MOBILE CONNECTIVITY

---

This section is intended to provide some historical and technological context to the work presented in the following chapters. The novelties later described are supported by the research of many engineers and scientist that started this journey many years ago and some examples are given below. Looking forward to the future, the forecast of globally connected cities, including vehicles, pedestrians, or even street furniture, justifies the need of further research on the topic of mmWave multi-antenna systems. Finally, some standarization framework is detailed as the base of certain limitations and assumptions in this thesis, as well as sources of improvement for solutions proposed regarding coming mobile generations.

### 2.1 A Not-so-Brief History of mmWave Research

The use of mmWaves may seem a very recent field of research and, actually, it is for cellular communications. However, one of the first experiments involving radio waves was carried out at 60 GHz in the 19<sup>th</sup> century. It was November 1894 when Jagadish Chandra Bose proved wireless transmission for the first time [28,29]. Only 30 years before, James Clerk Maxwell published the well-known mathematical derivation of EM waves [30] and, in 1885, Heinrich Rudolf Hertz experimentally proved Maxwell's theory with a simple, yet smart setup consisting of a a capacitance loaded dipole resonator transmitting standing waves towards a loop receiver [31]. Those Hertzian waves were about 50 MHz. In parallel, Bose worked on a less known experiment at much higher frequency.

Bose was able to fire a gun and also to ring a bell only using electromagnetic waves between the source and the target and very primitive instruments. Those can be seen in

Figure 2.1. In the experiment, he made use of a horn antenna, a Galena detector, an open resonator, and a spiral spring coherer (being those last two self-made). The scarcity of resources and poor knowledge about antennas and wireless communications at that time did not prevent Bose to succeed in his tests. He was able to penetrate two walls with 60 GHz signals, being the transmitter and the receiver separated about 23 m. This revolutionary experiment was the spark for the subsequent research in that field. Sir Neville Mott, winner of the Nobel prize in 1977 due to his findings in solid-state electronics, concluded that “J.C. Bose was at least sixty years ahead of his time... In fact, he had anticipated the existence of P-type and N-type semiconductors”[28], with regard to his invention of Galena crystals, later introduced as the foundation of ultraviolet receivers.

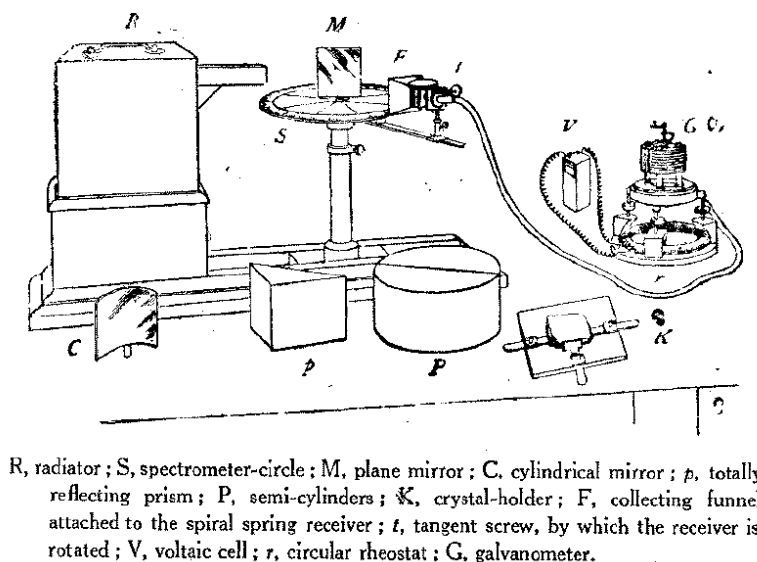


Figure 2.1: Instruments used by J.C. Bose during his investigations [32].

Until the second half of the 20<sup>th</sup> century, scientist devoted their research to much lower frequencies. Then, most published works tried to characterize materials in presence of electromagnetic waves. For example, this is the case of E. F. Nichols and J. D. Tear in 1923 [33, 34] or C. E. Cleeton and N. H. Williams in 1934 [35]. In the 19050s, a new discovery turned the focus back on mmWave communications. The invention of the maser by the Nobel prize in Physics Charles Hard Townes was the the predecessor of the laser. This device based its 24 GHz emission on the photonic radiation of ammonia molecules, which provide a low energetic gap.

Over the next decades, the cold war was the center of most people’s attention, also scientists. The U.S. Army started the development of high resolution radars at 70 GHz, but

the emergence of the laser also steered the focus towards optical bands for very high speed communications. Satellite communications and the rivalry between USA and the Sovietic Union fostered the creation of many remote sensing satellites with mmWave radiometers, such as the ATS-E [36] in the 1960s or the Nimbus-F [37] in the 1970s.

Despite mmWave technologies have been mainly devoted to radiometry and radar, the need for more spectrum makes this region appropriate for 5G systems. Its been more than 125 years since Bose's experimental demonstration of his findings in the Town Hall at Calcutta. Now, mmWave communications seem to finally take off when the first commercial 5G frequency range 2 (FR2) devices are already in the market.

### 2.2 Mobility in Future Cities Will Be Connected or Won't Be

Mobility is a broad term encompassing all those actions, policies, means, and services to satisfy the needs of transportation. Under this big umbrella, one could find public, private, and shared transportation methods. Each case has its own peculiarities, however, it is a common issue that mobility in future cities should address the following challenges [38–40]:

- **Congestion** is the most evident situation one could experience every day. Commuters take in average about 25 minutes to reach their workplace in Europe [41], and the same time back to home again. This implies almost one hour travelling every day. Given the growth of population density of cities and the use of private cars, it is common to see large traffic jams leading to higher levels of pollution, anxiety and stress on drivers, and less liveable spaces.
- **Pollution** is then the second challenge to be addressed. Transportation is the economic activity with most impact on greenhouse gases emmissions. In addition, road transport represented the 75.3% of the inland freight transport by 2018 [42]. Freight and passenger transport usually converge on our roads further increasing the levels of air pollutants. A newcomer to our cities are goods delivery services with a large number of riders. Some of them ride bikes or electric scooters, but others still use combustion engines.
- **Safety** is probably one of the main concerns of people when travelling in cities. Active transportation methods need to be protected by a redesign of urban spaces to prevent pedestrians or cyclist from sharing the same streets with cars. In addition, the use

of new technologies on vehicles like advanced driver assistance systems (ADAS) is helping to reduce traffic fatalities, as well as more strict policies regarding speeding and driving behaviors.

- **Social inclusion** is the usually-forgotten but critical issue when looking at future mobility. Thanks to the improvement of public transport and the arrival of shared and active mobility methods, more people can have access to a basic right as transportation. This has a direct impact on their social and economic status, reducing the need for private cars and allowing all people to reach any place, any time.

Many strategies can be carried out to tackle all those issues, but one is common to all. Connectivity is the booster of many industries and, in particular, transportation. Ubiquitous vehicular communications is a paramount step towards an increasingly automated mobility ecosystem. Known as cooperative, connected, and automated mobility (CCAM), this new paradigm is expected to improve road safety, energy efficiency, urban accessibility, social inclusion and reduce traffic congestion [43]. It is impossible to understand future cities and methods of transportation without it. And it comes together with electrification to reduce the dependency on oil and to reduce greenhouse gases and air pollutants. However, taking the emissions to energy generation plants is not the solution and new charging strategies and infrastructure have to be considered [44].

The role of connectivity, as mentioned above, is crucial when designing future mobility and cities. In the particular case of car communications, many new opportunities and difficulties appear. Safety-related applications and autonomous driving require extremely low latency and several users are expected to interact between them at the same time (as many as cars on the road, at least). If we extend the communication environment towards other entities, the concept of V2X appears on scene. And, on that regard, reliability is possibly the most critical issue that concerns manufacturers nowadays. Table 2.1 depicts some of the typical V2X use cases and their associated performance requirements. Depending on the type of messages and how critical is the adequate delivery of that data, more or less stringent requirements in terms of latency, reliability, and data rate are given. For instance, cooperative sensing (sensor data shared between vehicles) requires very low latency and high data rate for real-time environment sensing, but reliability is not a major concern. On the other hand, in pre-crash warning, vehicles deliver very short basic safety messages (BSM) or cooperative awareness messages (CAM) messages with very high integrity. Other intermediate situations are also depicted in the table.

## 2. THE JOURNEY TOWARDS MMWAVE MOBILE CONNECTIVITY

**Table 2.1:** Requirements for various V2X use cases. Data extracted from [45–47].

Use Case	V2X Mode	Latency	Reliability	Data rate
Cooperative awareness	V2V/V2I	100 ms	95%	< 100 kbps
Cooperative sensing	V2V/V2I	3 ms	> 95%	25 – 1000 Mbps
Cooperative maneuvers	V2V/V2I	3 – 100 ms	99.99%	< 10 Mbps
Pre-crash warning	V2V	3 ms	99.999%	< 10 kbps
vulnerable road user (VRU) detection	V2P	100 ms	95%	5 – 10 kbps
Traffic efficiency	V2V/V2I	> 1 s	< 90%	< 2 Mbps
Teleoperated driving	V2N	20 ms	99.999%	25 Mbps
High-density platooning	V2V	10 ms	99.99%	< 50 Mbps

With respect to the type of communications, V2X includes all type of links in which a vehicle is involved (named as V2X modes in Table 2.1). Each case should make use of one, or more, different link according to the intended target to communicate with. In case of cooperative environment awareness or sensing, V2V or vehicle-to-infrastructure (V2I) communications are involved if the vehicle shares data with other vehicles or a road side unit (RSU), respectively. In case of vulnerable road users (VRUs), who are often people walking or working close to the road, their detection is based on vehicle-to-pedestrian (V2P) links. Regarding teleoperated driving, a remote driver makes use of the cellular network to retrieve data from the vehicle sensors and manage its controllers and actuators. In this case, we talk about V2N. Other types of vehicle communications not included in the table are vehicle-to-grid (V2G) (for battery charging purposes) or vehicle-to-cloud (V2C), which can be a sub-category of one of the previous ones.

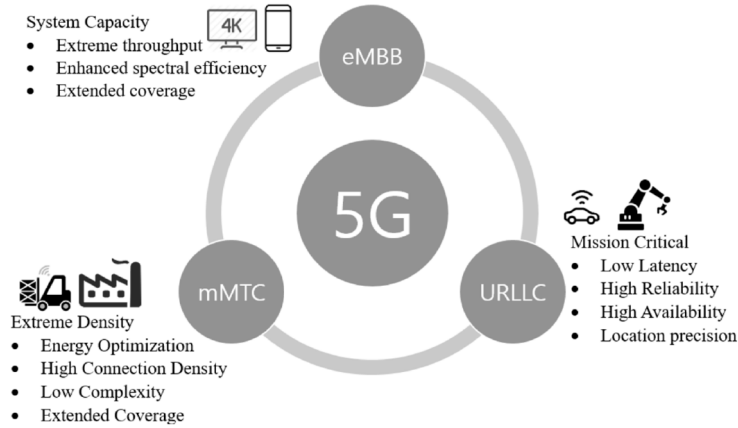
However, mmWave technology is not just the enabler of advanced V2X use cases. The ever-growing demands in terms of massive amount of users being served with cellular connectivity and channel capacity for high-speed data transmission are moving wireless technology towards higher bands to alleviate the stringent spectrum limitations at lower bands. Edge computing and widespread Internet of Things (IoT) devices are also pushing the known limits of wireless networks. The estimations of one recent Cisco white paper [48] forecast that the number of devices connected to IP networks will be more than three times the global population by 2023. The report also mentions that connected home applications will represent nearly half of the machine-to-machine (M2M) share, and M2M will be the fastest-growing category at 19% compound annual growth rate (CAGR) reaching 14.7 billions of connections by 2023, being IoT about the 50% of all networked devices (one third, wirelessly). The evolution of some other mobile metrics is shown in Fig. 2.2.



Figure 2.2: Wireless network metrics by Cisco [48].

Given such amount of connected devices, some of them even trying to communicate by means of device-to-device (D2D) ad-hoc networks, mmWaves are also a good candidate for ultra-dense network deployment. Regarding cellular topologies, pico- and femtocells are foreseen as a suitable solution to ensure wireless connectivity for home wireless devices and alleviate congestion on macrocells. Frequencies in the 28 – 73 GHz range have already been proven feasible for medium-to-small-size cell coverage (less than 200 m) in real urban scenarios [49, 50]. The use of directional antennas, and their associated technical challenges, permits much larger distances than the ones expected with monopole-like patterns commonly used for wide coverage areas. And the reduction on the physical size of radiating elements as the frequency increases, together with latest technological advances, is allowing to fit tenths or even hundreds of antennas to deploy smart antenna solution for such purpose.

The vast extent of applications covered by next-generation networks, starting with 5G and beyond, can be classified into three main categories, which are summarized in Fig. 2.3 extracted from [51]. Vehicular communications for cooperative and automated driving and massive IoT sensor devices are comprised between two of those categories: massive machine-type communications (mMTC) and ultra-reliable and low latency communications (URLLC). There is still a third one concerning high-throughput dedicated channels, namely enhanced mobile broadband (eMBB) communications. In the latter, mmWave communications are expected to excel. Large bandwidth requirements associated to applications such as augmented reality, high-resolution multimedia streaming or smart city cameras can only be accomplished under less restricted channels like the ones available at those frequencies.



**Figure 2.3:** Classification of 5G applications [51].

It is evident that multi-antenna mmWave antennas are expected to be a necessary step to fully exploit the capabilities of future connectivity applications. Their feasibility and requirements have been thoroughly studied but actual solutions to high-mobility environments and future cities must be provided. Some of the state-of-the-art solutions available at research, or even commercial, level to tackle some of the most challenging issues will be discussed on the following chapters. But now it is time to understand how standardization bodies give support to those needs to deploy those novel wireless technologies.

### 2.3 The Landscape of Standardization: WiFi, 5G, and Beyond

The goals to be accomplished by next-generation networks are very heterogeneous as previously seen. Some of the already operational wireless technologies, based on standards such as LTE or Wi-Fi, need to be combined between them and with new radio access technologies (interoperability). Therefore, a wide range of solutions is under discussion. In the particular case of 5G, it is not just an evolution with respect prior generations, but a complete change on the mobile communications paradigm. The following paragraphs are devoted to create a mind map on the reader with the evolution of wireless technologies concerning mobile users, paying a special attention to 5G.

#### 2.3.1 The New Generation of Cellular Communications

Over the last decade, the world has experienced the spreading of wireless technologies and mobile connectivity. Thanks to the arrival of 4G LTE and the revolution of smart-



phones, users worldwide have been able to share their coolest pictures instantaneously from anywhere. Digital transformation has reached all corners, from society to industry. According the International Mobile Telecommunications (IMT) requirements for 2020 and beyond defined by the International Telecommunications Union Radiocommunications Sector (ITU-R) [52, 53], the design goals of 5G should cover peak data rates in the order of 10/20 Gbps (for UL/DL), spectral efficiencies up to 15/30 bps/Hz and latencies below 4 ms in the user plane, for instance. However, the capabilities of LTE are well below those values and a smooth transition from one generation to the following one is planned by operators. In this sense, two operation modes are defined by the 3GPP: a first case in which 5G radio access networks are backed by the 4G evolved packet core (EPC) and a second case where 5G makes use of its own independent core network. The latter is expected to exploit the full capabilities of the new mobile generation but, in the meanwhile, operators start deploying sub-6 GHz radio access points under the already existing core network. Fig. 2.4 illustrates both cases.

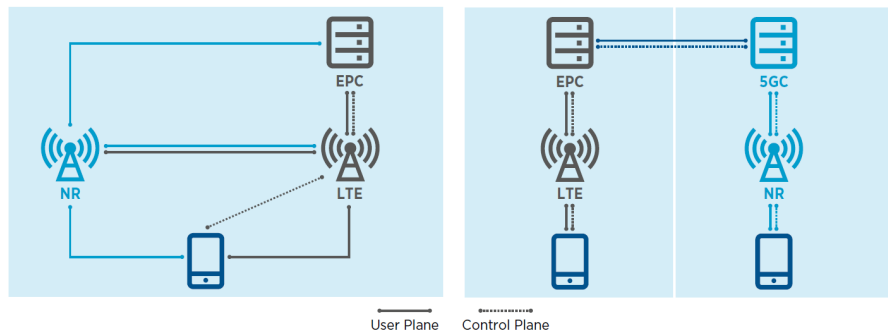


Figure 2.4: 5G NR Configurations: NSA and SA [53].

This natural coexistence of both generations is due to the fact that they are conceived with the same philosophy. Unlike past generations, they have been designed as fully packet-switched networks, even using similar radio access technologies like orthogonal frequency division multiple access (OFDMA). And this is where the evolution starts and the part mainly concerning this thesis. Despite many similarities (in the frame structure and waveforms), 5G NR has introduced the concept of flexible numerologies and the use of mmWave frequencies and massive MIMO is considered from its foundation [54].

- Frequency Range 2

A big step forward in the new mobile generation is the use of much higher frequencies than ever before. Some very-demanding applications in terms of bandwidth, may need to be developed at frequencies in which the spectrum is less crowded and the

## 2. THE JOURNEY TOWARDS MMWAVE MOBILE CONNECTIVITY

---

fractional bandwidth (FBW) to reach high throughput values is still technologically feasible. For that purpose, two main bands have been defined: frequency range 1 (FR1), ranging from 410 to 7125 MHz, and FR2, from 24.2 to 52.6 GHz.

- Numerologies

In LTE's OFDM, the spacing between subcarriers was set to a fixed value of 15 kHz. In 5G NR, this is a flexible parameter that defines the widening in frequency, and time, of the resources used in the link. Table 2.2 lists all available numerologies (indicated with the index  $\mu$ ) and the equivalent subcarrier spacing (SCS), as well as some other useful information that will be later explained. The value of the SCS is defined by  $\Delta f = 2^\mu \times 15 \text{ kHz}$ . However, only those from 60 to 240 kHz are allowed in FR2. The use of very wide SCS values at mmWave frequencies allows to compensate the larger degradation due to Doppler spread in this band, which could lead to a high loss in orthogonality if lower values were used.

- Massive MIMO and Beamforming

New FR2 bands and massive multi-antenna architectures come hand in hand. As previously stated, beamforming solutions are to be a must when operating at those frequencies and the first releases of 5G already consider this situation. In particular, adequate metrics and signaling waveforms are dedicated to obtain the required channel information for a suitable beam management. More details are given in the following paragraphs. Regarding MIMO modes, FR1 allows up to 8 layers in downlink (DL), whereas FR2 limits parallel data streams to 2, since it is expected that antenna elements will be mainly devoted to shape radiation patterns to enhance the system focusing capabilities.

**Table 2.2:** 5G supported numerologies. Data extracted from [15, 54]

$\mu$	SCS (kHz)	Cyclic Prefix	Sidelink	Frequency
0	15	Normal	Yes	FR1
1	30	Normal	Yes	FR1
2	60	Normal, Extended	Yes	FR1, FR2
3	120	Normal	Yes	FR2
4	240	Normal	No	FR2 (only SS/PBCH)

In order to understand the operational principles of 5G at physical layer, one should know how physical resources are organized. The basic frequency unit is the resource block (RB).

Each RB encompasses 12 consecutive subcarriers, so its span in frequency tightly depends on the numerology being used. In time, resources are organized in frames, subframes, slots and symbols. Each slot includes 14 symbols, 12 in case of extended cyclic prefix (CP), and its duration also depends on the numerology. Widening the frequency span also implies shrinking the symbol duration and, given a fixed number of symbols per slot, the duration of slot is provided by  $T_{slot} = 1/2^\mu$  ms. The duration of a frame is set to 10 ms, including 10 subframes of 1 ms each. Following the same rule of the slot duration, one can easily calculate the number of slots, and hence symbols, per frame or subframe. Table 2.3 summarizes those values.

**Table 2.3:** 5G physical resources organization. Data extracted from [54]

$\mu$	$N_{sym}^{slot}$	$T_{sym}$ (ms)	$N_{slot}^{frame}$	$N_{slot}^{subfr}$
0	14	66.67	10	1
1	14	33.33	20	2
2	12, 14	16.67	40	4
3	14	8.67	80	8
4	14	4.17	160	16

As mentioned above, one of the main goals of FR2 is to provide larger bandwidths to each user. In this sense, the 3GPP [15, 55, 56] defines the different bandwidth options for both the BS and the UE on each frequency range and the associated number of RB to achieve them. In particular, the available options are:

- FR1 – 5, 10, 15, 20, 25, 30, 40, 50, 60, 80, 100 MHz , and
- FR2 – 50, 100, 200, 400 MHz

Most of the previous aspects about 5G apply to the case of V2X. But there are subtle, yet critical differences that must be considered regarding this type of communications. Furthermore, other standards compete for the leadership in connected mobility. The automotive and urban mobility industry start to play an important role in communications and no one wants to miss the party. The following section details what the main stakeholders and available standards are and what are the main differences between them.

### 2.3.2 Standardization in the World of Vehicular Communications

In 2008, the European Commission publishes the ITS Action Plan that represents the kick-off for connected mobility [57]. Among other actions, they propose the assessment

## 2. THE JOURNEY TOWARDS MMWAVE MOBILE CONNECTIVITY

---

of future cooperative ITS (C-ITS) and the definition of the needed V2X specifications. On the other side of the Atlantic Ocean, the race started many years before. The U.S. Congress discussed for the first time a bill for intelligent vehicle highway systems (IVHS) in 1991, but it did not take hold. It was not until 2003 that the Federal Communications Commission (FCC) established the licensing and serving rules for dedicated short-range communications (DSRC) in the 5850-5925 MHz band [58]. The legislation in China, for its part, arrived much later but it took few years to develop a framework for ITS, including industry. In 2016, the Chinese Ministry of Transportation and the National Development and Reform Commission (NDRC) issued the “Implementation Plan to Promote Smart Transportation by Carrying Forward Internet Plus Convenient Transportation” [59]. It represented the first step towards the creation of a network of connected vehicles.

As we can see, there is not a single story in ITS and this has produced different regulations and standards in parallel to be adopted by the manufacturers. On the one hand, the European Telecommunications Standards Institute (ETSI) created its own C-ITS communication architecture (ETSI EN 302 665) [60] following the Open Systems Interconnection (OSI) model and, similarly, the Wireless Access for Vehicular Environments (WAVE) architecture (IEEE 1609.0-2019) was created based on the DSRC specifications [61]. For both cases, the access layer is based on the IEEE 802.11p (or WLANp), named as ITS-G5 in the European standard ETSI EN 302 663.

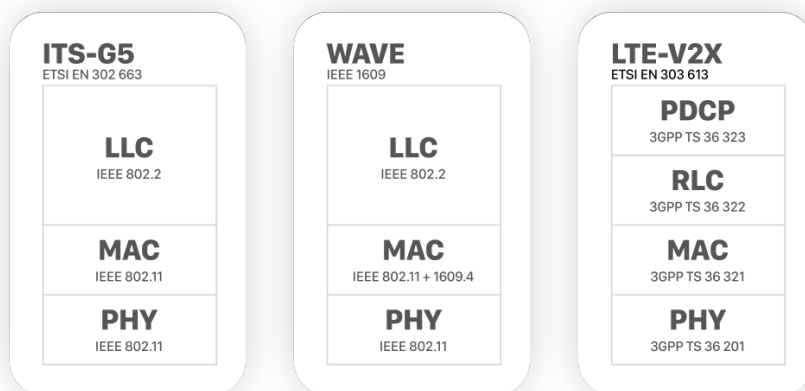


**Figure 2.5:** Available access layer standards for ITS communications [62].

On the other hand, the 3GPP proposed in its Release 14 the first solution for cellular V2X (C-V2X) with an LTE-based access layer, upwards agnostic. Two operation modes were defined for that purpose: Mode 3, for which the cellular network manages the resources,

and Mode 4, allowing completely independence to the vehicles from the network, as it is the case in WLANp. Therefore, vehicles should make use of two different interfaces for the network (Uu) or direct (PC5) connectivity. In China, this is the approach followed from the development of the first V2X communications. As a summary, Fig. 2.5 shows the three different options for ITS access layer.

The advent of new use cases with more stringent requirements in terms of latency, throughput, and reliability turns the capabilities of the first radio access technologies (RATs) to be insufficient [63]. In the case of C-V2X, 5G appears as the evolution to exploit the cellular network for advanced applications. Those standards that are built on top of IEEE physical and medium access control (MAC) layers also have the possibility of using an enhanced version, namely IEEE 802.11bd. Current DSRC standards have very limited applicability given their restricted performance. For example, the physical layer of WLANp makes use of fixed-space OFDM subcarriers (156.25 kHz) as a trade-off between multipath fading and Doppler spread [64], but more flexibility in numerologies should be available for advanced use cases in which reliability is a critical factor. In addition, WLANp is not able to deliver data packets with end-to-end latency much lower than 100 ms, also insufficient for certain Day-2 cases. Then, IEEE 802.11bd is designed with the goal of outperforming those obsolete capabilities. Some of its main novelties at PHY level are: flexible subcarrier spacing, the use of midambles (to address fast channel variations), optional dual carrier modulation (DCM) and the 60 GHz band for small-distance, high-throughput communications like video streaming. Table 2.4, extracted from [64], summarizes the main differences between WLANp and 802.11bd.

**Table 2.4:** Comparison of IEEE 802.11p and 802.11bd [64]

<b>Feature</b>	<b>802.11p</b>	<b>802.11bd</b>
Frequency band	5.9 GHz	5.9 and 60 GHz
Channel coding	BCC	LDPC
Re-transmissions	None	Congestion dependent
Midambles against Doppler	No	Yes
Sub-carrier spacing	156.25 kHz	312.5/{1, 2, 4} kHz
Max speed	252 km/h	500 km/h
Spatial streams	One	Multiple

Despite the variety of communication standards for ITS, all them were initially allocated within the same band. This may not seem a problem since each region got behind a different

## 2. THE JOURNEY TOWARDS MMWAVE MOBILE CONNECTIVITY

option, but the increasing momentum of C-V2X makes European and American regulators to consider its coexistence with WLANp-based access technologies. Fig. 2.6 illustrates the radio channels in the ITS bands for each region, as well as the ITU-R recommendation for ITS in the 5.8 GHz band [65, 66].

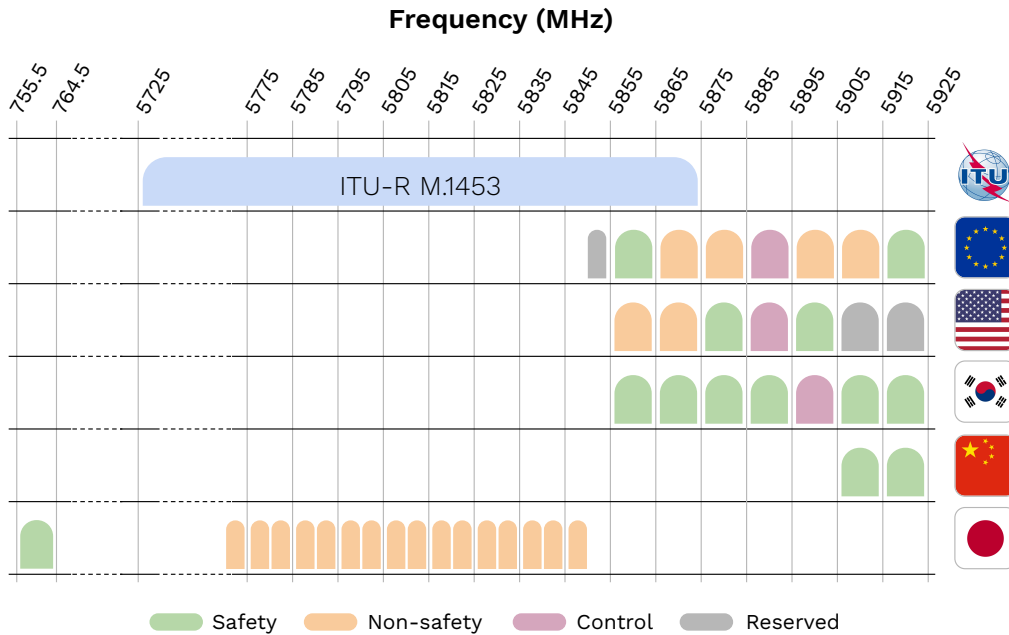


**Figure 2.6:** ITS Spectrum and channel distribution in main regions.

The inherent issues associated to DSRC, such as short operation range (200 – 400 m) and large access delay of carrier-sense multiple access with collision avoidance (CSMA/CA) mechanism [67], together with the arrival of a new cellular era enabling the full potential of V2X communications, shifted the focus of the automotive industry towards the C-V2X alternative as a mid-term solution. In consequence, the 5G Automotive Association (5GAA), underpinned by major stakeholders in the automotive and wireless technology industries, filled in 2018 a petition for waiver to the FCC to open the 20 MHz CH183 channel (5905–5925 MHz) for C-V2X [68].

However, the use of sub-6 GHz bands falls short when targeting to advance V2X use cases given the limited spectrum available [69]. Hence, 5G-V2X and FR2 appear on the horizon for such cases. The potential benefits of mmWave V2X must be also assessed considering many implicit challenges: larger signaling overheads for beam training, smaller cells with more frequent handover procedures, issues arising in high mobility environments as Doppler and beam misalignment, and large signal blockage [70].

The first proposals to make use of mmWaves for V2X include two lines of research. On the one hand, similarly to WLANp, WiGig is used as the base for 60 GHz vehicular communications. The WiGig family includes the IEEE 802.11ad standard, which has already been proposed for V2V [71, 72], and the upcoming IEEE 802.11ay, expected to allow higher MIMO orders and enhanced beamforming training [73]. IEEE 802.11ad is the baseline of IEEE 802.11bd when operating at the 60 GHz band. The main drawbacks of those approaches relate to the access and beam determination methods of WiGig, as well as the large path loss attenuation that limits its application to very short distances (it coincides with the peak of the absorption coefficient of oxygen molecules in the atmosphere [6]). On the other hand, 5G already introduced a second band of operation in the mmWave region, i.e., FR2. Initially conceived for cellular eMBB services, FR2 can also offload the channel usage between vehicles when more stringent use cases in terms of bandwidth are deployed. One of the main challenges concerns the joint operation of microwave and mmWave bands, since lower bands can provide a backup channel when directive beams at higher frequencies are blocked [74]. Moreover, the complete integration of both RATs can minimize the overhead and delay associated to beam training, increase the link reliability, and efficiently manage handover procedures in high-mobility environments [74]. However, all those benefits come at the expense of increased complexity of access protocols and a redesign of the frame structure.

Most 5G- and WiGig-based mmWave communications make use of directive beams determined with a brute force scanning (complete beam sweeping). Given the limitations of such approaches in high speed scenarios [70], due to misalignment and the presence of frequent blockages, more sophisticated methods are to be studied. For instance, the work in [75] already introduced the exchange of BSMs data at lower bands to reduce signaling overhead limiting the number of candidate beams to scan. Hierarchical codebooks [76, 77] or beam optimization based on a certain knowledge of the environment [78, 79] could also enhance the link performance for next generations and they are considered as the adequate alternative when evaluating different V2X situations in the following chapters.

## 2.4 Beamforming in 5G Networks

It is concluded from the evidence given in previous sections that mmWave wireless systems entail the necessity of using multi-element antenna geometries with beamforming capabilities. The way a certain technology manages such shaped beams determines, in most cases, the ability to keep track of users and the stability of the link. In the particular case of 5G,

in which most calculations of this thesis are based, the 3GPP already provides resources for establishing and updating the beams. However, the standard remains agnostic to the vendor's implementation of the beamforming strategy.

Permanent signaling is required between the communicating entities, two UEs or one UE and a next generation NodeB (gNB), to establish and maintain reliable directional links. In that regard, beam management comprehends all those procedures involved in the creation and update of beamformed patterns, which can also be grouped in two stages. First, the initial access or initial beam alignment is performed. At this point, neither communicating node has any knowledge about the situation of its counterpart. The approaches found in the literature for initial access are mainly divided in 1) side-information-aided [80–82] or 2) full-space sweeping [83, 84]. The first category makes use of a certain knowledge about the channel or the relative position between nodes to determine a first beam pointing at the right angular space. The exchange of positioning information aids to reduce the signaling overhead [75], at the expense of relying on external sensor data. Otherwise, the second type of initial access procedures assumes zero knowledge about the channel and the nodes must sweep the entire space to find the most suitable beam. This second approach usually requires a beam refinement stage in which more directive beams sweep a much smaller area. The use of hierarchical codebooks to provide different directivity levels has also been widely studied and the IEEE 802.15.3c standard already considers their usage for wireless personal area networks (WPANs) [85]. Hybrid approaches that make use of adaptive learning of the environment are also a matter of research [86–88].

Regardless of the initial access procedure, a second stage is triggered once the link is established. It concerns the tracking (and refinement) of the beam over time. The periodic update of the channel or beam information is required in order to ensure that the link quality is maintained. A comprehensive study on the procedures and challenges of beam management in the case of V2X mmWave links is given in [89, 90]. In the latter, besides the participation of the author of this thesis, a comparison between two proposed strategies for V2V in terms of link stability and channel usage can be found.

From the standard perspective, the 3GPP defines a set of signaling resources devoted to synchronization, channel state update and beam determination in [54]. In particular, there are two structures of interest regarding 5G beamforming procedures: the synchronization signal blocks (SSBs) and the channel-state information reference signals (CSI-RSs).



### 2.4.1 Synchronization signals

The initial access and synchronization procedure in 5G is carried out thanks to a set of physical-layer signals framed within the nomenclature of SSB. Each block contains three types of signals:

- The primary synchronization signal (PSS) is a 127-value sequence used to determine the radio frame boundaries and calculate the cell ID.
- The secondary synchronization signal (SSS) is also a sequence of 127 values and it defines the sub-frame boundaries, as well as being used for cell ID decoding.
- The physical broadcast channel (PBCH) carries information about bandwidth, timing, or synchronization signal (SS) burst periodicity, for instance. That data is sent together with the PBCH demodulation reference signal (DMRS) allowing that physical channel to be decoded.

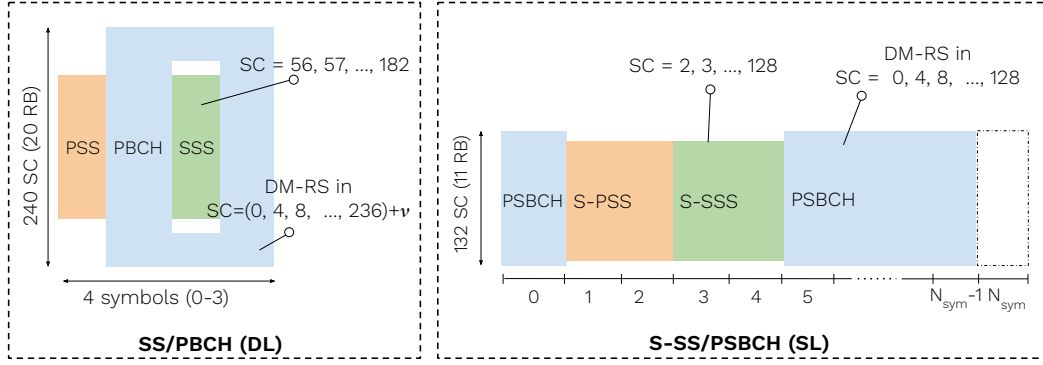
That naming applies to downlink channels, being the S-PSS, S-SSS and PSBCH their sidelink equivalents. The structure of the block also differs in how signals are arranged in the resource grid. Figure 2.7a depicts the SSB resource allocation within a slot for both cases. The reader is encouraged to dive into [91] for further details on all required procedures, channels and signals in LTE and 5G V2X.

SSBs are grouped in bursts allocated in the first half (5 ms) of a radio frame. The number of SSBs within a burst,  $N_{SSB}$ , depends on the employed numerology, but its maximum is set to 64 for mmWaves. Each SSB can be beamformed at both transmitting and receiving ends and thus be used to establish the best beam pair combination. The time between beam updates, or the periodicity of the SS burst ( $T_{SS}$ ) in other words, must consider the variability of the wireless channel and the shape –i.e., beamwidth– of the beams in the beamset. The standard allows different values ranging between 5 and 160 ms. Figure 2.7b illustrates the evolution of the SS bursts in the time axis.

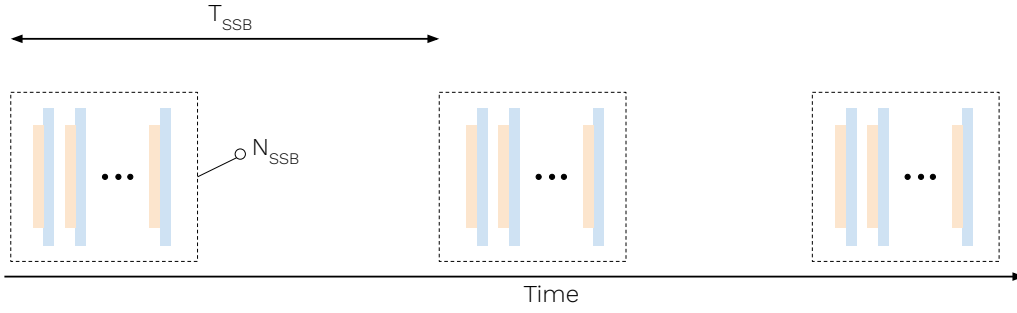
### 2.4.2 Channel-state information signals

Another mechanism that can be exploited for beamforming purposes is channel-state information (CSI) signaling. Those signals are used to report radio channel quality to the gNB with large flexibility regarding resource allocation [54]. It is not the scope of this section to dig into the details of the associated complex procedures and the unique feature to be highlighted at this point is the ability to provide channel measurements between consecutive

## 2. THE JOURNEY TOWARDS MMWAVE MOBILE CONNECTIVITY



(a) Structure a single SS and S-SS



(b) Transmission pattern of signaling bursts.

**Figure 2.7:** Resource allocation of 5G NR synchronization signals

SS bursts. Likewise, the gNB transmits UE-specific reference signals, namely CSI-RS, that are used at the receiver side to report quality parameters such as signal strength. When beamformed, those signals can be used also to determine the suitable beam combination with finer time accuracy. This is particularly useful in the case of beam refinement strategies, in which a coarse beam search can be performed with SS burst periodicity, whereas sharper beam pairs are established by means of CSI-RS reporting for instance.

## CHAPTER 3

# MODELING MILLIMETER-WAVE COMMUNICATIONS IN HIGH-MOBILITY ENVIRONMENTS

---

This chapter describes the peculiarities of high-mobility scenarios, such as the case of V2X communications. In particular, effects like Doppler or shadowing need to be properly modelled when dealing with fast varying channels and beamforming arrays. In order to provide numerical data to realistic scenarios, a simulation framework is developed in the AntennaLab. Here, detailed information about the framework is also provided. It serves as the basic tool to implement and validate the proposed solutions for multi-element antenna systems in high-mobility environments. The tool is built on Matlab, which is used as platform together with some already available solutions for channel and traffic modeling. In the last section of the current chapter, a second and more-sophisticated version developed during a reasearch visit in the Fraunhofer Heinrich-Hertz-Institut (HHI) is also described, stressing out the main novelties and features differing from the preliminary version.

### **3.1 Millimeter-wave Channels: Opportunities and Challenges**

As stated in Chapter 2, future mobile communications are expected to demand larger bandwidth and multi-element radiators. Both requirements converge in the mmWave region, where the spectrum is less crowded and the size of the antennas is smaller compared to typical sub-6 GHz bands. However, the use of such frequencies entails the consideration of additional challenges, which can be also used in benefit of the system performance.

A clear example of the difficulties when working at those frequencies concerns the

### 3. MODELING MILLIMETER-WAVE COMMUNICATIONS IN HIGH-MOBILITY ENVIRONMENTS

---

pathloss and coverage limitation. In [92], the authors compare several outdoor channel models between 6 and 100 GHz, but some common conclusions can be extracted: penetration in buildings makes almost unfeasible indoor-to-outdoor communications (above 20 GHz at least) and line of sight (LOS) is practically limited to a range of 100 m. Losses are partially overcome by the use of distributed antenna systems (DAS) but their location on the UE is a major issue. The ability to fit more antennas in the same physical space allows the operators to exploit diversity and beamforming to a great extent and the efficiency of those techniques tightly depends on an adequate assembly of the elements. The publications presented in Chapters 5 and 6 dive deeper in this discussion for two particular cases: a vehicular user and a pedestrian handset.

Taking a look to the wireless system in our arbitrary scenario, one could express the received signal over time,  $r(t)$ , by means of the transmitted one,  $s(t)$ , and the model of our channel impulse response,  $h(t, \tau)$ . The latter can be seen as the addition of several replicas that define the multipath environment, i.e., a tapped delay line (TDL) model following the definition from the 3GPP [93]. The following expression wraps the idea in form of a convolution, including an additive noise term at the end:

$$r(t) = h(t, \tau) \otimes s(t) + n(t), \quad (3.1)$$

In high-mobility scenarios, the multipath components do not only differ in the delay domain. The relative velocity between transmitter and receiver cause a frequency shift (Doppler), which differs from one component to another. Behind this unavoidable issue, one modulation technique emerges to take advantage of the channel sparsity when moving from typical time-frequency to delay-Doppler responses [94]. The orthogonal time frequency space (OTFS) modulation exploits both domains to encapsulate the symbols to transmit. But implementing this technique requires a very precise estimation of the channel and sophisticated equalizers [95], which is not always possible.

In case of modulation schemes based on orthogonal subcarriers, like the ones used in the fourth and fifth generations of mobile communications, the distortion of the signal due to Doppler produces a loss in the orthogonality of the symbols. According to Bello in [96], assuming a slow fading condition (coherence time much larger than the symbol period), the impulse response at the  $k$ -th subcarrier can be expressed as follows:

$$h_k(t) = h_k(t_0) + h'_k(t_0)(t - t_0). \quad (3.2)$$

The directive nature of mmWave links largely reduces the multipath effect and they are often limited to the LOS component plus a small contribution of close scatterers. This is

the case, for instance, of massive arrays acting as base stations. Assuming this situation, low Doppler spread is expected and, thus, the slow fading condition is met. Then, the detected symbol at the  $k$ -th branch of the OFDM receiver is expressed as:

$$\hat{x}_k = h_k(t_0)x_k + \frac{NT}{2\pi j} \sum_{\substack{l=1 \\ l \neq k}}^N \frac{h'_l(t_0)x_l}{l-k} + n_k, \quad (3.3)$$

where  $N$  is the number of subcarriers and  $T$  is the symbol period.

The work presented in Chapter 4 makes use of this knowledge to propose an alternative method to exploit the Doppler information. The expression of the ICI power in a beamforming V2N channel is derived and, together with some side-information aid (the vehicle estimated position), an optimization function for the beamwidth is obtained.

Complex systems such as an urban area full of interconnected vehicles are difficult to analyse from a purely theoretical point of view and numerical tools are commonly used to extract the most important features of the communication links. For that purpose, a tailored system-level simulation framework is designed. The goal is to implement the beamforming arrays and strategies proposed in the following chapters and validate their performance in comparison with those solutions available nowadays. Next section introduces the software structure and the set of features available to evaluate distinct channel models and multi-antenna structures.

## 3.2 The System-Level Simulator of Beamforming High-Mobility Scenarios

Since the main purpose of this thesis is to propose multi-antenna solutions for mmWave 5G communications and validate them in realistic environments, it is then required to use an accurate simulation tool. Then, an in-house solution is developed: the System-Level simulator of Beamforming high-Mobility scenarios (SLoBMo). It uses the MATLAB platform to recreate automotive (or any other mobile) links in urban and highway scenarios and estimates the channel response depending on the chosen antenna geometry and environment.

First, a preliminary, script-based, framework is created, which detailed in the following sections. It is used to obtain basic system-level parameters such as the achievable SINR or link failure probability. The results presented in chapters 4 and 5 have been obtained with this version of the code. At the end of the current chapter, an enhanced version based on object-oriented programming (OOP) and including new features is to be presented.

### 3. MODELING MILLIMETER-WAVE COMMUNICATIONS IN HIGH-MOBILITY ENVIRONMENTS

---

The numerical evaluation of beamforming mobile links requires of several steps, namely processing stages, which are depicted below:

#### 1. **Generation of user profiles and trajectories**

Each user participating in the network is created as an independent node, whose position is defined over time (static or moving). The trajectories are sampled at a given rate, providing a certain number of temporal snapshots of the scenario.

#### 2. **Establishment of wireless links**

According to a given assumption (the input of the software user), the communicating pairs are established, being one node able to communicate with one or more of the other nodes.

#### 3. **Radio channel emulation**

The wireless channel response is obtained over the simulation time for all pairs. In the first version of the code, isotropic radiators are assumed at each node. Then, the multipath response of the channel is weighted according to the radiation diagram of each node, which can evolve over time.

#### 4. **Calculation of system-level metrics**

Parameters such as channel capacity or outage probability can be obtained based on the signal at the receiving nodes.

The following sections detail how each of the abovementioned stages are addressed in the presented custom simulation framework.

#### 3.2.1 **Framework Overview**

The software framework is built in Matlab given its large amount of available off-the-shelf solutions for data treatment and wireless channel modeling. A modular design is pursued to ease the integration of new features along the project. Different types of beamforming strategies or channel models are to be tested and the proposed framework allows to substitute certain functions without reprogramming the rest of the software. Fig. 3.1 depicts the main blocks composing the software structure.

First, the trajectories of the communicating nodes are created by means of a module external to MATLAB. Simulation of Urban Mobility (SUMO) [97] (in blue) is an open-source tool that allows to define any kind of vehicular scenario and creates a random traffic distribution based on the user inputs. It is able to handle the effect of traffic lights,

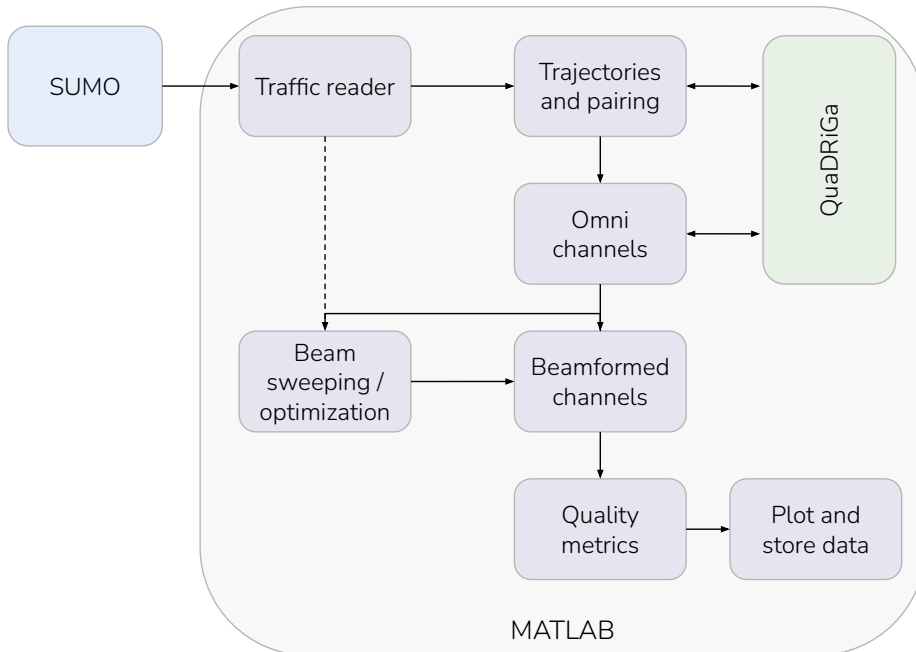


Figure 3.1: Diagram of the software framework.

pedestrians, and different types of vehicles. In this case, only vehicles and pedestrians are created in SUMO, whereas static nodes such as RSUs or cellular BSs are directly defined in MATLAB with their known coordinates.

A second open-source module imported to the framework is the QUAsi Deterministic Radio channel GenerAtor (QuaDRiGa) [98] (in green). It encompasses a set of object definitions and methods, already developed in MATLAB, to model radio channels following a semi-deterministic approach. In particular, the calculations are performed based on random processes, whose characteristics are given by the commonly used models such as those for vehicular channels in [99] or mmMAGIC [100]. The so-called geometry-based stochastic channel models (GBSCMs) provide a trade-off between repeatability, generalization of the outcome and accuracy. Ray tracing tools have been widely used to assess the expected performance of wireless systems, especially at high frequencies in realistic environments. The loss of applicability of the results to a general case and the time consuming calculations makes it an unfeasible option for this analysis. In contrast, purely stochastic models suffer from a lack of physical meaning and the spatial information is lost. GBSCM is used to estimate the radio channel parameters by assuming a set of arbitrary scatterers using the initial settings defined by stochastic models, whereas the particular contributions of the

scattering clusters are computed with the addition of various rays with individual angular and temporal features [101]. The evolution of the channels considers the correlation of the scatterers over time and their contributions are properly weighted.

The other modules, in violet, have been developed in MATLAB to particularly address different interfacing and processing functionalities within the framework. Their main purpose and description are given in the next section.

The operation of the software also relies on some additional toolboxes that must be installed beforehand to make it work in any Matlab platform. Those are the 5G toolbox, used for the metrics calculation given particular channel response, and the Antenna toolbox, to generate the beamforming patterns.

#### 3.2.2 Custom modules

The following modules have been developed to address the required processing stages:

- **Traffic reader**
  - Input: SUMO traffic file (\*.csv)
  - Output: MATLAB data file (\*.mat)
  - Description: The data generated by SUMO containing the position and speed of the vehicle at every time sample is translated to a data structure directly readable by any MATLAB function.
  
- **Trajectories and pairing**
  - Input: MATLAB trajectory files (\*.mat)
  - Output: *qd\_track* object array
  - Description: The vehicle trajectories are translated into MATLAB objects to be used with the QuaDRiGa channel simulator. All or a small subset of nodes can be used, with random links between them according to certain distance-based criteria. Depending on the environment, different channel models are applied (urban or highway). The interaction with building and other vehicles is used to determine non-line of sight (NLOS) and vehicular NLOS (NLOSv) segments, respectively.
  
- **Omnidirectional channels**
  - Input: *qd\_track* object array



- Output: *qd\_channel* object array
- Description: The links between the paired nodes are computed by assuming isotropic radiators (named as omnidirectional in QuaDRiGa) at both sides. The channel response for all multipath components over time, as well as the angles of arrival and departure, are stored in an array of type *qd\_channel*.

- **Beamformed channels**

- Input: *qd\_channel* object array, *antennaConfig* structure array
- Output: *qd\_channel* object array
- Description: The omnidirectional channels previously computed are weighted for the given beams at the transmitting and receiving sides. The evolution of the beams over time is calculated in a separate module according to the problem under study (dynamic beams, hierarchical beamsets, and channel-based beam optimization, for instance).

- **Beam sweeping or optimization**

- Input: *qd\_channel* object array, *antennaConfig* structure array
- Output: *qd\_channel* object array
- Description: Different approaches can be chosen to calculate the adequate beams along the trajectories of the communicating nodes. The particular details of each implementation are discussed in the corresponding chapters of this thesis.

- **Quality metrics**

- Input: *qd\_channel* object array, PHY layer configuration file (\*.mat)
- Output: MATLAB data file (\*.mat)
- Description: From the given beamformed channels, different parameters are computed to assess the link-level performance such as achievable data rate, outage probability (or service availability), maximum coverage for a target modulation and coding scheme (MCS) or data rate, and statistics about the usage of the beamset. Those figures of merit are based on a certain configuration of the physical layer, including the receiver noise figure as well as 5G-based waveform configurations (numerology, bandwidth, modulation tables...).

- **Plot and store data**

### 3. MODELING MILLIMETER-WAVE COMMUNICATIONS IN HIGH-MOBILITY ENVIRONMENTS

---

- Input: MATLAB data file (\*.mat)
- Output: Figure files (\*.pdf, \*.fig)
- Description: The data previously obtained is stored and the corresponding figures are plotted in an adequate journal-manuscript fashion.

#### 3.2.3 Data Structures

The operation of the simulator depends on the reading and creation of certain data structures. At each stage, new data is generated that is then passed to the next one as input.

The first data file is the XML output from SUMO. However, the traffic reader translates that data into a Matlab structure, much easier to work with. This new structure is saved as a variable named as *mobility*. Its properties are detailed in Table 3.1.

**Table 3.1:** Fields in the *mobility* struct.

Property	Type	Description
n_timesteps	uint32	Number of time samples ( $M$ )
n_veh	uint32	Number of vehicles ( $N$ )
scenario	string	Name of the scenario
time_res	double	Time between snapshots (in s)
veh_angle	$M \times N$ double	Orientation (azimuth) of each vehicle (in deg.)
veh_dis	$M \times N$ double	Distance travelled by each vehicle (in m)
veh_id	$1 \times N$ cell	Cell array with strings defining each vehicle
veh_in	$M \times N$ bool	Flag indicating if a vehicle is present in the simulation
veh_speed	$M \times N$ double	Speed of the vehicles in the direction of travel (in m/s)
veh_x	$M \times N$ double	Position of the vehicle in the x axis (in m)
veh_y	$M \times N$ double	Position of the vehicle in the y axis (in m)
veh_z	$M \times N$ double	Position of the vehicle in the z axis (in m)

During the channel calculation stage, several objects defined by the QuaDRiGa library must be used. More details about how that tool deals with trajectories (*qd\_track*) and channels (*qd\_track*) can be found in the user manual [102].

The way the simulator deals with beamforming patterns is based on the post-processing of the isotropic channels with a customized radiation diagram obtained through numerical evaluations of realistic array antennas. The user is able to implement any kind of antenna geometry but some considerations must be pointed out. First, cars are assumed to be a moving point on the map. Then, MIMO antennas are considered to be located at the same

place. Assuming a far-field situation, only a phase offset can be assumed between antenna ports. In that case, the user must fix that when combining the responses according to the particular geometry. On the other hand, if a single port with completely analog steering capabilities is assumed, this is not needed.

The radiation diagram of each port can be stored with the *antennaConfig* format, that is, using a MATLAB struct including the radiation patterns for each beam within the beamset. In Table 3.2, one can find the main fields in the struct.

**Table 3.2:** Fields in the *antennaConfig* struct.

Property	Type	Description
aggregatedPattern	$N_{el} \times N_{az}$ double	Aggregated radiation of all beams
az	$1 \times N_{az}$ double	Azimuth angles where the patterns are sampled (in deg)
beamwidthAz	$1 \times NM$ double	Beamwidth in azimuth for each beam (in deg)
beamwidthEl	$1 \times NM$ double	Beamwidth in elevation for each beam (in deg)
directivity	$1 \times NM$ double	Maximum directivity of each beam (in dBi)
el	$1 \times N_{az}$ double	Elevation angles where the patterns are sampled (in deg)
mBeams	uint32	Number of beams in elevation
nAnt	$1 \times 2$ uint32	Total number of antennas (rows and columns per array)
nBeams	uint32	Number of beams in azimuth
oversampling	$1 \times 2$ uint32	Oversampling factor of the beamset (elevation and azimuth)
pattern	$1 \times MN$ cell	Directivity patterns of all beams (in dBi)

### 3.3 The Object-Oriented SLoBMo

The previously detailed simulator was used to obtain several results regarding V2V and V2N links that were published in the work related in the following chapters. The achievable SINR can be estimated only considering each individual link and a macroscopic analysis is performed, so other parameters such as the probability of outage or beam usage statistics come into play. But that initial version of the code fell short quite soon when targeting to more thorough studies on the management of resources within a large vehicular network.

Life is unpredictable and, by chance, I ran into an unexpected opportunity in my way. The Fraunhofer HHI is a world's leading organization on applied research, participating in the most advanced projects on cutting-edge technologies about wireless systems, photonics, artificial intelligence and multimedia. In parallel to my journey as a Ph.D. candidate, the mmWave group at the Fraunhofer HHI, led by Dr.-Ing. Michael Peter, together with other 40 partners from 10 European countries, launch the Automotive Intelligence for Connected and Shared Mobility (AI4CSM) project, funded by the European Commission (EC). And

### 3. MODELING MILLIMETER-WAVE COMMUNICATIONS IN HIGH-MOBILITY ENVIRONMENTS

---

thanks to the European Institute of Innovation and Technology (EIT) Urban Mobility initiative, I was able to participate as an HHI visiting researcher.

During that time, an improved version of the software was developed to allocate new features for the needs of the project. Those requirements were in line with our previous concerns at the Universitat Politècnica de Catalunya (UPC) regarding vehicular communications. A precise calculation of the impact of surrounding interferers on resource allocation and beam management is paramount to deduce practical conclusions in beamforming environments. Luckily, other researchers at the HHI developed the tool used as basis of the wireless channel calculations of the first version of the simulation: QuaDRiGa. Then, all interests easily converged into a system-level simulator with enhanced capabilities to estimate standard-agnostic quality metrics of V2X communications on the physical layer.

For that purpose, the impact of the aggregated traffic should be considered. In order to be aligned with available standards for vehicular communications, OFDM-like resources are to be assumed to allocate user demands in terms of data exchange. But multiple scheduling algorithms are included to cover current and future expectations with high flexibility.

The efficiency of the simulations is improved with respect to the first simulator, making use of the minimum number of snapshots to simulate beam management and removing isotropic calculations. With an object-oriented approach, the new code is well-aligned with QuaDRiGa source code to maximize compatibility and increase fluency towards its structures. The proposed simulator acts as a wrapper of all possible evaluations of V2X with the focus on assessing beamforming arrays on vehicular platforms. In addition, any dependency to additional toolboxes is removed, so any MATLAB (or Octave) user can make use of it.

Figure 3.2 depicts the organization of the software regarding its source and data files. A main file can be created by the user to make use of any file within the folders in dark green, including the classes detailed in the following chapter. The code is developed to make use of the latest release of QuaDRiGa by the end of 2021, i.e., release 2.6.1. Data and results folders are intentionally left empty to allow the user to allocate any useful file for later calculations or the software outcomes, respectively. That can be also configured with a simulation settings object, later explained.

Only some parts of the code from the initial version were reused. Since the new software entailed a complete conceptual change of the way the simulations must be carried out, most part of the software was newly coded. From those reused features, the *mobility* structure stands out. The enhanced realism of SUMO traffic scenarios should be also used as input to the new software, so the same structure was kept to store data in MATLAB format. A

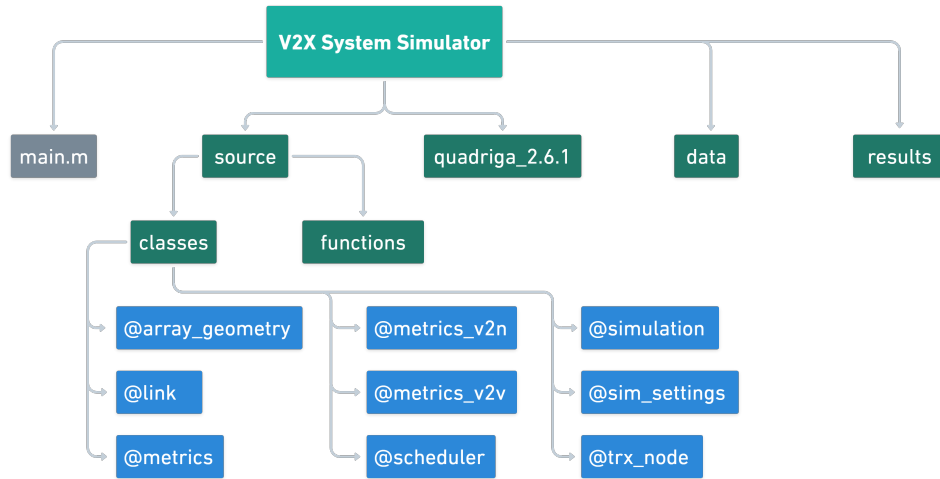


**Figure 3.2:** Structure of the source code in the V2X Simulator.

new function was developed to integrate that data into the new classes as the vehicle (or any other moving node) trajectories. Nevertheless, customary trajectories can be used if they are properly stored in the node objects.

### 3.3.1 Classes

As previously stated, the software is structured in several classes. Each class represents a particular entity within the simulation framework. Figure 3.3 depicts the main properties of each class and the relations between them. It must be mentioned that all classes inherit the properties of handles in MATLAB. Then, it is important to notice that assigning an object to a new variable is not the same as copying it. This is paramount to manage the simulation objects, since changing one variable linked to another handle (not copied) will modify the original object as well.

Those are the classes contained in the framework:

- **Class *array\_geometry***

It defines an antenna topology, including the number of panels (for example, to mount on a vehicle), and the elements per panel in vertical and horizontal dimensions. The number of beams in elevation and azimuth is also stored in this object.

- **Class *link***

This type of objects store all necessary information to calculate the overall metrics. For each pair of communicating nodes, a *link* object is created. The channel response between both ends, as well as the channel from the interferers to the current receiver,

### 3. MODELING MILLIMETER-WAVE COMMUNICATIONS IN HIGH-MOBILITY ENVIRONMENTS

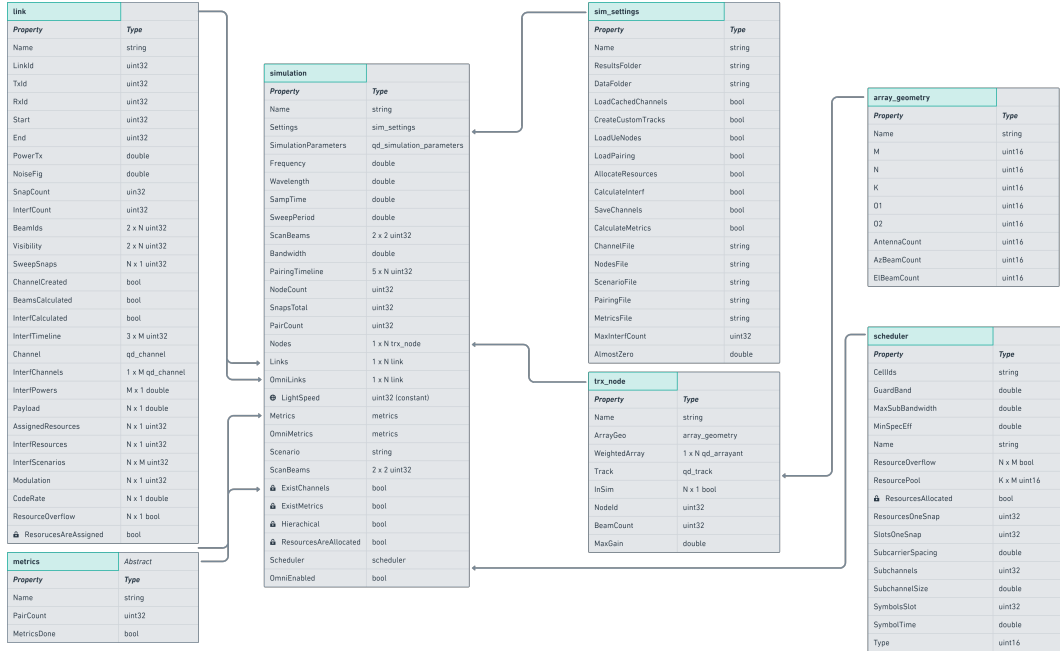


Figure 3.3: Pseudo-UML diagram with class properties.

is stored. Other important parameters such as the beam ID, the resource grid or the requested payload are also included.

- **Class *metrics***

This is an abstract class that encompasses all possible metrics to be measured for a given scenario. Only the V2V case is implemented to date, but different metrics may be required for other cases.

- **Class *scheduler***

It includes all features to implement resource allocation tasks. Depending on the given settings, a cellular station or the vehicles themselves can perform the assignment of resources for a pre-defined grid.

- **Class *sim\_settings***

This class includes the paths, file names, and flags necessary to read data and calculate and store the outcomes of the simulation.

- **Class *simulation***

This is the main class in the framework. It includes all necessary elements to perform the calculations and extract the required data. A list of nodes and another list of

links represent the scenario, but other variables are used to define properties such as the operating frequency and bandwidth, the simulation results, the type of scenario (highway, rural, urban...) or the sampling time.

- **Class *trx\_node***

This class represents a communicating entity. It can be static (base station) or moving (vehicle, pedestrian) and this is represented by its position over time. The node can be present only for some snapshots within the simulation and this is also stated, as well as the available radiation diagrams for single or multi-element antenna geometries.

### 3.3.2 Resource Allocation

Before defining how resources are managed in the simulated system, it is deemed convenient to mention how the software deals with time and frequency domains. Regarding the former, each simulation is composed of a certain number of temporal snapshots that represent instants of time between the beginning and end of our virtual scenario. The location of all communicating nodes is calculated for all of those instants and stored using a *qd\_track* object from QuaDRiGa (for more information, please take a look to the manual [102]). Since nodes do not need to be present in the scenario all the time, objects of type *trx\_node* also include a variable to state in which snapshots they are valid nodes in the scenario (*trx\_node.InSim*). On the other hand, frequency domain is constrained by the total bandwidth available in the system, stipulated in *simulation.Bandwidth*. This amount must be shared by all nodes in the simulation, so the simultaneous number of subchannels will be limited. The class scheduler includes the information concerning subchannel sizes and maximum bandwidth per user.

The simulator assumes that resources are distributed in a time-frequency grid, as in OFDM-like systems, with a certain granularity. Following the same nomenclature as in 3GPP standards, resources can be divided in slots (time) and subcarriers (frequency). A temporal snapshot usually will include several slots given its larger duration in most cases, whereas subcarriers are often grouped in subchannels. However, this particularity does not affect the actual implementation of the software, since the minimum frequency unit is the subcarrier to provide higher degree of generalization.

As said, the total simulation bandwidth includes a certain amount of subcarriers and each node will take a portion, i.e., a subchannel. The size of a subchannel depends on the user implementation, but it is usually limited by the data traffic required by the

### 3. MODELING MILLIMETER-WAVE COMMUNICATIONS IN HIGH-MOBILITY ENVIRONMENTS

---

link and the available resources. Figure 3.4 illustrates the abovementioned time-frequency decomposition.

The available resources in each snapshot depend on both the system bandwidth and the number of slots within a snapshot. No distinction between frequency or time resources is made since the final traffic will be the addition of both. According to the traffic pattern of each link, some of those resources will be used and the ones left could be grabbed by the next user.

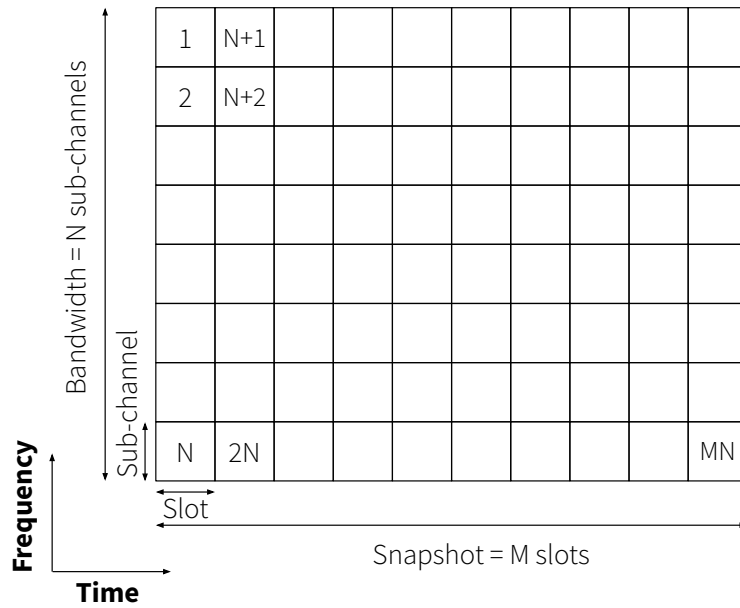


**Figure 3.4:** Resource distribution in a time-frequency grid.

There are three possible situations regarding the type of scheduling:

- **Sensing-based (TX)**

When a transmitting node wants to reserve some resources, a first sensing stage is performed. The TX ‘listens’ the environment and captures the incoming signals from other simultaneous TX nodes in the scenario. Based on the received power, it reserves those resources with the lowest level of sensed power.

- **Sensing-based (RX)**

In this second case, the procedure is exactly the same as in the former, but the RX is the one who senses the power at each resource. This is particularly interesting in beamformed communications. Due to the use of directive radiation patterns, the interferences perceived by the RX may largely differ from the ones at the TX.



- **Coordinated by a BS**

Finally, resource allocation can rely on the coordination of a base station (BS) that provides coverage to the vehicles (or, at least, to some of them). The BS uses the information of all simultaneous links to minimize the amount of them sharing the same resources. It does not guarantee that the interference level will be minimum, since the radiation between nodes is not known by the BS (unless reported), but it can reduce the average effect of interferences and provide a fair allocation to avoid greedy nodes. If more than one BS is present in the scenario, an adequate coordination between them is required in order to smoothly transmit from one coverage area to the next one, as well as ensure the link between nodes that may potentially be under different coverage areas.

Regardless of the scheduling type, the amount of resources is calculated based on the estimated SINR at the scheduling snapshots. Since the actual value will depend on the chosen resources, a noise floor for the maximum user bandwidth plus a practical SINR margin [103] is used for the estimation. Figure 3.5 shows an example of resources to be allocated based on both cell-based coordination or sensing-based scheduling.

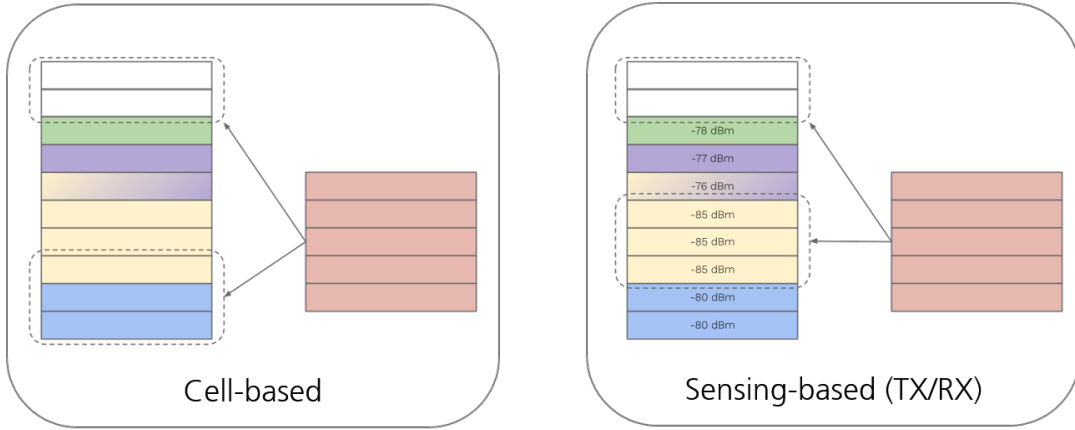


**Figure 3.5:** Scheduling stack for cell-based or sensing types.

Once the scheduling stage is finished, the local resource grid per snapshot is assigned to each link. Given the estimated SINR, the modulation and coding scheme is defined based on the achievable spectral efficiency.

$$\eta = R \times Q = \log_2 \left( 1 + \frac{SINR_{est}}{\Delta} \right), \quad (3.4)$$

where  $\eta$  represents the spectral efficiency obtained from the estimated SINR,  $\Delta$  is the practical gap according to [103],  $Q$  is the modulation order, and  $R$  is the coding rate.

### 3.3.3 Interference Calculations

One of the most interesting features of the simulator is the ability to calculate the channel response from interfering nodes. Once all users have a certain amount of resources assigned, it is possible to identify those transmitters using the same resources simultaneously and estimate the channel between them and their associated receivers.

During the scheduling process, the interference level is somehow estimated at each sensing snapshot if that option is chosen. When the receiver is the node performing the resource sensing, the visibility state is saved in the link object so the same is later used when calculating the interferences. This is needed to keep a certain level of coherence between the sensed environment during the scheduling stage and the interferences calculation. A more efficient approach could rely on the simultaneous calculation of interferences and the resource pool. However, the scheduling stage only uses those snapshots where the allocation is performed for channel calculation in order to avoid extremely long computation time.

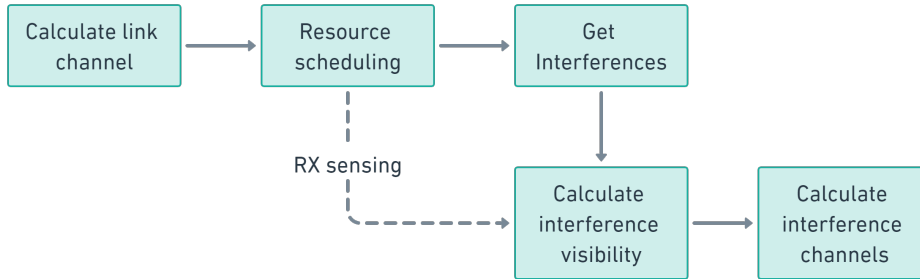


**Figure 3.6:** Simulation flowchart for the calculation of interferences.

Given that all *link* objects are able to store which resources are being used at each snapshot, this information is used to retrieve the colliding resources between pairs. Then, a list of the interfering links is created as well as the visibility state between the receiver of the current link and the transmitter of the interfering one, if not created during the scheduling stage (RX sensing). With that information, the QuaDRiGa channel from the interfering nodes is calculated and stored. In Figure 3.6, the simulation flow chart, from link generation to interference calculation, is depicted.

## CHAPTER 4

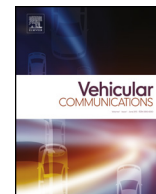
# OPTIMIZATION OF V2N BEAMS WITH POSITIONING AND DOPPLER ESTIMATION

---

This chapter includes a manuscript entitled "Adaptive beamwidth optimization under Doppler ICI and positioning errors at mmWave bands". The reader can find the study of the optimum beamwidth from the perspective of a cellular station when trying to communicate with a vehicle. Undesired effects such as Doppler and positioning errors are considered to derive the optimization expression.

### 4.1 Publication

[J1] C. Ballesteros, A. Pfadler, L. Montero, J. Romeu and L. Jofre-Roca, "Adaptive beamwidth optimization under Doppler ICI and positioning errors at mmWave bands," in Elsevier Vehicular Communications, vol. 34, article 100456, Apr. 2022, doi: 10.1016/j.vehcom.2022.100456.



# Adaptive beamwidth optimization under Doppler ICI and positioning errors at mmWave bands



Christian Ballesteros<sup>a,\*</sup>, Andreas Pfadler<sup>b</sup>, Luca Montero<sup>a,c</sup>, Jordi Romeu<sup>a</sup>, Luis Jofre-Roca<sup>a</sup>

<sup>a</sup> Universitat Politècnica de Catalunya (UPC), Jordi Girona 31, Barcelona, 08034, Spain

<sup>b</sup> Volkswagen Commercial Vehicles, Hermann-Münch-Straße 1, Wolfsburg, 38440, Germany

<sup>c</sup> SEAT S.A., A-2, KM. 585, Martorell, 08635, Spain

## ARTICLE INFO

### Article history:

Received 15 September 2021

Received in revised form 3 December 2021

Accepted 19 January 2022

Available online 24 January 2022

### Keywords:

V2N

Beamforming

Arrays

## ABSTRACT

The growing trends towards massive antenna arrays with focusing capabilities has enabled the use of higher frequencies at the cost of more complex systems. In the particular case of vehicular communications, millimeter-wave (mmWave) communications are expected to unleash a set of advanced use cases with stringent spectrum needs. However, dealing with very directive patterns and high frequencies entail additional challenges such as beam misalignment and Doppler effect. This paper presents a beam optimization procedure for vehicle-to-network (V2N) systems in which a base station communicates with high-speed users. Aided by the a priori knowledge of the vehicle location, the base station is able to estimate the average signal-to-interference-plus-noise ratio (SINR) until the next beam refresh considering the positioning accuracy and the Doppler inter-carrier interference (ICI). The estimation includes the antenna beamwidth, which can be optimized to maximize the achievable throughput. The numerical results indicate that the SINR can be significantly enhanced compared to beam sweeping with identical hierarchical codebooks while reducing the probability of outage.

© 2022 The Author(s). Published by Elsevier Inc. This is an open access article under the CC BY-NC-ND license (<http://creativecommons.org/licenses/by-nc-nd/4.0/>).

## 1. Introduction

### 1.1. Motivation

Vehicles become simultaneously more connected and automated. New applications such as tele-operated driving, HD mapping, platooning, and cooperative driving are essential to enable automated driving. These applications come with stringent requirements on reliability and throughput, which are particularly challenging in high mobility scenarios. In general, one refers to quality of service (QoS) requirements, such as latency, data rate, and reliability [1,2]. It is foreseen that connected vehicles will require more spectrum than provided nowadays. Even the recent roll-out of the 5th generation cellular system (5G) in sub-6 GHz, i.e., frequency range one (FR1), does not satisfy the spectrum need of connected vehicles together with the increasing cellular user demand [3]. Therefore, research focuses on the use of mmWave bands. In particular, appropriate beamforming strategies addressing the QoS requirements in vehicular networks are essential and investigated in this paper.

Operating at mmWave bands requires the use of beamforming techniques to cope with inherent additional losses [4,5]. This brings a few challenges with it, especially in vehicular scenarios. The authors highlighted in [6] the importance of massive antenna geometries in vehicle-to-infrastructure (V2I) based on the analysis of the channel capacity and eigenvalues, also emphasizing the need of adequate beam refreshing times. Similarly, in [7], the use of singular value decomposition (SVD) precoding is compared to maximum-ratio combining (MRC) and pre-defined codebooks in terms of SINR for a given highway scenario. The peculiarities of highway and urban V2I can be found in [8] and in [9], respectively. The former presents very high probability of line of sight (LOS) with small angular spread of multipath components, whereas the coverage of a base station (BS) in the latter case is much degraded due to the grid-like shape of the streets.

The use of highly directive beams also intends to reduce the interference between users and increase the energy efficiency, at the cost of higher beam update rates and signaling. To provide reliable focusing, accurate channel state information and/or user positioning needs to be exchanged. In case of mmWave channels, some experiment-based models are discussed in [10,11] that allow the prediction of the behavior of such type of links under realistic circumstances. However, accurate and real-time channel state updates

\* Corresponding author.

E-mail address: [christian.ballesteros@upc.edu](mailto:christian.ballesteros@upc.edu) (C. Ballesteros).

are crucial in rapidly varying links to allow reliable communications, which is paramount in safety-related applications. The angular and temporal correlation of the channel is discussed in [12] for different sub-6 GHz and mmWave frequencies, with sparser multipath components as the frequency increases. Doppler effects may also cause significant impairments leading to beam steering inaccuracy [13,14].

Location-based beamforming strategies require precise information of the users position, which is not always achieved. In the particular case of vehicles, several positioning technologies are available, such as: cellular trilateration [15], GNSS [16], or joint in-band position prediction [17]. The advent of 5G also promises enhanced positioning features [18] with expected positioning errors in the order of tens of centimeters.

In [19], the main use cases and challenges of beam management in vehicular scenarios are presented. The procedure can be partitioned into two parts: First, the beam alignment phase, where the beams from both sides need to be aligned to establish a communication link. Second, the beam management strategy including user tracking and refinement of beams. The collective knowledge of the vehicles' trajectory allows to predict their behavior and optimize tracking and beam selection or adaptation as in [20]. Typically, beam sweeping methods based on hierarchical codebooks reduce signaling overhead and are usually specification-compliant, as in the IEEE 802.15.3c standard [21].

Different from this conventional approach, this paper targets to improve the antenna beamwidth by adapting it according to the positioning quality of the shared vehicle trajectories and the inter-carrier interference caused by Doppler shifts. This approach is particularly useful for those V2N links in which the BS has more sophisticated focusing capabilities and calculation power. Beam sweeping approaches are limited to power measurements, not always a sufficient criterion of quality, and their validity may be short in time. In contrast, using the knowledge of the vehicle trajectory may help to enlarge the refreshing rate of the beams (and, thus, reducing overheads), as well as increase the accuracy of the focusing.

Other previous studies already tackled the problem of beam optimization in vehicle-to-everything (V2X). In [22], a beam-switching strategy of unequal beams covering a highway lane is proposed. The authors consider the vehicle's velocity with timing errors, but other undesired effects in complex environments with realistic radiation patterns are neglected. In [23], a triangular beam pattern modeling the vehicle radiation is optimized with the average capacity for a beam update period. The channel correlation and coherence time are also considered, which limit the validity of the beam and trigger the next update. However, other sources of error are not considered, such as Doppler effect or positioning inaccuracy. More recently, the authors in [24] propose an algorithm for beamwidth optimization in vehicle-to-vehicle (V2V) highway scenarios. They consider the misalignment due to positioning errors in the azimuth plane and the effect of surrounding users with a Montecarlo-based optimization of the entire system. The work presented in the current manuscript proposes a novel beamforming strategy for BS-to-vehicle systems. Assuming an orthogonal frequency division multiplexing (OFDM)-like communication, an expression of the SINR in presence of the Doppler ICI due to the vehicle motion is obtained using the channel correlation. In this case, the location of the target vehicle is assumed to be known with a certain accuracy, which is also used in the calculation of the desired and self-interference signal. Then, the average SINR until the next beam update is maximized for a given set of available beamwidths. The proposed strategy is studied for a large group of randomly distributed users and compared with the expected performance in typical beam sweeping strategies.

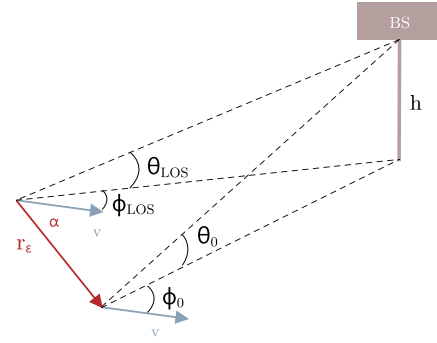


Fig. 1. Steering errors due to inaccurate positioning and vehicle movement.

## 1.2. Scope of the study

In this section, the scope of the paper is presented. The main contributions can be summarized as follows:

- Proposing a novel beamforming strategy to optimize throughput with a certain confidence level taking into account the vehicle position inaccuracy and speed.
- Considering Doppler effect and vehicle speed in the optimization. Wider beamwidths are prone to larger Doppler spread. Depending on the probability density function (PDF) of the angle of arrival (AoA) of multipath components at the receiver [25,26], the divergence in Doppler frequency of each multipath degrades the system performance.
- Taking into account the impact of positioning accuracy (relative and absolute position) on the optimum beamwidth, and hence the achievable throughput.
- Simulating V2N channels with realistic beam pattern of the antenna arrays using the QuaDRiGa channel simulator [27].
- Comparing the performance of the proposed method with the widespread beam sweeping strategy, for which some standards already provide resource allocation, e.g., 5G new radio (NR) and IEEE 802.15.3c.

The manuscript is organized as follows: section 2 presents the modeling of the positioning and Doppler, section 3 depicts the equations to obtain the maximization expression of the SINR, section 4 shows the simulated results to validate the proposed strategy, and section 5 concludes the paper with the main outcomes of the work. In addition, an appendix is given at the end with the ICI derivation.

## 2. System model

### 2.1. Positioning error modeling

In this paper, the positioning errors of vehicles are modeled following a bivariate distribution including distance and angle around the expected vehicle location in the XY plane. It is common to neglect small errors in height as the vertical beamwidth is assumed wide enough to prevent misalignment's. Typically, two independent and identically distributed Gaussian errors  $x_\epsilon$  and  $y_\epsilon$  are defined to model the position of the car on the pavement plane. One could also express the positioning error in polar coordinates as  $r_\epsilon \sim \text{Rayleigh}(\sigma_r)$  and  $\alpha \sim \text{Unif}(0, 2\pi)$ , being  $r_\epsilon$  the distance between the estimated and the real positions, and  $\alpha$  the angle of the error vector with respect to the driving direction.

Fig. 1 illustrates the relative position with respect to the BS of both the estimated and real vehicle locations.  $\theta_{\text{LOS}}$  and  $\phi_{\text{LOS}}$  stand for the expected LOS angles from the vehicle towards the BS, whereas  $\theta_0 = \theta_{\text{LOS}} + \Delta\theta_\epsilon$  and  $\phi_0 = \phi_{\text{LOS}} + \Delta\phi_\epsilon$  are the real

angles for the first position of the vehicle trajectory. The steering error in azimuth ( $\Delta\phi_\varepsilon$ ) and elevation ( $\Delta\theta_\varepsilon$ ) is thus calculated as:

$$\begin{aligned} \tan \Delta\phi_\varepsilon &= \frac{\sin(\phi_{\text{LOS}} - \alpha)}{\frac{\tilde{D}}{r} - \cos(\phi_{\text{LOS}} - \alpha)} \\ \tan \theta_0 &= \tan \theta_{\text{LOS}} \frac{\sin(\phi_0 - \alpha)}{\phi_{\text{LOS}} - \alpha}, \end{aligned} \quad (1)$$

where  $\tilde{D} = D \cos \theta_{\text{LOS}}$  is the distance from the BS to the car in the XY plane. All azimuth angles are referred to the driving direction defined by the velocity vector.

Following the same approach, one can calculate the beam misalignment due to the vehicle motion. In this case, the error vector is replaced by the distance traveled by the car from its initial position. The angle between the error vector and the velocity vector is now zero. The error when estimating the velocity is assumed to be negligible. Its impact is expected much lower than the actual positioning and the information is updated so often that any change in the traveling direction is not substantially degrading the estimation.

Then, the azimuth ( $\Delta\phi$ ) and elevation ( $\Delta\theta$ ) misalignment from its initial position follow these expressions:

$$\begin{aligned} \Delta\phi &\simeq \frac{v\tau \sin \phi_0}{D_0 \cos \theta_0 - v\tau \cos \phi_0} \\ \Delta\theta &\simeq \frac{\delta - \tan \theta_0}{1 + \delta \tan \theta_0}, \end{aligned} \quad (2)$$

where  $\delta \simeq h\Delta\phi/v\tau \sin \phi_0$  and  $v$  is the magnitude of the velocity vector. It is worth mentioning that small angle approximations ( $\sin x \simeq x$ ,  $\cos x \simeq 1$ ) have been used in the previous expressions given the small error due to the movement, since the beam and vehicle dynamics update rate are considerably faster than any noticeable change in its motion.

## 2.2. Doppler effect on ICI

The use of multi-carrier modulation schemes such as OFDM introduces a higher degree of robustness against channel dispersion. Long symbol duration is additionally compensated by a redundant cyclic prefix (CP) and multipath delay spread is thus mitigated. However, OFDM systems tend to lose the orthogonality between subcarriers in fast time-variant scenarios. This is the case of vehicular communications. High speeds introduce large Doppler shifts that may severely degrade the signal quality. In V2V, where two or more vehicles exchange information using direct sidelink communications, Doppler represents a major challenge. Very directive beams can alleviate this effect. A direct relation between beamwidth and Doppler spread is demonstrated in [25,26]. Conversely, thanks to the powerful focusing capabilities of next generation cellular stations, one could exploit the use of large arrays to mitigate the Doppler effect and also increase the power on the user's side. This is the case of V2N communications, where a cellular base station is linked to a vehicle using downlink and uplink streams. This work tries to address this situation in the following sections.

In [28], a statistical analysis of the ICI under the wide-sense stationary uncorrelated scattering (WSS-US) assumption is performed. The study also assumes Rayleigh fading but the channel is modeled in terms of a two-dimensional correlation function. Additionally, the authors in [29] present the temporal evolution of vehicular beamformed channels. This is later used to obtain the channel coherence time and a novel parameter such the beam coherence time, which can be related to a larger beam refresh. The work in [28,29] is thus used as baseline in the following sections to derive the actual power of the ICI in beamformed V2N channels. The

derivation is extended to a full 3D scenario in which a cellular BS optimizes its focusing towards a moving vehicle.

## 3. Optimum beamwidth analysis

### 3.1. Beamforming channel model

Given a wideband frequency selective channel, one can divide its impulse response for each OFDM  $k$ -th subcarrier to be  $h_k(t, \tau)$ . This response is zero-mean and stationary for all  $N$  subcarriers, with cross covariance between sub-channels  $h_k(t, \tau)$  and  $h_l(t, \tau)$  expressed as:

$$R_{h_k, h_l}(\tau) = \mathbb{E}[h_l(t)h_k^*(t + \tau)]; k, l = 1, \dots, N. \quad (3)$$

Assuming that the channel follows a WSS-US, the correlation function is factorable as follows [28,30]:

$$R_{h_k, h_l}(\tau) = R_1(\tau)R_2(k - l), \quad (4)$$

where  $R_1(\tau)$  is the delay correlation and  $R_2(k - l)$  the correlation between subcarriers. The first term is directly related to the Doppler spectrum, which cannot be assumed to follow a Clarke-Jakes distribution [31,32]. In this case, the delay correlation function,  $R_1(\tau)$ , can be split into LOS and non-line of sight (NLOS) terms, being the first one related to the pointing direction whereas the second one is assumed to follow the one-ring scatterer model as in [29]:

$$\begin{aligned} R_1(\tau) &= \mathbb{E}[h_k(t)h_k(t + \tau)] \\ &= \frac{K}{K + 1}R_{\text{LOS}}(\tau) + \frac{1}{K + 1}R_{\text{NLOS}}(\tau), \end{aligned} \quad (5)$$

where  $K$  is the Rician factor relating the power of LOS and NLOS components.

The channel correlation is also depending on the chosen antenna pattern for such scenarios. Following the same approach as in [29], the analytical expressions used for beam optimization make use of the von Mises distribution to model the beamforming gain. In this paper, the bivariate von Mises distribution is used as a model for the azimuth and elevation gain [33]. For two uncorrelated variables, the expression of the antenna gain reduces to:

$$G(\theta, \phi | \mu_\theta, \mu_\phi) = G_0 e^{k_\theta \cos(\theta - \mu_\theta) + k_\phi \cos(\phi - \mu_\phi)}, \quad (6)$$

where  $G_0$  is a normalization variable related to the maximum gain,  $\mu_\theta$  and  $\mu_\phi$  represent the elevation and azimuth steering angles and  $k_\theta \approx 1/\theta_{-3\text{dB}}^2$  and  $k_\phi \approx 1/\phi_{-3\text{dB}}^2$  are the concentration parameters of the bivariate von Mises distribution that are inversely proportional to the squared half-power (-3 dB) beamwidth for highly directive antennas.

$$\begin{aligned} R_{\text{LOS}}(t, \tau) &= \mathbb{E} \left[ \frac{(G(\theta_0, \phi_0 | \theta_{\text{LOS}}, \phi_{\text{LOS}})G(\tilde{\theta}, \tilde{\phi} | \theta_{\text{LOS}} + \Delta\theta, \phi_{\text{LOS}} + \Delta\phi))}{G_{\text{max}} \exp\{k_\theta + k_\phi\}} \right. \\ &\quad \times \exp\{j2\pi f_D t (\cos \theta_0 \cos \phi_0 - \cos(\theta_0 + \Delta\theta) \cos(\phi_0 + \Delta\phi))\} \\ &\quad \left. \times \exp\{-j2\pi f_D \tau \cos(\theta_0 + \Delta\theta) \cos(\phi_0 + \Delta\phi)\} \right] \end{aligned} \quad (7)$$

In (7), the LOS correlation is presented. Once normalized to the maximum achievable gain, two phase terms appear: one depending on time and one depending on delay. The former can be neglected since  $\Delta\theta$  and  $\Delta\phi$  are assumed to be very small (proportional to the delay). The correlation thus is not dependent on time and the wide-sense stationarity is fulfilled. The second phase

term depends both on the initial positioning error and that small angular shift due to the movement in  $\tau$ . The equation can be then simplified to the expression in (8).

Due to the inherently directive nature of beamforming mmWave links [34], those incoming paths close to the LOS component are expected to have a much higher impact on the perceived signal at the receiver. Therefore, for the sake of simplicity in the analysis, only the LOS correlation term is assumed from now on ( $K \gg 1$ ). In any case, this simplification only affects the beam optimization function and not the numerical analysis carried out in the following chapters, since all multipath components are considered when calculating the channel performance. In consequence, the delay-term of the correlation from the initial position onward can be expressed as in (8).

$$\begin{aligned} R_1(\tau) &\simeq R_{\text{LOS}}(\tau) \\ &\simeq \mathbb{E} \left[ \exp \left\{ k_\theta \left( \cos \Delta\theta_\varepsilon + \frac{\Delta\theta}{2} \sin \Delta\theta_\varepsilon - 1 \right) \right. \right. \\ &\quad \left. \left. + k_\phi \left( \cos \Delta\phi_\varepsilon + \frac{\Delta\phi}{2} \sin \Delta\phi_\varepsilon - 1 \right) \right\} \right. \\ &\quad \left. \exp \left\{ -j2\pi f_D \tau \cos(\theta_0 + \Delta\theta) \cos(\phi_0 + \Delta\phi) \right\} \right] \end{aligned} \quad (8)$$

The power delay profile (PDP) is assumed to be exponential, as in a tap delay model, in the form  $\text{PDP}(\tau) = \frac{1}{\sigma_\tau} \exp(-\frac{\tau}{\sigma_\tau})$ , with  $\tau \geq 0$ . In this expression,  $\sigma_\tau$  represents the delay spread, which can be translated to the channel coherence bandwidth. By calculating the Fourier transform of the PDP, one can obtain the correlation over the frequency,  $R_H(f)$ . The sampled frequency correlation at every subcarrier corresponds to the second term in (4),  $R_2(k) = R_H(k\Delta f)$ . Thus, the relation between the PDP and  $R_2(k)$  can be summarized as:

$$R_2(k) = \frac{1}{\sigma_\tau} \int_0^\infty e^{-\frac{\tau}{\sigma_\tau}} e^{-j2\pi k\Delta f \tau} d\tau = \frac{\kappa}{\kappa + j2\pi k\Delta f}, \quad (9)$$

where  $\kappa = 1/\sigma_\tau$ .

### 3.2. Received signal and SINR

The received signal at the user terminal is:

$$r(t) = h(t, \tau) \otimes s(t) + n(t), \quad (10)$$

where  $s(t)$  is the baseband signal at the transmitter and  $n(t)$  stands for additive Gaussian noise. The symbol  $\otimes$  denotes the convolution operation.

Assuming a slow-fading subcarrier channel (i.e., the symbol period is much smaller than the coherence time [6,29]), the symbols detected at the output of the  $k$ -th subcarrier of the OFDM receiver can be expressed as [28]:

$$\hat{x}_k = h_k(t_0)x_k + \frac{NT}{2\pi j} \sum_{\substack{l=1 \\ l \neq k}}^N \frac{h_l'(t_0)x_l}{l-k} + n_k, \quad (11)$$

where  $T$  is the symbol period ( $T = \frac{1}{\Delta f}$ ),  $x_k$  is the original symbol sent at the  $k$ -th subcarrier and  $n_i$  is the Gaussian noise after the correlator with zero mean and  $N_0$  power density.

In the Appendix, details about the calculation of the SINR accounting for ICI in beamforming environments are provided. Then, the SINR at each subcarrier can be expressed as:

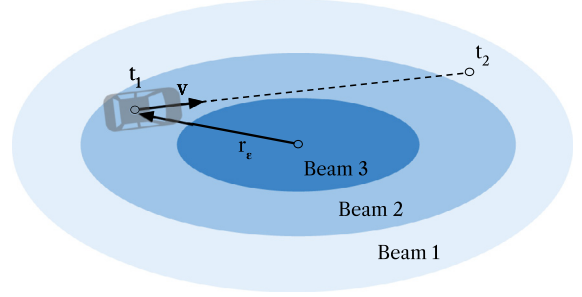


Fig. 2. Sketch of the vehicle position relative to the beam spot.

$$\text{SINR}_k = \frac{P}{P|R_1''(0)| \left(\frac{NT}{2\pi}\right)^2 \sum_{\substack{l=1 \\ l \neq k}}^N \frac{1}{(l-k)^2} + N_0B}. \quad (12)$$

As stated in (12), the SINR must be defined for each subcarrier. When accounting for those in-band fluctuations,  $\text{SINR}_{\text{eff}}$  can be used as an abstraction from multi-carrier instantaneous measures to a single value that allows to evaluate the link-level performance from a system perspective. In [35], further details about the calculation of the  $\text{SINR}_{\text{eff}}$  for OFDM systems are provided. The authors provide up to four different effective SINR mapping models for its calculation from the sub-carrier individual SINR values. Nonetheless, the links in the system experience less multipath components thanks to the inherent directivity of mmWave bands given the large attenuation of some multipath components, further increased by the use of sharp beams. Those components far from the angular region covered by the beam are severely attenuated, which translates to larger beam coherence times and smaller in-band SINR fluctuations. In that regard, and targeting to a low-complex implementation under realistic circumstances, the  $\text{SINR}_{\text{eff}}$  calculation is approximated to the average among all the individual SINR values per subcarrier.

$$\text{SINR}_{\text{eff}} \approx \sum_{k=1}^N \text{SINR}_k \quad (13)$$

### 3.3. Beam outage and link stability

High-mobility environments are prone to fast changes in the wireless channel characteristics. In the case of beamforming systems, steering information must be rapidly updated to provide an accurate enough tracking of the target. This information is also affected by prediction inaccuracies worsening the quality of the link. Beam recovery strategies must be provided to prevent beam-steering algorithms to lose track but this is left out of the scope of the present work.

Given a beam with  $\theta_{3\text{dB}}$  and  $\phi_{3\text{dB}}$  beamwidth in elevation and azimuth, respectively, the probability of falling outside its -3 dB footprint, also coined here as beam outage, is expressed as:

$$P_{bo} = 1 - \int_{\mu_\theta - \frac{\theta_{3\text{dB}}}{2}}^{\mu_\theta + \frac{\theta_{3\text{dB}}}{2}} \int_{\mu_\phi - \frac{\phi_{3\text{dB}}}{2}}^{\mu_\phi + \frac{\phi_{3\text{dB}}}{2}} f_{\theta,\phi}(\theta, \phi) d\theta d\phi, \quad (14)$$

where  $\mu_\theta$  and  $\mu_\phi$  are the steering angles of the beam in elevation and azimuth and  $f_{\theta,\phi}(\theta, \phi)$  is the joint density function of the vehicle position based on the definitions in Section 2.1.

The definition of beam outage does not directly relate to actual outage or reliability but it might be used as a hint of the suitability of a certain beam. Fig. 2 illustrates the position of a vehicle with respect to the beam spot for a given positioning accuracy for

a certain trajectory within the time period between  $t_1$  and  $t_2$ . It is assumed that the BS beam uses the closest beam to the expected position of the vehicle. Higher speed or larger positioning inaccuracy might lead to a wrong beam choice and hence reducing dramatically the perceived signal. This issue can be alleviated by increasing the beamwidth at the expense of reduced gain.

### 3.4. Beamwidth optimization

The target vehicle reports its position and velocity every  $T_v$  seconds. In parallel, the BS updates its beam with a  $T_b$  periodicity. In case of typical beam sweeping strategies, this would represent that all beam combinations are swept every  $T_b$  seconds, for instance, by means of synchronization signal block (SSB) bursts in 5G NR.

Since the proposed strategy is a single-side optimization algorithm, the BS makes use of the most recent vehicle information to predict the current position and driving direction. A safety margin due to positioning inaccuracies is considered by assuming that the standard deviation of the positioning error distribution is known. Thus the optimization is based both on the achievable channel capacity and the probability of the car to lay outside the beam footprint (beam outage).

The optimum beamwidths in elevation and azimuth ( $\theta_{-3\text{ dB}}^{\text{opt}}$ ,  $\phi_{-3\text{ dB}}^{\text{opt}}$ ) are chosen to maximize the overall data transmission for each beam period,  $T_b$ . In the optimization process, two simultaneous goals are pursued: minimize the outage probability and maximize the channel capacity (i.e., throughput). The abrupt degradation of the signal outside a beam coverage area makes the first goal almost a must, which also tightly relates to the second one. Data delivered outside the beam boundaries should be left as marginal, triggering an update of the beam for the next period in case that the vehicle is outside that area. Furthermore, accounting for involuntary data reception outside the beam coverage may lead to a suboptimal use of resources. Then, the optimization function can be written as:

$$\theta_{-3\text{ dB}}^{\text{opt}}, \phi_{-3\text{ dB}}^{\text{opt}} = \arg \max_{k_\theta, k_\phi} \int_0^{T_b} (1 - P_{\text{bo}}) \log_2(1 + \text{SINR}_{\text{eff}}), \quad (15)$$

which includes the effective SINR ( $\text{SINR}_{\text{eff}}$ ) and the beam outage probability as parameters.

Given a set of pre-defined beamsets, with different azimuth and elevation beamwidth for their individual beams, the closest beam to the expected LOS is chosen for each. The optimum one from this subset of beams is chosen based on the maximization criterion in (15). This approach tackles a complex optimization problem with a simple, yet feasible way for massive deployment with multiple vehicles under real-time coverage.

## 4. Numerical evaluation

The proposed optimization strategy is then validated through numerical simulations. A set of  $N_v$  vehicles is randomly distributed within the coverage area of a BS. Each one is independently simulated assuming a linear trajectory with a constant speed,  $v$ , during  $T_t$  seconds. Once the trajectory of the current vehicle is simulated, the results are stored and the next vehicle is dropped to the scenario. The car positions are sampled every  $\Delta t$  seconds and all values (e.g., SINR, outage) are computed for each sample. LOS visibility is assumed for all users, following the channel model proposed by the 3rd Generation Partnership Project (3GPP) for highway scenarios in [36]. In that regard, the QUAsi Deterministic Radio channel GenerAtor (QuADriGa) libraries are used to retrieve the channel impulse response along each trajectory [27]. The results discussed below are based on the averaged values for all

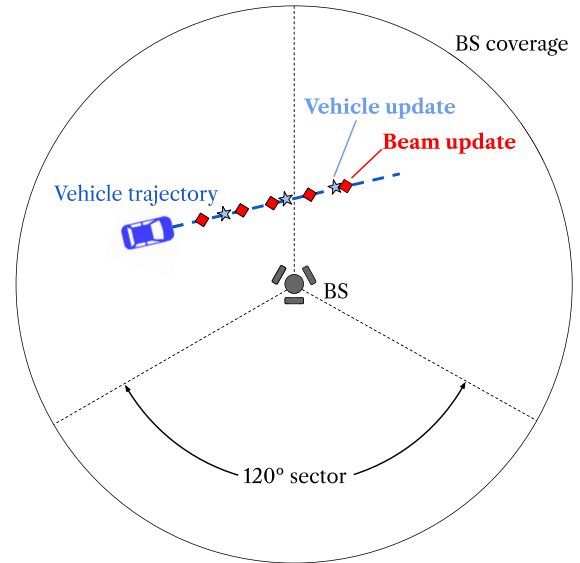


Fig. 3. Simulation scenario with a single vehicle. The update of the vehicle information and the BS beam is illustrated along the trajectory.

Table 1  
Parameters used for the simulation.

Parameter	Symbol	Value
Carrier frequency	$f_c$	28 GHz
Channel bandwidth	$B$	50 MHz
Transmission power	$P_T$	20 dBm
Channel model		Highway LOS [36]
Number of vehicles	$N_v$	500
Max BS-vehicle distance		300 m
Velocity	$v$	{25, 50, 100, 150, 200} km/h
Total simulation time	$T_t$	5 s
Sampling interval	$\Delta t$	0.01 s
Beam update period	$T_b$	{20, 40, 80, 160} ms
Vehicle positioning period	$T_v$	200 ms
Number of sectors	$N_s$	3
Azimuth sector		$[-60, 60]^\circ$
Elevation sector		$[-60, 30]^\circ$
Number of beamsets	$N_b$	3
Azimuth beamwidth	$\phi_{-3\text{ dB}}$	{24, 12, 6} $^\circ$
Elevation beamwidth	$\theta_{-3\text{ dB}}$	{50, 24, 12} $^\circ$

computed trajectories to obtain suitable statistics. Fig. 3 depicts the simulation scenario for a given vehicle trajectory.

The BS is composed by  $N_s$  equal sectors covering the entire azimuth range. It calculates the optimum beam with  $T_b$  periodicity and the vehicle reports its (randomly erroneous) position every  $T_v$  seconds. Up to  $N_b$  beamsets are considered at the BS, choosing the closest beam towards the car for each of them. The  $N_b$  beams are then evaluated in terms of the expressions in Section 3.4. Then, every  $T_b$ , the process is triggered again with the most recent information of the car. Table 1 lists the different simulation parameters.

When evaluating the suitability of a beam, one can follow several criteria. Typically, beam sweeping strategies are based on power measurements carried out by the receiver when the transmitter sends some signaling messages with a finite set of beams. Nevertheless, the beam with the highest power is not always the one with the best performance in terms, for example, of SINR – tightly related to throughput and error rates. On the other hand, repeated messaging with several beams leads to an increased overhead and larger periods of time to retrieve the optimum beam. In addition, the “instantaneous” measurement of such beams re-



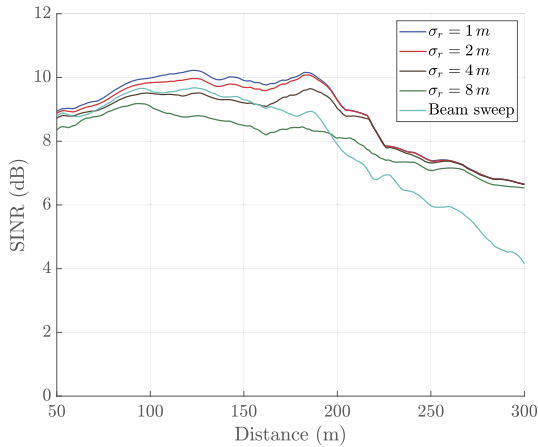


Fig. 4. SINR against LOS distance between the BS and the vehicles.

quires fast refresh rates so they are valid enough until the next update. The proposed approach only makes use of the position and speed information from the receiver, which is periodically reported but at a much lower rate with very low associated overhead. The position and speed information can even be sent in a separate channel at lower frequencies. The use of optimization algorithms to retrieve the optimum beamwidth is also discarded due to its complex application in realistic scenarios. However, the presented methodology later compared to some optimization algorithms with a subset of vehicles to prove that the benefit-cost ratio is quite low when compared with the proposed approach. The authors propose to substitute current beam sweeping stages by a single-message exchange from the vehicle to the base station and fast SINR calculations using existing codebooks with the previous expressions.

The performance of such approach is thus compared to a typical hierarchical beam sweeping strategy based on periodical power reports from the receiver once the transmitter sends signaling bursts with all possible beams. It is decomposed in two phases. First, a low-directivity set of beams is evaluated, corresponding to the so called beam determination stage. The next beam update period is used for beam refinement, in which a set of narrower beams is used. The limit in the number of beams to sweep within a  $T_b$  interval defines the maximum number of neighboring beams to test so they still fulfill the requirements of current standards as in 5G NR, which limits the signaling blocks to 64 per burst in the case of frequency range two (FR2) [37]. The beamwidth is reduced until the highest hierarchy is reached. Then, only neighbor beams are swept until the vehicle exceeds the coverage of a sector, where the low-level beams are swept again and the process starts again. All beams are swept at the lowest level to allow the BS to find the car regardless its position. A fixed number of 5 neighbors per dimension (25 in total) are swept at higher levels.

#### 4.1. SINR evolution

There are two main parameters that influence the optimization as previously stated: the vehicle speed and the accuracy of the positioning method, defined by the standard deviation of the positioning error ( $\sigma_r$ ). In this section, the evolution of the SINR is studied for different cases in terms of those parameters. For instance, Fig. 4 depicts the SINR as a function of the distance between the vehicle and the BS for several positioning error values, i.e., standard deviation of the Rayleigh distribution. All vehicles drive at a constant speed of 100 km/h and the beam is updated every 40 ms.

As expected, the divergence between lines in Fig. 4 is reduced as the distance increases and the angular error becomes similar. For relatively short distances, the additional path losses are over-

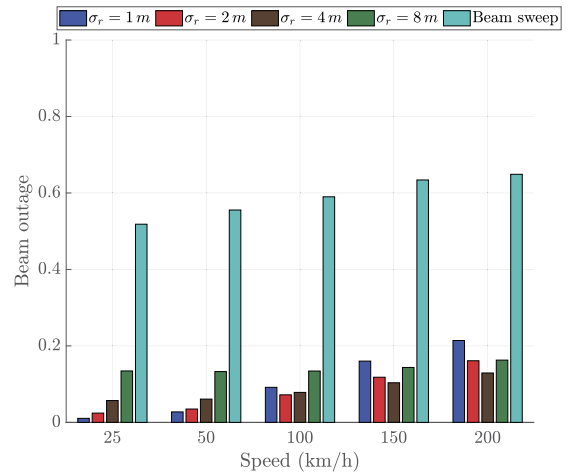


Fig. 5. Beam outage for different speed and standard deviation of the positioning error values.

come with more directive beams. The performance of the beam sweeping strategy in terms of SINR is similar to the proposed solution, even better for very high positioning errors, until 200 m. The use of the most directive beams during almost the entire trajectory leads to much probable outage locations and this has a big impact in the statistics when power is comparable to noise. In addition, the change in the trend of all curves coincides with those distances for which the received power is so low that the ICI becomes much lower than the noise and propagation losses have a direct impact on the SINR.

#### 4.2. Misalignment and gain loss

Optimized beams consider both channel capacity and beam outage probability. Therefore, it is a matter of interest to capture the evolution of the latter under various conditions. In this case, the simulated trajectories are limited to a coverage area of 200 m in which small positioning errors are still meaningful. It is also typical that highly demanding applications in terms of throughput as the ones offered by mmWave V2X are limited to a relatively small cell coverage.

The probability of the car to be outside the footprint of the chosen beam is as illustrated in Fig. 5. The values are given for speeds between 25 and 200 km/h and deviations of the vehicle position from 1 to 8 m. In light blue, the beam outage probability for the beam sweeping case is also shown. The consideration of the vehicle positioning (with a certain accuracy) really helps the BS to avoid large outage periods as seen in Fig. 5. The fact that finer beams are used for low  $\sigma_r$  values implies slightly larger loss in SINR. When the car speed is increased, this difference of using narrow (low  $\sigma_r$ ) and wide beams (high  $\sigma_r$ ) is more noticeable. However, the achievable SINR evolves as expected (Fig. 4). The average SINR degradation due to outage is much lower than the one due to the use of wider beams when the positioning error becomes higher. Targeting to provide accurate QoS for advanced vehicular use cases at mmWave bands, alternative optimization methods should be investigated to minimize the impact of outage.

Moreover, one could expect that outage increases both with the positioning error and the vehicle speed. For the former, this is true for relatively low speeds. However, this trend is not kept from 100 km/h forward. To understand this effect and provide a plausible explanation, Fig. 6 shows the ratio of usage of each beamset hierarchy level depending on the error. In this case, the velocity is fixed to 100 km/h. It is evident that better positioning allows to

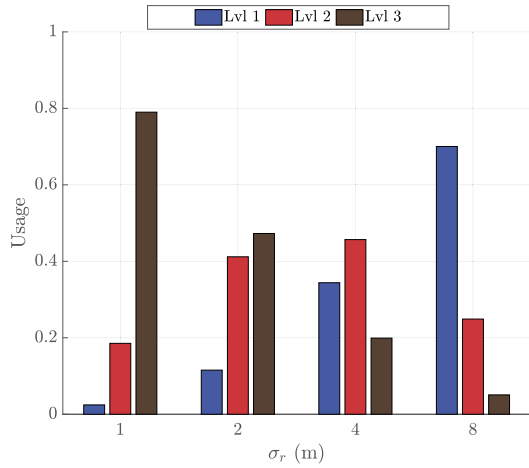


**Fig. 6.** Beamset hierarchy usage ratio for different values of the standard deviation of the positioning error when driving at 100 km/h.

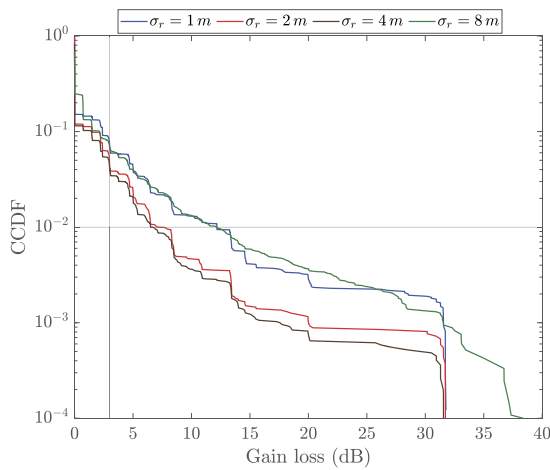


**Fig. 7.** CCDF of the gain loss due to beam misalignment at 100 km/h. Black lines indicate a 3 dB loss (vertical) and 1% probability (horizontal).

use more directive beams, whereas high errors imply widening the footprint at the expense of less gain.

Finally, the values in Fig. 5 are not directly linked to any reliability metric but they can provide a hint on how effective the energy focusing is. However, the degradation in terms of SINR or packet reception rate (PRR) must be provided for such kind of assessment.

The loss of gain due to beam misalignment is then depicted in Fig. 7. The values are calculated as the difference between the gain of the pattern resulting from the optimization towards the vehicle and the gain of the beam including the LOS direction at the same angles. Again, the speed of the vehicles is 100 km/h. The complementary cumulative distribution function (CCDF) of the gain loss is represented in such a way that one can somehow relate this parameter to a certain reliability level. For instance, regardless of the positioning accuracy, all beams suffer less than 3 dB losses on 94% of the cases. Inversely, with 1% probability, losses will be higher than 6.5 and 12.2 dB for {2, 4} and {1, 8} m accuracy, respectively.

#### 4.3. Effect of beam update period

Lastly, the impact of the beam update period on the link performance is studied. For the same highway scenario, the optimum beam is chosen with four update period: 20, 40, 80, and 160 ms. The same periods are used in the case of beam sweeping for com-

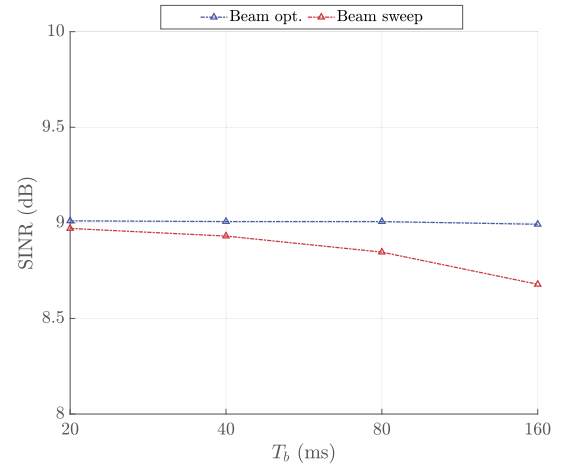


**Fig. 8.** Average SINR for different beam update periods.

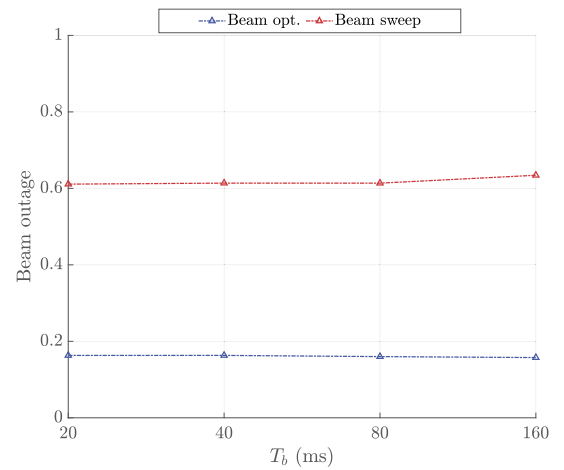


**Fig. 9.** Outage probability for different beam update periods.

parison. All vehicles drive at a constant speed of 100 km/h and they report their position every 200 ms with an accuracy of 2 m. Fig. 8 shows how the average SINR evolves for each case. On the one hand, the proposed beam optimization method outperforms the beam sweeping strategy for all beam update periods, especially when this value is increased, with up to 0.4 dB more SINR in average. The optimum beam considering both ICI and vehicle positioning also showcases a much more stable performance as the time between beam updates increases. On the other hand, it is of interest to evaluate the system-level performance in terms of beam outage probability. Again, the proposed beam optimization presents a very stable behavior as seen in Fig. 9, with values always below a 0.2. The beam sweeping approach, with high use ratio of very narrow beams, shows a slightly increased probability of beam outage for higher beam update periods.

#### 4.4. Comparison with other optimization methods

In order to evaluate the optimality of the proposed approach, it is compared to two different optimization algorithms. For a given beam update period (40 ms) and positioning accuracy (2 m), a subset of 10 vehicles is used to extract some quality parameters for two other optimization methods and compare them with the abovementioned results. In particular, the two chosen algorithms are: a global search with sequential quadratic programming (SQP) [38,39] and the genetic algorithm (GA) [40]. The former makes use of a large number of starting points to iteratively solve individual

**Table 2**  
Performance comparison between the three optimization methods.

Parameter	Beamset	SQP	GA
Avg. SINR (dB)	7.37	8.46	8.44
Avg. $P_{bo}$	0.02	0.24	0.19
Avg. Time (norm.)	1	402	830
Avg. $\Delta\theta_{-3\text{dB}}$ (deg.)	-	6.78	6.37
Avg. $\Delta\phi_{-3\text{dB}}$ (deg.)	-	13.0	12.83

problems. It allows to solve non-linear constrained problems, as it is the case. The optimization variables (beamwidth in azimuth and elevation) are restricted to a range of values and the maximization function is far from presenting a linear behavior. The second method, GA, is based on a natural-selection process, creating random children at each iteration from a subset of the parents in the previous stage. When the population and iterations are large enough, the solution converges to the optimum. The following settings are applied to both optimization methods:

- A total number of 500 trial points are initially used in the global search, which are reduced to 200 in successive iterations.
- The tolerance of the SQP and GA optimizer variables (beamwidth) is set to  $0.01^\circ$ .
- No thread parallelization is used in the optimization, which could partially alleviate the time consumption.

Table 2 presents the results for a subset of 10 vehicles with positions ranging between 150 and 250 m along their trajectories. The distance criterion is used in order to obtain meaningful mean values of SINR and outage, since it does not make sense to average power for very distinct distances between transmitter and receiver. The average calculation time for each optimization (normalized to the original beam search) and the average difference between the optimum beamwidth and the one chosen from the beamset are also given. As it can be stated, the use of optimization algorithms improves the achievable SINR at the expense of much larger computation times. Regarding the beam outage probability, it is much larger for the optimum beams as well, since they tend to lower beamwidth values. The goal function for the entire trajectory is maximized but it does not imply that all points are maximum. Additionally, being out of the beam does not necessarily mean that the received power is insufficient for an adequate decoding of data. For such analysis, higher layers should be implemented to calculate other parameters such as the packet error rate (PER).

## 5. Conclusion

This paper addresses the optimization of the antenna beamwidth in high-mobility V2N communication scenarios using massive antenna arrays at mmWave band. In particular, the information of the vehicle speed and position, assuming a certain error, are used to estimate the channel performance along the vehicle trajectory in terms of SINR and outage probability to optimize the antenna beam width. Analytical expressions are provided to estimate the ICI depending on the Doppler shift due to the vehicle speed and the accuracy when positioning the car in the scenario. The results are also compared to those obtained with a hierarchical beamset codebook in which the beam is refined after an initial tracking phase.

An increased performance in terms of SINR and throughput is shown when the antenna beamwidth is adapted according to the vehicle dynamics compared to the wide-spread beam sweep-

ing case. This is true even when a finite beamset is chosen, equal to the one used in beam sweeping. The main constraint of the proposed methodology concerns the accuracy when estimating the user trajectory but this is compensated in the optimization at the expense of reduced antenna gains. SINR and throughput are maximized when the vehicle position is known with better accuracy, whereas gain drops due to beam misalignment do not always follow this trend. Nevertheless, a loss smaller than 3 dB is given at least for 94% of the cases. The discussed optimization method also presents a very stable performance with beam update periods ranging from 20 to 160 ms.

## Declaration of competing interest

The authors declare that they have no known competing financial interests or personal relationships that could have appeared to influence the work reported in this paper.

## Acknowledgement

This work was partly funded by the Spanish Ministerio de Economía y Competitividad under the projects PID2019-107885GB-C31 and MDM2016-0600, the Catalan Research Group 2017 SGR 219, and “Industrial Doctorate” programme of the Agència de Gestió d’Ajuts Universitaris i de Recerca (2018-DI-084). The Spanish Ministerio de Universidades contributes via a predoctoral grant to the first author (FPU17/05561).

## Appendix A

In [41], Bello justified that, under slow-fading condition, one can define the channel fading terms by the two first terms of its series expansion. In 5G FR2 communications, the symbol period,  $T$ , is  $16.67 \mu\text{s}$  at most ( $\Delta f = 60 \text{ kHz}$ ). Moreover, according to the calculations in [6,29], typical values of the channel coherence time in mmWave V2I communications are strictly more than 1 ms. Hence, slow-fading condition is assumed to be fulfilled and the channel coefficients for the  $k$ -th subcarrier are expressed as:

$$h_k(t) = h_k(t_0) + h'_k(t_0)(t - t_0). \quad (\text{A.1})$$

The received signal in time, defined in (10), corresponds to the addition of all subcarrier symbols, that combined with (A.1) lead to the following expression:

$$r(t) = \frac{1}{\sqrt{NT}} \sum_{k=1}^N h_k(t_0) x_k e^{j2\pi f_k t} + \frac{1}{\sqrt{NT}} \sum_{k=1}^N h'_k(t_0)(t - t_0) x_k e^{j2\pi f_k t} + n(t). \quad (\text{A.2})$$

Then, the output of the  $k$ -th correlator is the one defined in (11). The three addends in (11) correspond to the signal, ICI and noise components. First, the symbol to be detected has a power, namely  $P$ , that is proportional to the transmit power divided by the channel path loss. The power perceived by the receiver will scale accordingly to the position with respect to the beam footprint. Assuming that the BS focuses to the estimated position of the vehicle, there will be a decrease of the signal strength mainly due to two factors: the error in positioning and the vehicle movement.

The second term in (A.2) must be carefully depicted, since both the beamforming antenna (gain and misalignment) and user movement (Doppler) influence the ICI power in different ways. The power of the ICI is then computed as

**Table A.3**  
Definition of terms in (A.5) for  $\tau = 0$ .

Variable	Definition
$C$	$e^{k_\theta (\cos \Delta\theta_\varepsilon - 1) + k_\phi (\cos \Delta\phi_\varepsilon - 1)}$
$A'_1$	$\frac{1}{2} k_\theta \sin(\Delta\theta_\varepsilon) \Delta\theta'$
$A'_2$	$\frac{1}{2} k_\phi \sin(\Delta\phi_\varepsilon) \Delta\phi'$
$B'$	$-j2\pi f_D \cos \theta_0 \cos \phi_0$
$\Delta\theta'$	$\frac{hv(\tan^2(\theta_0)+1)\cos\theta_0}{(D_0\cos\theta_0+h\tan\theta_0)^2}$
$\Delta\phi'$	$\frac{v\sin(\phi_0)}{D_0\cos\theta_0}$
$A''_1$	$(A'_1)^2 + \frac{1}{2} k_\theta \sin(\Delta\theta_\varepsilon) \Delta\theta''$
$A''_2$	$(A'_2)^2 + \frac{1}{2} k_\phi \sin(\Delta\phi_\varepsilon) \Delta\phi''$
$B''$	$B' - j8\pi f_D \left[ \sin \theta_0 \cos \phi_0 \Delta\theta' + \cos(\theta_0) \sin \phi_0 \Delta\phi' \right]^2$
$\Delta\theta''$	$\frac{2hv^2(\tan^2\theta_0+1)\cos^2\phi_0}{(D_0\cos\theta_0+h\tan\theta_0)^3}$
$\Delta\phi''$	$\frac{2v^2\sin\phi_0\cos\phi_0}{(D_0\cos\theta_0)^2}$
$D_0$	$D \frac{\cos\theta_0\cos\sin(\phi_0\cos-\alpha)}{\cos\theta_0\sin(\phi_0-\alpha)}$

$$I_k = \mathbb{E} \left[ \left| \frac{NT}{j2\pi} \sum_{\substack{l=1 \\ l \neq k}}^N \frac{h'_l(t_0)x_l}{l-k} \right|^2 \right] = I_1 + I_2 \quad (\text{A.3})$$

and it is decomposed in two parts, being  $I_1$  the crossed terms correlation and  $I_2$ , the self-correlation of all the undesired symbols at the  $i$ -th branch. Given zero-mean i.i.d. symbols,  $I_1 = 0$  and only the second term remains in the equation:

$$\begin{aligned} I_k = I_2 &= \left( \frac{NT}{2\pi} \right)^2 \sum_{\substack{l=1 \\ l \neq k}}^N \frac{1}{(l-k)^2} E[|h'_l(t_0)x_l|^2] \\ &= |R''_1(0)| P \left( \frac{NT}{2\pi} \right)^2 \sum_{\substack{l=1 \\ l \neq k}}^N \frac{1}{(l-k)^2}, \end{aligned} \quad (\text{A.4})$$

where  $R''_1(0)$  is the second derivative of the self-correlation function particularized for  $\tau = 0$ .

In (8), the temporal correlation of the LOS component is detailed. Both positioning and movement errors influence the channel correlation in magnitude and phase. The angles are referred with respect to the axes defined by the driving direction and the zenith. The bivariate von Mises distribution [33] is used to model the beam pattern, which extends the initial approach in [29] to both angular dimensions, and the two variables are assumed to be uncorrelated.

For  $\tau = 0$ , the second derivative of  $R_1$  can be expressed in the following form:

$$R''_1(0) = \mathbb{E} \left[ C(A''_1 + 2A'_1A'_2 + A''_2 + 2A'_1B' + 2A'_2B' + B'') \right] \quad (\text{A.5})$$

and each term is detailed in Table A.3. The undefined parameters are:  $v$  stands for the magnitude of the velocity vector,  $D$  is the LOS distance between the BS and the vehicle at the reported position and  $h$  is the height difference between both.

Considering a noise power that scales with the sub-channel bandwidth,  $N_0\Delta f$ , the SINR of the  $i$ -th subcarrier follows the expression detailed in (12).

## References

- [1] A. Pfadler, G. Jornod, A.E. Assaad, P. Jung, Predictive quality of service: adaptation of platoon inter-vehicle distance to packet inter-reception time, in: 2020 IEEE 91st Vehicular Technology Conference (VTC2020-Spring), 2020, pp. 1–5.
- [2] A. Kousaridas, R.P. Manjunath, J. Perdomo, C. Zhou, E. Zielinski, S. Schmitz, A. Pfadler, Qos prediction for 5g connected and automated driving, IEEE Commun. Mag. 59 (9) (2021) 58–64, <https://doi.org/10.1109/MCOM.110.2100042>.
- [3] S. Euler, A. Pfadler, L. Fernández Ferreira, H. Zhao, Spectrum needs of cooperative, connected and automated mobility, in: 2021 IEEE 93rd Vehicular Technology Conference (VTC2021-Spring), 2021, pp. 1–6.
- [4] T.E. Bogale, Adaptive beamforming and modulation design for 5G V2I networks, in: 2020 10th Annual Computing and Communication Workshop and Conference (CCWC), 2020, pp. 0090–0096.
- [5] M. Matalatala, M. Deruyck, E. Tanghe, L. Martens, W. Joseph, Simulations of beamforming performance and energy efficiency for 5G mm-wave cellular networks, in: 2018 IEEE Wireless Communications and Networking Conference (WCNC), 2018, pp. 1–6.
- [6] A. Pfadler, C. Ballesteros, J. Romeu, L. Jofre, Hybrid massive MIMO for urban V2I: sub-6 GHz vs mmWave performance assessment, IEEE Trans. Veh. Technol. 69 (5) (2020) 4652–4662, <https://doi.org/10.1109/TVT.2020.2982743>.
- [7] I. Maskulainen, P. Luoto, P. Pirinen, M. Bennis, K. Horneman, M. Latva-aho, Performance evaluation of adaptive beamforming in 5G-V2X networks, in: 2017 European Conference on Networks and Communications (EuCNC), 2017, pp. 1–5.
- [8] D. Kong, J. Cao, A. Goulianos, F. Tila, A. Doufexi, A. Nix, V2I mmWave connectivity for highway scenarios, in: 2018 IEEE 29th Annual International Symposium on Personal, Indoor and Mobile Radio Communications (PIMRC), 2018, pp. 111–116.
- [9] Y. Wang, K. Venugopal, A.F. Molisch, R.W. Heath, MmWave vehicle-to-infrastructure communication: analysis of urban microcellular networks, IEEE Trans. Veh. Technol. 67 (8) (2018) 7086–7100, <https://doi.org/10.1109/TVT.2018.2827259>.
- [10] M.K. Samimi, T.S. Rappaport, Ultra-wideband statistical channel model for non line of sight millimeter-wave urban channels, in: 2014 IEEE Global Communications Conference, 2014, pp. 3483–3489.
- [11] T.S. Rappaport, Y. Xing, G.R. MacCartney, A.F. Molisch, E. Mellios, J. Zhang, Overview of millimeter wave communications for fifth-generation (5G) wireless networks – with a focus on propagation models, IEEE Trans. Antennas Propag. 65 (12) (2017) 6213–6230, <https://doi.org/10.1109/TAP.2017.2734243>.
- [12] C.K. Anjinappa, I. Guvenc, Angular and temporal correlation of V2X channels across sub-6 GHz and mmWave bands, in: 2018 IEEE International Conference on Communications Workshops (ICC Workshops), 2018, pp. 1–6.
- [13] K. Guan, B. Ai, B. Peng, D. He, G. Li, J. Yang, Z. Zhong, T. Kürner, Towards realistic high-speed train channels at 5G millimeter-wave band—part I: paradigm, significance analysis, and scenario reconstruction, IEEE Trans. Veh. Technol. 67 (10) (2018) 9112–9128, <https://doi.org/10.1109/TVT.2018.2865498>.
- [14] J. Lorca, M. Hunukumbure, Y. Wang, On overcoming the impact of Doppler spectrum in millimeter-wave V2I communications, in: 2017 IEEE Globecom Workshops (GC Wkshps), 2017, pp. 1–6.
- [15] J.A. del Peral-Rosado, R. Raulefs, J.A. López-Salcedo, G. Seco-Granados, Survey of cellular mobile radio localization methods: from 1G to 5G, IEEE Commun. Surv. Tutor. 20 (2) (2018) 1124–1148.
- [16] G.M. Hoang, B. Denis, J. Härrri, D. Slock, et al., Distributed link selection and data fusion for cooperative positioning in GPS-aided IEEE 802.11 p VANETs, Proc. WPNC 15 (2015) 1–6.
- [17] G.E. Garcia, G. Seco-Granados, E. Karipidis, H. Wymeersch, Transmitter beam selection in millimeter-wave MIMO with in-band position-aiding, IEEE Trans. Wirel. Commun. 17 (9) (2018) 6082–6092.
- [18] H. Wymeersch, G. Seco-Granados, G. Destino, D. Dardari, F. Tufvesson, 5G mmWave positioning for vehicular networks, IEEE Wirel. Commun. 24 (6) (2017) 80–86.
- [19] T. Shimizu, V. Va, G. Bansal, R.W. Heath, Millimeter wave V2X communications: use cases and design considerations of beam management, in: 2018 Asia-Pacific Microwave Conference (APMC), IEEE, 2018, pp. 183–185.
- [20] N. Garcia, H. Wymeersch, E.G. Ström, D. Slock, Location-aided mm-wave channel estimation for vehicular communication, in: 2016 IEEE 17th International Workshop on Signal Processing Advances in Wireless Communications (SPAWC), IEEE, 2016, pp. 1–5.
- [21] I.E.E.E. Std, 802.15.3c-2009 (Amendment to IEEE Std 802.15.3-2003), IEEE Standard for Information Technology – Telecommunications and Information Exchange between Systems – Local and Metropolitan Area Networks – Specific Requirements. Part 15.3: Wireless Medium Access Control (MAC) and Physical Layer (PHY) Specifications for High Rate Wireless Personal Area Networks (WPANs) Amendment 2: Millimeter-Wave-Based Alternative Physical Layer Extension, Oct. 2009.
- [22] V. Va, T. Shimizu, G. Bansal, R.W. Heath, Beam design for beam switching based millimeter wave vehicle-to-infrastructure communications, in: 2016 IEEE International Conference on Communications (ICC), IEEE, 2016, pp. 1–6.

- [23] Y. Kang, H. Seo, W. Choi, Optimal receive beamwidth for time varying vehicular channels, in: 2020 IEEE Wireless Communications and Networking Conference (WCNC), IEEE, 2020, pp. 1–6.
- [24] Y. Feng, D. He, Y. Guan, Y. Huang, Y. Xu, Z. Chen, Beamwidth optimization for millimeter-wave V2V communication between neighbor vehicles in highway scenarios, *IEEE Access* 9 (2021) 4335–4350.
- [25] P. Petrus, J.H. Reed, T.S. Rappaport, Effects of directional antennas at the base station on the Doppler spectrum, *IEEE Commun. Lett.* 1 (2) (1997) 40–42.
- [26] S.J. Nawaz, N.M. Khan, M.N. Patwary, M. Moniri, Effect of directional antenna on the Doppler spectrum in 3-D mobile radio propagation environment, *IEEE Trans. Veh. Technol.* 60 (7) (2011) 2895–2903.
- [27] S. Jaeckel, L. Raschkowski, K. Börner, L. Thiele, QuaDRiGa: a 3-D multi-cell channel model with time evolution for enabling virtual field trials, *IEEE Trans. Antennas Propag.* 62 (6) (2014) 3242–3256.
- [28] Tiejun Wang, J.G. Proakis, E. Masry, J.R. Zeidler, Performance degradation of OFDM systems due to Doppler spreading, *IEEE Trans. Wirel. Commun.* 5 (6) (2006) 1422–1432.
- [29] V. Va, J. Choi, R.W. Heath, The impact of beamwidth on temporal channel variation in vehicular channels and its implications, *IEEE Trans. Veh. Technol.* 66 (6) (2017) 5014–5029, <https://doi.org/10.1109/TVT.2016.2622164>.
- [30] J.D. Parsons, A.S. Bajwa, Wideband characterisation of fading mobile radio channels, *IEE Proc. F, Commun. Radar Signal Process.* 129 (2) (1982) 95.
- [31] R.H. Clarke, A statistical theory of mobile-radio reception, *Bell Syst. Tech. J.* 47 (6) (1968) 957–1000.
- [32] W.C. Jakes, D.C. Cox, *Microwave Mobile Communications*, Wiley-IEEE Press, 1994.
- [33] K.V. Mardia, G. Hughes, C.C. Taylor, H. Singh, A multivariate von Mises distribution with applications to bioinformatics, *Can. J. Stat.* 36 (1) (2008) 99–109.
- [34] M.-D. Kim, J. Liang, J. Lee, J. Park, B. Park, H.K. Chung, Investigating the effect of antenna beamwidth on millimeter-wave channel characterization, in: 2016 URSI Asia-Pacific Radio Science Conference (URSI AP-RASC), 2016, pp. 1–4.
- [35] Z. Hanzaz, H.D. Schotten, Analysis of effective SINR mapping models for MIMO OFDM in LTE system, in: 2013 9th International Wireless Communications and Mobile Computing Conference (IWCMC), 2013, pp. 1509–1515.
- [36] Technical 3GPP, Specification Group Radio Access Network; Study on Evaluation Methodology of New Vehicle-to-Everything (V2X) Use Cases for LTE and NR; (Release 15), Technical Report (TR) 37.885, 3rd Generation Partnership Project (3GPP), version 15.3.0, June 2019.
- [37] 3GPP, Technical Specification Group Radio Access Network; NR; Physical channels and modulation; (Release 16), Technical Specification (TS) 38.211, 3rd Generation Partnership Project (3GPP), version 16.3.0, September 2020.
- [38] Z. Ugray, L. Lasdon, J. Plummer, F. Glover, J. Kelly, R. Martí, Scatter Search and Local NLP Solvers: A Multistart Framework for Global Optimization, vol. 19, 2007.
- [39] J. Nocedal, S. Wright, *Numerical Optimization*, Springer Science & Business Media, 2006.
- [40] D.E. Goldberg, *Genetic Algorithms in Search, Optimization, and Machine Learning*, Addison, Addison-Wesley, 1989.
- [41] P. Bello, Characterization of randomly time-variant linear channels, *IEEE Trans. Commun. Syst.* 11 (4) (1963) 360–393.

## CHAPTER 5

# VEHICLE ANTENNA DESIGN BASED ON WIRELESS CHANNEL PERFORMANCE

---

The paper included in this chapter, "Multi-Antenna 3D Pattern Design for Millimeter-Wave Vehicular Communications", details the procedure to assess the best vehicular distributed antenna system. In the horizontal plane, a set of panels are mounted on the car's roof with variable number of elements. Based on the achievable coverage and system-level performance under realistic conditions, the amount of panels and horizontal array elements are assessed. In the vertical plane, the radiation is shaped by means of Fourier synthesis in such a way that the scattering on the vehicle bodywork is minimized.

### 5.1 Publication

[J2] C. Ballesteros, L. Montero, G. A. Ramírez, and L. Jofre-Roca, "Multi-Antenna 3D Pattern Design for Millimeter-Wave Vehicular Communications," in Elsevier Vehicular Communications, vol. 35, article 100473, June. 2022, doi: 10.1016/j.vehcom.2022.100473.



# Multi-antenna 3D pattern design for millimeter-wave vehicular communications



Christian Ballesteros<sup>a,\*</sup>, Luca Montero<sup>a</sup>, Germán A. Ramírez<sup>a,b</sup>, Luis Jofre-Roca<sup>a</sup>

<sup>a</sup> Universitat Politècnica de Catalunya (UPC), Jordi Girona 31, Barcelona, 08034, Spain

<sup>b</sup> École Polytechnique Fédérale de Lausanne (EPFL), EPFL-STI-MAG, Bâtiment ELB, Station 11, Lausanne, CH-1015, Switzerland

## ARTICLE INFO

### Article history:

Received 7 September 2021

Received in revised form 27 March 2022

Accepted 18 April 2022

Available online 22 April 2022

### Keywords:

V2X

Beamforming

Arrays

## ABSTRACT

The transformation of the automotive industry towards ubiquitous connection of vehicles with all kind of external agents (V2X) motivates the use of a wide range of frequencies for several applications. Millimeter-wave (mmWave) connectivity represents a paramount research field in which adequate geometries of antenna arrays must be provided to be integrated in modern vehicles, so 5G-V2X can be fully exploited in the Frequency Range 2 (FR2) band. This paper presents an approach to design mmWave vehicular multi-antenna systems with beamforming capabilities considering the practical limitations of their usage in real vehicular environments. The study considers both the influence of the vehicle itself at radiation pattern level and the impact of the urban traffic on physical layer parameters. Connectivity parameters such as Signal-to-Interference-plus-Noise Ratio (SINR) and outage probability are optimized based on the array topology. A shaped beam in the vertical plane based on three preset radiating elements is proven to be robust enough against self-scattering effects on the vehicle body. Regarding the horizontal geometry, four panels on the roof's edges provide good coverage and link quality. The number of horizontal antennas per panel tightly depends on the required values of the link quality metrics, potentially leading to a non-uniform geometry between sides and front or back panels.

© 2022 The Author(s). Published by Elsevier Inc. This is an open access article under the CC BY-NC-ND license (<http://creativecommons.org/licenses/by-nc-nd/4.0/>).

## 1. Introduction

The automotive industry is experiencing a transformation to shape the mobility of the future. Amid rising consciousness about its contribution to global pollution, and with a view to reduce the still large number of traffic accidents [1], connectivity and automation have emerged as key drivers of the industry's evolution towards greener, safer and more efficient transportation. This trend towards Connected and Automated Mobility (CAM) establishes new challenges to cope with connectivity-related issues such as assuring a certain Quality of Service (QoS) based on reliable and high-speed wireless links.

Although we are currently in an early stage of this evolution, vehicles are already equipped with a variety of sensors that assist the driver in taking decisions. Likewise, the so-called Advanced Driver-Assistance Systems (ADAS) often take control of some manoeuvres. However, safety-wise, vehicles just rely on ADAS as a mean to mitigate imminent road risks. In terms of connectivity, vehicles make use of back-end data to obtain useful information along the journey. New vehicles are also capable to connect to the

Internet, but also connected road infrastructure is being deployed worldwide to help anticipating relevant information about unusual road conditions and potentially hazardous situations.

Intelligent Transportation Systems (ITS) make use of Vehicle to Everything (V2X) technologies, an umbrella term encompassing communications between the vehicle and the network, road-side infrastructure, pedestrians, and other vehicles. Early signs of successful V2X implementation have been experienced from 2019 onward [2], when the ITS ecosystem included support for a set of safety applications – namely, Day-1 use cases – in which nodes broadcast basic status messages to prevent road hazards. These V2X messages are to be transmitted with either IEEE 802.11p or Cellular V2X (C-V2X), technologies that coexist in the ITS Band (5.875 to 5.915 GHz) [3] harmonized for safety ITS.

The advent of advanced automotive use cases, with stringent requirements in terms of resource consumption [4,5], exemplify the need of enhanced features associated to New Radio (NR). Extended sensors or in-vehicle infotainment are expected to demand up to 1 GHz bandwidth with latency ranging between 3 and 50 ms and coverage up to hundreds of meters. In this context, although economically challenging for mass deployment, the use of the mmWave band (30–300 GHz), is essential to off-load the large volume of data required to realize the most demanding use cases.

\* Corresponding author.

E-mail address: [christian.ballesteros@upc.edu](mailto:christian.ballesteros@upc.edu) (C. Ballesteros).

One of the mmWave well-established enablers is beamforming, consisting in feeding an array of antennas to obtain sharp beams of concentrated power towards the intended receiver/transmitter set. The high gain obtained helps overcoming the intrinsically large propagation losses of mmWave channels. In [6], the use of mmWave antenna arrays for V2X communications is addressed showing larger data capacity when the number of on-board antennas increases. However, even assuming seamless beam-alignment, beams should not be considered arbitrarily narrow just accounting for the potential gain and throughput, since antenna array behavior limits these possibilities.

Even though some studies apply appropriate beam distributions, like the pre-defined set of beams used in [7], most of the assumptions found in the literature use oversimplified antennas where beamwidth and beam-steering are indiscriminately flexible, which is not the case in the performance shown by customary User Equipment (UE). Similarly, antennas and radiation patterns used in most works are rarely altered by the vehicle or their mounting location. In [8], radiation patterns show asymmetries depending on their position. In [9], the location of V2X antennas at 5.9 GHz is optimized, pointing its importance on the performance of the communications, whereas the authors in [10] conclude that channel capacity depends on antenna height and location. More recently, the 5G Automotive Association (5GAA) published a study regarding the use of distributed antenna systems for Fifth Generation of Mobile Communications (5G) vehicular communications [11]. Co-located geometries are compared with distributed ones for both side and Uu links at 6 GHz. In case of sidelink, the performance of distributed geometries is demonstrated to outperform co-located antennas in terms of coverage – achievable SINR – and signal blockage reduction. In [12], a measurement-based study on the achievable diversity of distributed antennas is also presented, as well as the channel dispersion under different scenario conditions, also at sub-6 GHz. More simplistic studies strictly based on the impact of the vehicular platform on a single-antenna radiation can be found in [13,14]. Also, the authors in [15–18] antenna designs with some degree of reconfiguration (at pattern or frequency level), but all designs still target sub-6 GHz, low-gain radiation.

Notwithstanding these results at lower frequency bands, only few studies have been found tackling these effects at mmWave, although the Third Generation Partnership Project (3GPP) has emphasized the need for accurate radiation models at these bands [19]. In [20], the coverage of several antennas mounted on a vehicle is studied based on their perceived path loss when the transmitting antenna is moved around the vehicle. There, the use of a distributed system at high positions (i.e., the roof) is envisioned as a potential solution for such users to reduce blockage effects. The authors in [21] already propose a multi-band antenna design for V2X application supporting both sub-6 GHz MIMO and mmWave beamforming. However, the proposal is evaluated independently from the vehicle and the environment. Similarly, in [22], a dual-band V2X antenna is proposed, but a moderate-directivity beam without steering capabilities is obtained.

In this work, a vehicular antenna system is tailored to meet the common requirements of mmWave V2X with a design methodology formulated to account for the effects of the vehicle on the radiation pattern and the surrounding traffic to optimize communication towards other vehicles. The results aim to serve as a reference design for antenna-aware V2X evaluations at mmWave, giving importance to feasible implementations and the potential interactions with the car and the scenario. The most similar approach found in literature is in [23], where a reconfigurable mmWave multi-beam panel is proposed to be located at both front and rear windshields of the vehicle. However, that design targets solely to the elevation problem and the study does not consider azimuth coverage nor the scattering effect of the vehicle. In the present

manuscript, the elevation problem is solved with a synthesized pattern, whereas a complete azimuth coverage is studied depending on the number of panels and radiators in the horizontal plane.

## 2. Considerations for the design of mmWave V2X antenna systems

The comparatively narrow spectrum portions available at frequency bands below 6 GHz (sub-6 GHz) fall short at fulfilling automotive-grade requirements like reliability, especially due to the expected large volumes of data to be exchanged. For instance, at 5.9 GHz, LTE-V2X delivers an average of 60% Packet Reception Rate at 60 km/h in urban scenarios [24]. 5G-V2X is expected to increase this metric [4], but the 99.99% reliability needed by highly-automated applications like platooning or sensor information sharing [25] cannot be met considering the high channel utilization rate expected at sub-6 GHz V2X bands. This motivates the use of larger bandwidths available at mmWave frequencies.

A common misconception related to the use of mobile mmWave is that propagation losses are prohibitive. However, as it is true that free-space path loss (FSPL) scales with the second power of frequency, it is also true that the effective antenna aperture does so. Therefore the feared FSPL can be compensated without increasing antenna space regardless of the operation frequency. On the other hand, when real-life propagation factors such as multipath fading, shading by obstacles, and atmospheric effects (i.e., water vapor and oxygen absorption, or rain) are included, path losses increase can be from mild to dramatic depending on the specific frequency band [26]. Fortunately, we can take advantage of the fact that the physical size of radiating elements becomes smaller as frequency grows. This fact allows packing more antennas without dramatically increasing the overall space. This, in combination with ingenious array design, allows to overcome most of the propagation-related losses.

The inherently directive nature of mmWave channels fosters the use of high gain antenna systems to exploit either direct Line-of-Sight (LOS) or indirect Non Line-of-Sight (NLOS) paths with narrow beams towards the dominant incoming or outgoing wave direction [27]. This comes with the additional challenge of beam alignment that may lead to unacceptable outage probabilities for arbitrarily narrow beams with low-accuracy, or low-rate beam updates [28]. Given this potential source of signal impairments, gain and beamwidth need to be carefully designed, as they are strictly related to the number of antenna elements in the array. Unless sophisticated methods are used, it is not feasible to assume low-cost and low-complexity vehicular arrays with focusing and defocusing capabilities to adapt their beam according to the channel state. Flexible arrays and fine phase resolution would lead to increased costs in the Radio Frequency (RF) processing, and robust phase shifters would be required [27]. It is also worth mentioning undesired effects such as sidelobes or scattering on the vehicle body when the beam is steered far from the broadside. All those considerations must be carefully depicted and addressed when designing an adequate geometry of the antenna array.

Conventional monopoles placed on the rooftop are widely used to obtain omnidirectional radiation patterns in vehicles at sub-6 GHz bands. However, the directional nature of the intended links at mmWave motivates a different antenna system topology, as in the absence of strong multi-paths, and given the channel losses, power radiated in unintended directions is practically lost. Therefore, vehicular beamforming antenna systems at mmWave must henceforth be arranged for sectorized coverage, each handled by a different array, to achieve an aggregated effective coverage similar to that of the monopole in the lower frequencies. Antenna arrays have a limited steering range with stable single-beam radi-



**Table 1**  
Multi-panel antenna configurations supported by 3GPP Rel. 16.

Antenna ports	Panels	Antenna element distribution in array
8	2	
16	2	
	4	
	2	
32	2	
	4	
	2	
	4	

ation, outside of which increased sidelobes and potential grating lobes increase undesired radiation and reduce gain.

5G conceives these systems as multi-panel antennas, giving support to a set of virtual antenna configurations [29] shown in Table 1 [30] – notated here as  $N$  (columns, horizontally)  $\times$   $M$  (rows, vertically) antenna elements per panel. 5G support currently allows for a maximum of 32 controllable feeding weights to map on each antenna element, enabling up to 16 cross-polarized antenna elements. In the table, the configurations backed by the 3GPP are classified according to the number of panels ( $K$ ) and antenna ports ( $2 \times N \times M \times K$ ). For equal amount of ports, different geometries are allowed given the number of panels by arranging the antennas accordingly on each panel. The so-called codebooks establish the weights for each antenna port and therefore define a pre-configured set of beams steered to different angles.

Regarding coverage, it is reasonable to conceive the challenge of mmWave V2X antennas as separated in vertical and horizontal problems. On the vertical plane (i.e., in elevation,  $el$ ), the goal is ensuring proper coverage of vehicles and infrastructure. It is safe to assume that vehicles will be in small elevation values ( $el \simeq 0^\circ$ ), whereas infrastructure will generally be around  $0^\circ < el < 30^\circ$ . Infrastructure appearing at higher  $el$  angles is assumed closer in distance and less radiated power can be assigned to those directions. On the horizontal plane (i.e., in azimuth,  $az$ ), the required angles to reach the surrounding nodes will be relatively fast-changing, and no difference between azimuths can be easily set for coverage. Thus a vehicular beamforming antenna system can then be designed with steering capabilities to cover the entire horizontal plane, while having a suitable fixed configuration on the vertical plane. Arrays, thus, can be as simple as Uniform Linear Arrays (ULA).

### 3. Methodology

The use of mmWave for mobile communications poses several concerns on the allocation of antenna resources on the UE end of the link. The proposed methodology obeys both performance and cost-awareness criteria to evaluate different array designs. The parameters to analyze include the number of panels (arrays) on the car, the number of antenna elements per panel, and their most suitable location on the car.

Initially, an analytical study of the array geometry is performed based on the achievable array factor for both elevation and azimuth radiation. Then, the electromagnetic simulation of the array radiation is carried out with Altair FEKO's Multi-Level Fast Multipoles Method (MLFMM) solver. A basic rectangular patch is used

**Table 2**  
Configuration of urban vehicular traffic modeling for the case scenarios under evaluation.

Description	9 blocks of Manhattan Grid
<b>Channel model</b>	3GPP TR 37.885 Urban LOS/NLOSv [34]
<b>Lanes</b>	2 in each direction
<b>Lane width</b>	3.5 m
<b>Grid size</b>	433 x 250 m
<b>Simulation area</b>	1299 x 750 m
<b>Vehicle velocity</b>	60 km/h
<b>Intersection turn probability</b>	Going straight: 50%
	Turning left: 25%
	Turning right: 25%

as radiating element and a customizable number of elements is placed for each array geometry. In order to make the numerical simulations as time-efficient as possible, the isolated array is first simulated with this method. Then its near-field is combined with the geometry of the car using an equivalent source consisting of an aperture of  $81 \times 81$  infinitesimal dipoles located at the antenna boundaries and placed on each position to be analyzed. The large electric size of the vehicle at mmWave frequencies entailed the use of Physical Optics (PO) to obtain the far-field radiation of the entire structure. To further improve calculation time, the entire bodywork, windows and windshields are considered as Perfect Electric Conductor (PEC), a model supported by reported measurements of the reflection coefficient of glass at mmWave [31].

Finally, the simulated patterns are tested in a typical Manhattan urban environment to assess their link-level performance in 5G-V2X-like communications. For that purpose, two more tools are used: one for the traffic simulation and another one to obtain the wireless channel behavior between communicating pairs. On the one hand, the realistic traffic of the urban grid is obtained with Simulation of Urban Mobility (SUMO) [32]. It allows to launch several simultaneous vehicle trajectories considering the distribution of the streets and the rest of the environment. In the simulation, vehicles are dropped in a way that the distance between the rear bumper of a vehicle and the front bumper of the following vehicle in the same lane follows an exponential probability distribution where the mean is 2 m at the velocity configured in each corresponding lane. The size is assumed  $5 \times 2 \times 1.5$  m for all vehicles, which is later used to determine whether other nodes in the scenario block the direct path between two communicating ends. The vehicles drive at 60 km/h along random trajectories within a grid made by 9 buildings that create orthogonal streets of 4 lanes each (2 per direction). More details about the scenario can be found in Table 2. In this study, traffic density is kept constant since the estimation of the interference level is not using traffic information. The impact of that parameter is mainly expected to degrade the link SINR while increasing channel usage, but further investigation of that issue may be required.

On the other hand, once the trajectories are obtained, the previously calculated radiation pattern is applied to each vehicle position to calculate the wireless channel coefficients between random pairs of vehicles with the Quasi Deterministic Radio Channel Generator (QuaDRiGa) tool [33]. It makes use of Geometry Based Stochastic Channel Model (GBSCM) to estimate the behavior of a wireless channel, provided that there is a suitable trade-off between repeatability, generalization and accuracy compared to ray-tracing simulators or purely statistical models. The proposed simulation framework takes the urban channel models in [34] to estimate the distribution of the scatterers and their angular contribution is then weighted by the radiation to be tested in each case and coherently added at the receiver side.

All proposals are evaluated and designed at 28 GHz because evaluation procedures by the 3GPP already consider this band for

all V2X combinations [34], and it is the first 5G mmWave band being deployed in selected cities and implemented in smartphones.

#### 4. Design of the multi-antenna beamset

The design of the antenna system is first studied in terms of the required coverage. To maximize the radiation to intended directions of individual array elements, the initial step to propose an adequate antenna system is to find the most suitable location on the vehicle. Then, the problem is divided in two dimensions: vertical and horizontal. Finally, the designed pattern is evaluated with a real planar array to be mounted as a vehicular UE panel.

##### 4.1. On-vehicle placement

The optimum placement of the antenna arrays is the first issue to be addressed before proposing a particular geometry. Radiating elements surrounding the vehicle bodywork are strongly influenced by the latter, so an adequate positioning is paramount. Antenna radiation of sub-6 GHz vehicular antennas is a topic that has been extensively studied in the literature. Typical single-element omnidirectional can be achieved with shark-fin or monopole structures on top of the roof. Some available literature presents the radiation characteristic of such antennas [35,36]. Other manuscripts discuss alternative antenna locations, still at conventional frequency bands. In particular, the authors in [8,37] propose diversity-enabling positions on the sides and roof of different vehicles. In [38], the radiation and coupling of more directive elements is also considered. Bumper antennas achieve better isolation, as expected. But the use of highly directive antennas is able to compensate that issue even in the case of roof panels, achieving very low coupling factors.

In mmWave V2X, the use of multi-element beamformed patterns is implicit and they are particularly influenced by the environment in the proximity of the antenna. Additionally, full coverage is usually achieved with distributed geometries at different locations. As stated by the 5GAA in [11], typical implementations of Distributed Antenna Systems (DASs) consist of a central unit inside the vehicle and several antenna units around its bodywork. The latter can be implemented on the roof, with good azimuth coverage and clear view of high-elevation angles, or on the bumpers, glasses or mirrors, achieving more limited coverage. The sectorized disposition of such systems not only present aesthetic challenges but cable losses are also a concern for engineers. Antennas placed at the edges of the roof present a good balance of cable losses with regard to the other options and also can benefit from the curvature of these edges to promote an unnoticeable integration for any required antenna orientation. Antennas placed on the bumpers are limited to forward and backwards radiation, which is suitable for Cooperative Adaptive Cruise Control (CACC) [39]. Vehicle radars operating in the W band are commonly mounted on the front and rear bumpers for that reason, but alternative positions can be also a matter of study as in [40]. The surrounding bodywork poses additional issues in terms of signal blockage when the antennas are located there and this is partially studied in [20], where the path loss of a single radiating element on different positions along the vehicle is calculated. Then, placing antennas at the roof's edges can leverage some non-invasive parts for integration, such as the rear roof spoiler – where some vehicles already embed antennas – or the in-cabin rear-view mirror.

Fig. 1 illustrates a reference coordinate system originating in the roof's frontal edge position, where the orientation of the array is determined by the  $el_o$  angle that the normal of the array's surface points to. The orientation of the array has a strong influence on the achievable coverage, as later demonstrated in the following sections. In the case of a DAS, the same vertical orientation is kept

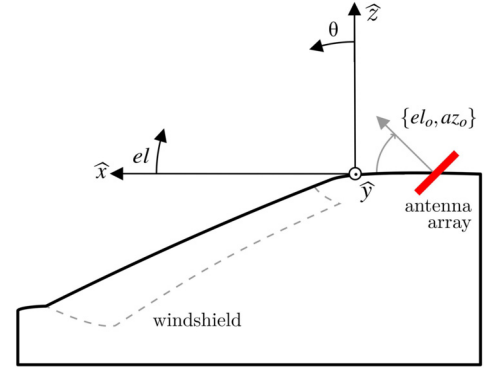


Fig. 1. Reference coordinate system.

for all available panels regardless of their position in the horizontal plane.

##### 4.2. Vertical plane coverage

As previously mentioned, a reasonable approach to solve the coverage challenges on the vertical plane is designing a suitable non-steerable beam that could give support for both Vehicle-to-Vehicle (V2V) and Vehicle-to-Infrastructure (V2I) links. For this purpose, Fourier synthesis is used for pattern design, being a widely acknowledged method that minimizes the Root-Mean-Square Error (RMSE) metric between the desired and synthesized beams [41]. In addition, the proposed arrays are to be located on the roof's edges following the criteria mentioned in the previous section.

The goal function to shape the desired vertical coverage is expressed in terms of the elevation Array Factor (AF), defined as a function of  $\theta = 90^\circ - el$ ,  $-90^\circ \leq el \leq 90^\circ$ . An optimized AF directly relates to the final beam radiation, following  $\vec{E} = AF \cdot \vec{E}_0$ , where  $\vec{E}$  and  $\vec{E}_0$  represent the electric field radiated by the array and the antenna element, respectively. Then, an appropriate beam for V2X applications can be pursued by designing an adequate goal AF. We define it as the following piece-wise function:

$$AF_{goal}(\theta) = \begin{cases} \cos(\theta_1) / \cos(\theta) & 0 \leq \theta < \theta_1 \\ 1 & \theta_1 \leq \theta \leq \theta_2 \\ 0 & \text{otherwise} \end{cases}, \quad (1)$$

where radiation is minimized for angles exceeding  $\theta_2$  to address the interfering reflections from the vehicle's body, while it is maximized for typical radiation directions, from  $\theta_1$  to  $\theta_2$ . To avoid nulls when  $\theta \rightarrow 0$ , the AF is defined to be proportional to  $\sec(\theta)$  in the range up to  $\theta_1$ . Assuming a constant height for infrastructure nodes, this would compensate for the FSPL associated with distance.

To synthesize the goal function, the AF is described as a function of  $\psi = kd \cos \theta + \alpha$  to capture the effects of inter-element spacing ( $d$ ), frequency ( $k = 2\pi f / c_0$ ), and progressive phase ( $\alpha$ ) [41]. For this method to work properly,  $AF(\psi)$  must be specified over one entire period  $|S_\psi| = 2\pi$ , regardless of the size of the visible region. The followed procedure to obtain the weights to synthesize the goal function with is described by:

$$AF(\theta) \rightarrow AF(\psi_{\in(-\pi, \pi)}) \rightarrow AF(\psi_n) \rightarrow a_m, \quad (2)$$

where the  $a_m$  coefficients are a reduced set of the sampled array factor  $AF(\psi_n)$  through an  $N_{pts}$  Inverse Discrete Fourier Transform (IDFT). The goal function can be fairly recreated by an odd number of antenna elements ( $M$ ), arranged vertically and fed with a signal amplitude and phase dictated by the complex value of  $a_m$ . To

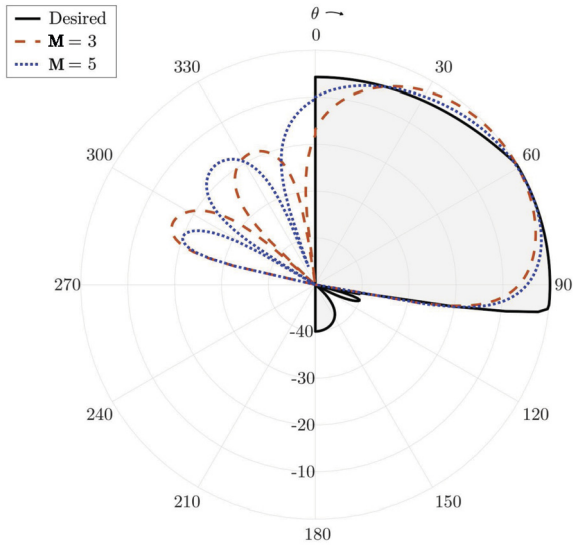


Fig. 2. Synthesized patterns with different number of array elements.

account for the possible antenna orientations, the synthesis is realized for different possible antenna pointing directions, aiming for the lowest RMSE, by rotating the goal AF according to the orientation being analyzed.

Then, a first analytical study is performed based on the achievable array factor with a variable number of antennas in elevation. This can be expressed with the following IDFT [41]:

$$AF(\psi) = \sum_{m=0}^{M-1} a_m e^{jm\psi} \quad (3)$$

The weights in (3) are those obtained from the Fourier synthesis of the piece-wise function described in (1).

$$a_n = \frac{1}{2\pi} \int_{-\pi}^{\pi} AF_{goal}(\psi) e^{-jn\psi} d\psi \quad (4)$$

The array synthesis on the vertical plane is set for the most restricting side of the car in terms of self-induced reflections: the front. In this case, the start of the established maximum for V2I is fixed as  $\theta_1 = 60^\circ$ , according to typical V2I LOS angles.  $\theta_2$  is thoughtfully chosen depending on the angle at which reflections from the vehicle start being significant. This threshold is set as  $\theta_2 = 105^\circ$  for this vehicle model, giving a  $5^\circ$  margin to be generalized for other models.

The resulting goal AF can be reasonably synthesized with a small number of vertical elements. Fig. 2 represents the resulting theoretical pattern in elevation for 3 and 5 elements and the desired piece-wise function. In this case, the effect of the car is still not considered.

The RMSE of the synthesized solution compared to the goal AF is now calculated for  $M = \{3, 5, 7, 9\}$  and for the whole range of  $-90^\circ \leq e_{l_0} \leq 90^\circ$  with a  $1^\circ$  step. Those values for  $e_{l_0} < 0$  can be neglected, since the broadside direction of the array will be pointing directly towards the vehicle's bodywork, contrary to the design criteria to minimize its scattering. In this regard, the results in Fig. 3 point that increasing  $M$  shows little improvement on RMSE compared to the benefits of choosing the optimum  $e_{l_0}$ , especially considering the increased cost and complexity arising from a larger number of antenna elements. All the simulations find a local minimum for a certain  $e_{l_0}$ , which in all cases is very close to  $80^\circ$ , and suggest that the smallest number of antenna elements ( $M = 3$ ) sufficiently fulfills the needs for cost-effective coverage.

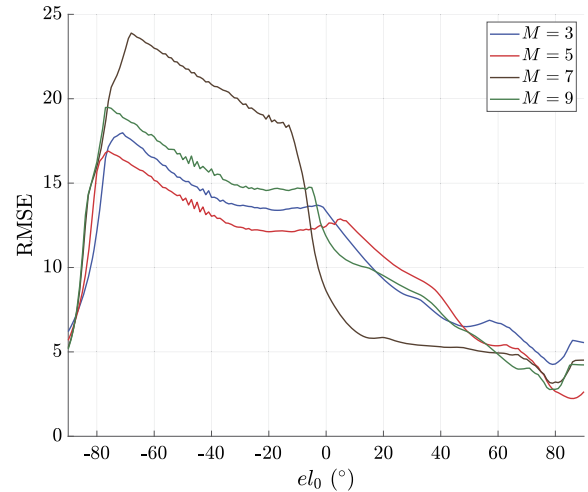


Fig. 3. RMSE in elevation varying array elements and tilt.

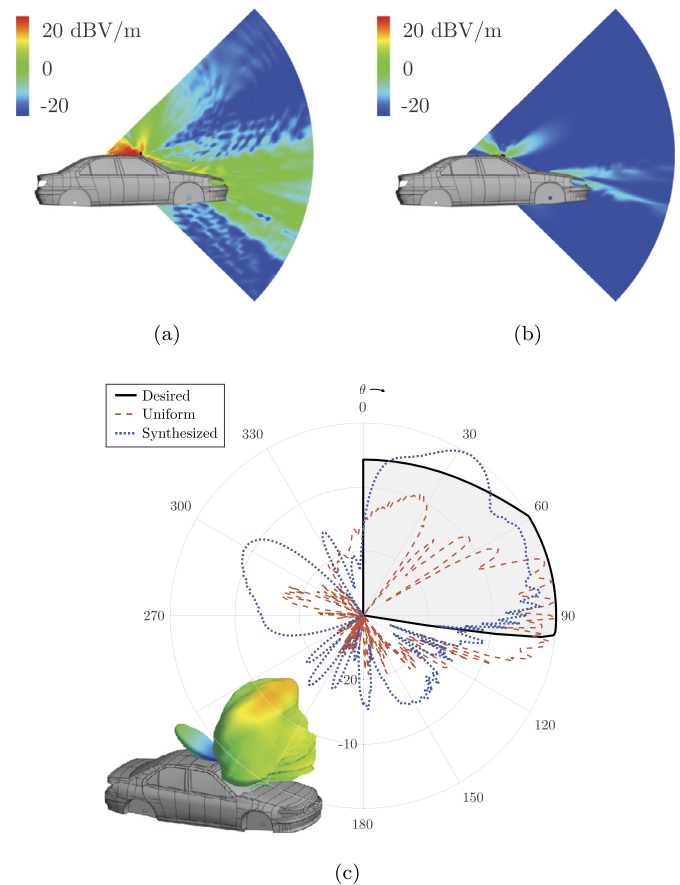
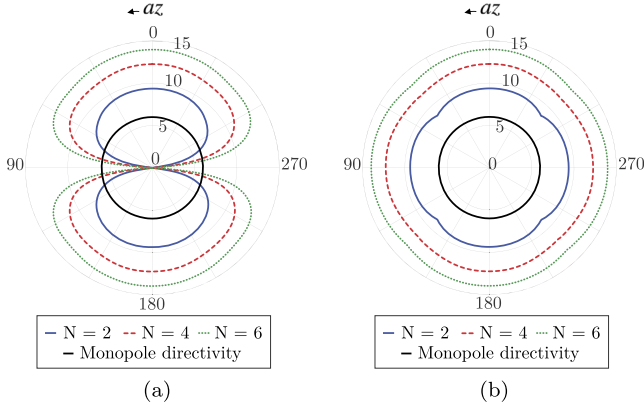


Fig. 4. Electric field scattered by the body of the vehicle when uniform feeding is applied in (a) and using the proposed 3-element synthesized pattern in (b). The overall front array radiation in presence of the vehicle is represented in (c).

To validate the suitability of the proposed solution, the scattered fields on the car of the proposed geometry with the optimized feeding and orientation are compared to those obtained with a uniformly fed array. Then, the radiation of the patch array mounted on the roof is numerically computed. As expected, the influence of the vehicle on the radiation pattern is substantially reduced as seen in Fig. 4. In Fig. 4a and Fig. 4b the distorting scattered fields due to the vehicle body are compared when uniform or the proposed synthesized feeding is used for 3 vertical antenna elements. The vertical radiation pattern accounting both for the



**Fig. 5.** Aggregated directivity for different  $N$  when (a)  $K = 2$  and (b)  $K = 4$  in the horizontal plane.

vehicle scattering and the array radiation is depicted in Fig. 4c. The desired AF is also shown as a reference. The main drawback of the synthesized pattern relates to the appearance of stronger back-radiation effect in the order of  $-9$  dB compared to the maximum.

#### 4.3. Horizontal plane coverage

Designing the optimum beam for the horizontal plane requires an additional knowledge on the propagation environment in which the vehicle is expected to communicate. As previously stated, sharp, high-gain beams will require complex, fast and accurate beam-alignment methods to prevent misalignments, but it could be a must to obtain large coverages for certain use cases.

As a first step, the horizontal coverage is studied in terms of the analytical aggregated radiation pattern in order to devise an adequate panel arrangement to use as baseline. To establish the configuration with lowest cost and complexity relying on the radiation pattern, a reasonable quality factor to validate can be based on obtaining monopole-like radiation, that is, being capable of an all-around coverage.

A convenient way to evaluate this monopole-like behavior is visualizing the aggregated radiation pattern, corresponding to the maximum envelope of the gains obtained for each steered beam enabled by the system. This is evaluated for the case of sectorized antenna systems with  $K = \{2, 3, 4, 5, 6\}$  arrays (panels) with  $N = \{2, 3, 4, 5, 6\}$  horizontal elements. For each  $K_i$ , the corresponding array is oriented towards  $az_{0i,j} = j \times 360^\circ / K_i$ , where  $j = 0, 1, \dots, K_i - 1$ , to cover their corresponding sector with a required steering range of  $360^\circ / K_i$ . Scenario evaluations suggest that  $az \simeq \{0^\circ, 90^\circ\}$  are the most common Angle of Departure (AoD) or Angle of Arrival (AoA), so this formulation motivates that the frontal ( $az_0 = 0^\circ$ ) and rear arrays ( $az_0 = 90^\circ$ ) should be always present. The sectorized coverage of each panel is achieved with a predefined set of beams, i.e., a beamset, obtained with a Discrete Fourier Transform (DFT) codebook defined by the total number of horizontal elements [42,43]. For a phase-shifted DFT codebook with a center beam towards the broadside direction, the following expression is used:

$$a_n^l = \frac{1}{\sqrt{N_B}} \exp \left\{ -j \frac{2\pi n(l - \frac{N_B+1}{2})}{N} \right\} \quad (5)$$

where  $a_n^l$  denotes the weight of the  $n$ -th horizontal element when the  $l$ -th beam is to be created and  $N_B$  is an odd number of beams, so  $l = 1, \dots, N_B$ . In this case,  $N_B = N + 1$ . For illustration, Fig. 5 presents the aggregated directivity for  $K = \{2, 4\}$  and  $N = \{2, 4, 6\}$

**Table 3**

Maximum scan loss (in dB) obtained with different array configurations.

$N$	2	3	4	5	6
$K = 3$	1.9	1.5	1.0	0.9	0.8
4	0.7	0.6	0.5	0.6	0.6
5	0.3	0.4	0.4	0.5	0.4
6	0.2	0.3	0.3	0.3	0.3

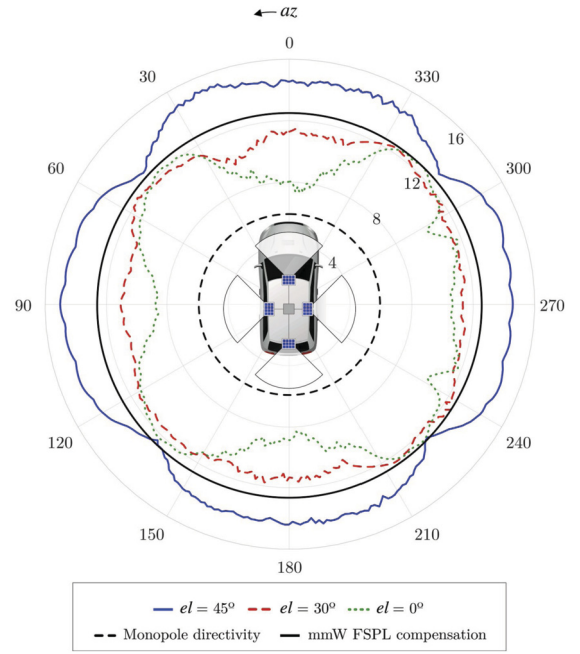


**Fig. 6.** Aggregated horizontal pattern for representative elevation cuts when the synthesized pattern is used together with a  $K = N = 4$  and  $M = 3$  configuration mounted on the vehicle.

when solely the array geometry without the influence of the vehicle is used. The simulated arrays are treated as horizontally-aligned ULAs, maintaining the independence between the horizontal and vertical problems. These plots showcase the broadening coverage as the number of arrays and antenna elements increase, using as a reference the maximum directivity of a conventional monopole, but also low directivity regions appear when the number of panels is small. The maximum scan loss perceived by the defined configurations within the steering range of each array is presented in Table 3. As seen in Fig. 5, the gain drops at the edge of the required steering range accentuates for smaller  $K$ , and improves for greater  $N$ , thus achieving smaller scan loss values. From  $K \geq 4$ , the scan loss does not substantially improve by increasing  $N$ , and even for  $K = 4$  scan loss never exceeds 1 dB for any angle and  $N$ . This is directly reflected in the aggregated directivity variation, which presents a ripple smaller than 1 dB reflecting a monopole-like form factor.

Finally, the aggregated horizontal pattern for the case of  $K = N = 4$  at different elevation angles when the array is placed on the vehicle roof's edges is presented in Fig. 6. The patterns are now calculated by means of numerical simulations with FEKO considering the antenna and the vehicle geometry. In the vertical plane, three elements are used to shape the beam proposed in Section 4.2 and the orientation of the arrays is  $el_0 = 80^\circ$ . The maximum gain of the whole system is 14.6 dB, experienced in  $(az, el) = (0^\circ, 45^\circ)$ . This shows how the radiation pattern, despite the synthesis of the vertical coverage, presents the highest intensity at elevation values beyond the goal range. In any case, the gain in the  $el = \{0^\circ, 30^\circ, 45^\circ\}$  cuts always exceeds  $\{12.4, 9.8, 7.4\}$  dB,

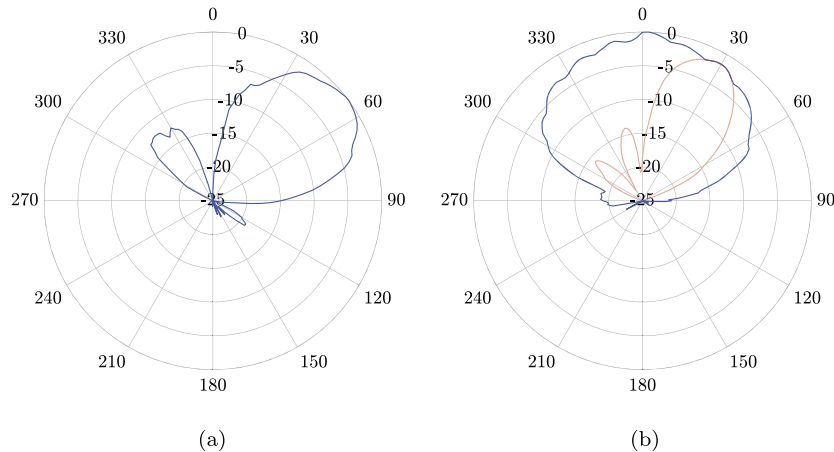


Fig. 7. Measured radiation of the antenna panel in (a) vertical and (b) horizontal planes.

respectively, thus achieving higher gains than a monopole (dashed circumference). The coverage also compensates the increased FSPL of mmWave compared to sub-6 GHz systems, as reflected in the reference circumference in Fig. 6. The solid black line indicates the gain increase needed to overcome the additional FSPL of moving from 5.9 to 28 GHz.

#### 4.4. Experimental validation

The proposed antenna system is lastly validated by means of an experimental demonstration with an in-house manufactured antenna array. The module corresponds to one of the panels to be mounted on the roof of the vehicle. As stated below, the array must allow the user to horizontally steer the beam to achieve continuous scanning in the panel sector ( $\pm 45^\circ$ ), while minimizing the scattering on the bodywork thanks to a shaped beam in the vertical dimension. In particular,  $N = 4$  radiating patches are used in the horizontal plane, whereas  $M = 3$  elements are vertically arranged to synthesize the desired pattern from Section 4.2.

The array radiation is measured in a controlled environment purposely built for the measurement of mmWave and THz antennas. The element weights are set thanks to a beamformer IC in the n257 5G band (the F5288 from Renesas Electronics). During the tests, the array acts as the receiving end and a reference horn is used as the transmitter at a distance of 900 mm to measure the far-field pattern.

Fig. 7 shows the measured normalized radiation in both vertical and horizontal planes of a single panel. The shape of the vertical beam approximates the theoretical pattern. However, the gain towards  $\theta = 90^\circ$  is degraded due to a narrower element radiation than expected (it must be reminded that the array is tilted  $80^\circ$  upwards in elevation). This issue must be addressed with a proper broadening of the beam for a successful coverage in V2V scenarios. Out-of-coverage radiation is limited below  $-12.2$  dB to the maximum gain, corresponding to a backwards sidelobe. Regarding the horizontal pattern, a beamset composed of 9 beams covers  $90^\circ$  in azimuth with a maximum scan loss of 3.7 dB. Besides the aggregated pattern, one individual beam towards  $30^\circ$  is shown for instance. Sidelobes have a maximum normalized gain of  $-12.5$  dB when the beamset is fixed at largest coverage angles.

### 5. Antenna system for mmWave V2V

From previous section, it is deduced that a 4-sector configuration with antennas on the roof's edges is an adequate trade-off between complexity and cost. In addition, the use of 3 antennas per RF chain with vertical beam shaping reduces the impact of

scattered fields due to the vehicle body and induces better steering capabilities. However, the number of array elements in the horizontal plane is still open to discussion in light of the similar aggregated coverage regardless of  $N$  when  $K = 4$ . Then, different antenna solutions are provided and evaluated under realistic V2V channels to assess their suitability to maximize the quality of communications. V2V is chosen for this evaluation given its challenging quality assurance due to the fast varying channels. A similar approach could be carried out for V2I or Vehicle-to-Network (V2N), in which one of the communicating ends is static.

The support of 3GPP to manage this system is compatible with the vertical beam-shaping of the arrays, which is based on fixed feeding coefficients and can be set with pre-configured hardware and be transparent to the beamforming control. 5G codebooks for this multi-panel configuration constrain analog beamforming in the system to the horizontal plane, and define weights to obtain  $O \times N \times M$  beams per panel – being  $O$  the DFT oversampling factor that defines the sweeping steps [44].

As stated in Section 3, each array configuration is tested in a realistic urban scenario where random vehicle pairs try to communicate using 5G-V2X-like links. Two visibility conditions are assumed: LOS and NLOS due to other vehicles (NLOSv) [34]. In total, up to  $N_p = 1000$  vehicle pairs are simulated for TX-RX distances ranging from 20 to 250 m. For each pair, the best beam pair is determined with  $T_b$  periodicity by sweeping both beamsets and reporting the combination with maximum Reference Signal Received Power (RSRP). Given the large number of beams for high  $N$  values, an initial full-azimuth scan is performed when the link is established, but only a reduced set of  $N_b = 5$  beams is used from that point forward. Along all trajectories, the perceived power by the receiving vehicle is calculated for the chosen beam pair. Then, assuming a certain 5G-V2X physical-layer configuration, it is possible to map those values to the SINR and, hence, an achievable throughput. No overhead is assumed in the calculation since it is not expected to differ between configurations when beam sweeping is performed for an equal  $N_b$ . All parameters concerning the simulations are depicted in Table 4.

For each link and time sample, the SINR is calculated assuming a noise power of  $P_N = -174 + 10 \log_{10} B + NF$  and a 2 dB margin accounting for additional interferences. This value is then translated to the maximum spectral efficiency supported by the current channel for a target Block Error Rate (BLER) with the following expression as in [45]:

$$\eta_{se} = \log_2 \left( 1 + \frac{1.5 \cdot \text{SINR}}{-\ln(5 \cdot \text{BLER})} \right) \quad (6)$$

**Table 4**  
Configuration of the simulation environment.

Parameter	Symbol	Value
Simulation time		120 s
Sampling time	$T_s$	10 ms
Vehicle pairs	$N_p$	1000
Beam update period	$T_b$	{40, 80, 160} ms
Operating frequency	$f_0$	28 GHz
System bandwidth	$B$	50 MHz
MCS Table		Table 5.1.3.1-3 [30]
Target BLER		$10^{-5}$
Transmitted Power	$P_T$	20 dBm
Receiver Noise Factor	$NF$	13 dB
Array elements per panel	$N$	{2, 3, 4, 6, 8}
Beamset oversampling	$O$	2
Number of layers	$l$	1

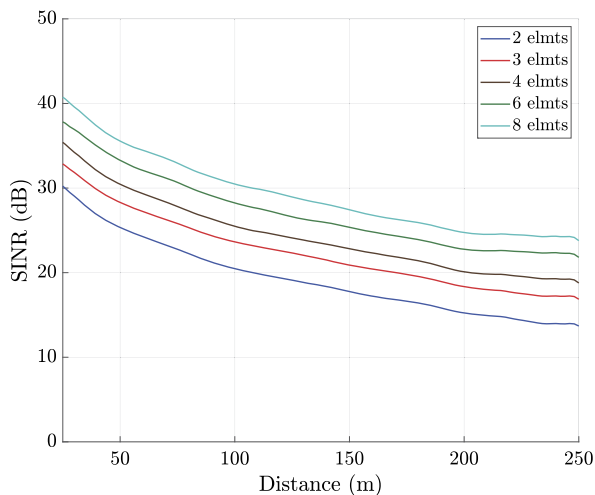


**Fig. 8.** Evolution of SINR as a function of distance for different number of array elements.

The experienced data rate is then adapted according to  $\eta_{se}$  so the link makes use of the maximum Modulation and Coding Scheme (MCS) level allowed by the channel. When no MCS is supported, the communication is interrupted and we call it as outage situation.

### 5.1. Average SINR

The first quality metric to validate is the SINR experienced by the receiver. For each V2V link and time sample, the received power and noise floor are calculated based on the values in Table 4. The beams are swept only with 40 ms period for now. The SINR calculated for all snapshots and trajectories is classified according to the distance between both vehicles and the mean value is calculated in for all samples within 2 m steps. The results are presented in Fig. 8 when 2 to 8 horizontal elements per panel are used. As expected, larger number of array elements imply an increased gain on both ends and hence more SINR in average. Doubling the number of elements provides up to 6 dB of improvement in total.

In the present work, the simultaneous use of equal or adjacent resources by several users in a crowded urban scenario is not considered. As previously stated, a 2 dB margin additional to the noise floor accounts for possible interference sources degrading the link quality at mmWaves. This might be particularly critical for distances below 100 m and small number of elements, for which the SINR at the receiver could be much lower than 20 dB and the performance of some advanced V2V use cases requiring large data rates (such as raw video and sensor data sharing or software up-

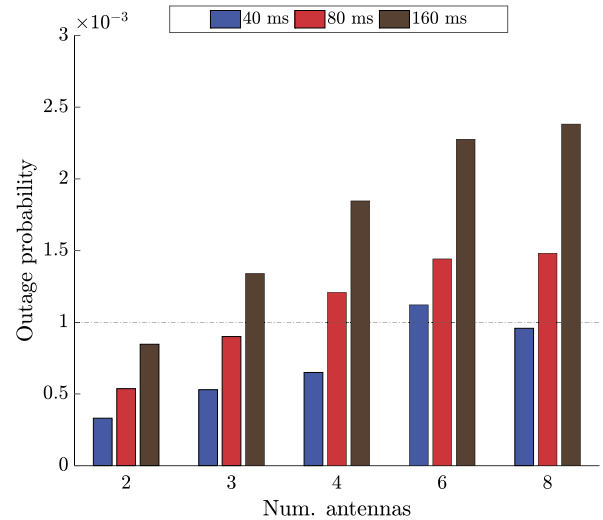


**Fig. 9.** Outage probability for different number of antennas per panel when the beam is updated every 40 (blue), 80 (red), and 160 ms (brown). The dashed line represents the 0.1% probability threshold.

dates [46]) could be compromised. It is worth mentioning that a 50 MHz channel bandwidth is used in the simulation. Increasing this value to 100 or even 200 MHz may help improving the achievable data rate at the expense of less available spectrum and higher noise power.

### 5.2. Outage probability

The previous results regarding SINR could lead to the wrong impression that an arbitrarily large array is always beneficial to improve the quality of communications. However, a large amount of antennas is a challenge in terms of cost, complexity, and overhead efficiency. Thus manufacturers must guarantee the required performance with the minimum number of elements possible.

One key parameter to validate that is reliability. It is a broad term encompassing any behavior of the channel that degrades the signal quality. Despite Packet Reception Rate (PRR) is often used as the figure of merit, its usage implies higher-layer simulations under realistic network conditions. For the assessment of physical-layer parameters such as the number of antenna elements, it is deemed sufficient to estimate the outage probability. In the present work, it is defined as the probability of not supporting any available MCS of those defined by the 3GPP in Table 5.1.3.1-3 from [30], so no communication is possible. For a particular use case, this definition could be extended to the capability of supporting a certain MCS or data rate. An outage situation is given mainly for two reasons: either the peak gain of the array is not sufficient to overcome the channel losses or there is a beam misalignment due to slow beam update sweeping a large set of narrow beams. Fig. 9 shows the outage probability for a number of antennas per panel in the horizontal plane between 2 and 8 when the beam is updated every 40, 80, and 160 ms. As a reference, a black dashed line illustrates the 0.1% probability. It is clear from the results that large number of elements (e.g., 6 and 8) lead to sharper beams that can be easily misaligned, especially when beams are slowly updated. This is in accordance with the expected beam coherence time [6,47]. However, [47] defines statistical models to derive the temporal variation of a vehicular Rayleigh-faded channel when directional antennas are used. The channel is calculated for the 60 GHz band with a one-ring scatterer model for the NLOS component. This differs from the current work, where all results are based on numerical evaluations of a realistic urban scenario at 28 GHz.

**Table 5**

Mean time in outage for different number of antennas per panel and beam update period (units: ms).

<i>N</i>		2	3	4	6	8
Beam update	40 ms	49.4	51.1	26.5	38.7	29.7
	80 ms	52.5	34.3	38.7	41.7	39.8
	160 ms	57.0	47.4	58.5	59.9	58.4

**Table 6**

Mean beam duration on each panel (units: s).

<i>N</i>		2	3	4	6	8
Panel	Front	3.75	3.59	3.33	2.96	2.71
	Back	5.39	5.21	4.95	4.76	4.3
	Right	0.62	0.90	0.75	0.74	0.61
	Left	0.65	0.58	0.51	0.47	0.58

The effect of wider beams is not that evident. Very wide beams are expected to cover a very broad range of angles so large update periods could be sufficient. However, they suffer from low gain so large distances with high path loss at mmWave frequencies or any fading-related effect may cause large power drops impossible to overcome with such geometries. This issue is particularly evident in Table 5. There, the mean duration of an outage period for the same previous cases is depicted. When outage is produced due to low gain values (2 or 3 antennas per panel), it is not sufficient to increase the update rate and outage periods even larger than the update period are easily given. On the other hand, outage due to beam misalignments (sharp beams with high number of antennas, from 4 to 8) can be mitigated with faster updates.

### 5.3. Beam usage

The last parameter of interest is the mean duration of each beam, i.e., the time it takes in average for the car to switch to another beam, which can also be related to the beam coherence time. In this case, the values are classified by the panel being used. In this way, it is possible to discern which panels are prone to faster beam updates according to the traffic behavior in an urban scenario like the one under study. Table 6 shows the mean duration of a beam for panels ranging from 2 to 8 horizontal elements and the four panels on the roof's edges (front, back, right, and left, defined according to the driving direction). All values are calculated for a beam update period of 40 ms. As expected, the beams lasting longer time are those on the front and the back sides of the car. When two vehicles are driving on the same road, in the same or opposite direction, they tend to use similar beams until they reach each other. On the contrary, when a vehicle is overtaking or it crosses the other's path, lateral panels need to switch faster the beams. This is critical in situation of high-speed lanes like highways. In this case, all cars drive at an average speed of 60 km/h and even one order of magnitude difference is stated.

The results in Table 6 suggest that non-uniform panels or adaptive beams could provide better performance to prevent from outage when steering angles are close to the orthogonal of the driving direction. Focusing capabilities can be enhanced at front and rear angles with a large number of radiating elements, whereas wider beams made with less elements (and, hence, less costly solutions) are deemed to perform good enough sidewise. Then, up to 8 horizontal elements can be used in front and back panels given the large benefit in SINR, the low outage probability expected from front-to-back communications, and the similar performance in terms of outage when compared to 6 elements. For the side panels, vehicles communicating at those angles are usually closer as well, so there is no need of very high gain patterns and 3 elements should be sufficient as a trade-off between directivity and reliability.

## 6. Conclusions

In the present work, the benefits of appropriate choice of smart antenna arrays for Cooperative Connected and Automated Mobility (CCAM) is presented. Highly-reliable delivery of large data in a timely manner requires of large bandwidth channels available in mmWave frequencies and synchronization between vehicles. Beamforming capabilities are essential for that purpose but strong challenges appear such as beam alignment, strong shadowing effects, and scattering on vehicles that could degrade the intended beam performance. To help overcoming those issues, an adequate assessment of the antenna system mounted on the vehicles is required.

A cost-effective antenna system for mmWave vehicular communications is presented with beam steering capabilities in azimuth and a shaped constant beam in elevation to reduce scattering on the vehicle bodywork and to cover the necessary angles for V2X communications. The integration suitability on the vehicular platform is also studied. A 4-panel sectorized geometry with arrays mounted on the roof's edges is shown as an adequate trade-off between radiation properties, cost and integration. Regarding each array, only 3 vertical elements with fixed analog weights are able to provide fair enough radiation in elevation, which is maximum between  $-15^\circ$  and  $30^\circ$  and gain decreases in the  $[30, 90]^\circ$  range proportional to  $\sec(90^\circ - \theta)$ .

On the horizontal plane, different solutions with a variable number of elements are studied. A predefined beamset covering all azimuth angles is used and its performance is validated through simulations on a realistic urban scenario where several V2V links are established. In light of the presented results, the proposed system obtains satisfactory all-around coverage to support a variety of connected vehicle applications foreseen in the autonomous landscape. The system aligns with 3GPP evaluation options for 5G-enabled vehicles, and the results show the possibilities of 5G codebooks applied to a mmWave antenna array operating in a V2V urban environment. The numerical simulation provides useful insights on the performance in terms of achievable SINR and outage probability for each case. A minimum number of 3 horizontal elements per panel properly satisfies both magnitudes. However, one could take advantage of the non-homogeneous distribution of traffic in azimuth to enhance the focusing capabilities to front and rear angles with an asymmetric geometry. There, up to 8 element could be mounted if the cost increase is still attainable.

### Declaration of competing interest

The authors declare that they have no known competing financial interests or personal relationships that could have appeared to influence the work reported in this paper.

### Acknowledgements

This work was partly funded by the Spanish Ministerio de Economía y Competitividad under the projects PID2019-107885GB-C31 and MDM2016-0600, the Catalan Research Group 2017 SGR 219, and "Industrial Doctorate" programme (2018-DI-084). The Spanish Ministry of Education contributes via a predoctoral grant to the first author (FPU17/05561).

### References

- [1] European Commission, Communication from the commission to the European Parliament, the council, the European economic and social committee, the committee of the regions - on the road to automated mobility: an EU strategy for mobility of the future (COM/2018/283 final), URL <https://eur-lex.europa.eu/legal-content/EN/TXT/?uri=CELEX:52018DC0283>, 2018.

- [2] K. Sjöberg, P. Andres, T. Buburuzan, A. Brakemeier, Cooperative intelligent transport systems in Europe: current deployment status and outlook, *IEEE Veh. Technol. Mag.* 12 (2) (2017) 89–97.
- [3] European Telecommunications Standards Institute (ETSI), ETSI TR 103 576-2. Pre-standardization study on ITS architecture; Part 2: Interoperability among heterogeneous ITS systems and backward compatibility, 2020.
- [4] 5G Automotive Association (5GAA); Working Group Standards and Spectrum, Study of spectrum needs for safety related intelligent transportation systems - day 1 and advanced use cases, 2020.
- [5] 3GPP, Technical Specification Group Services and System Aspects; Enhancement of 3GPP support for V2X scenarios; Stage 1 (Release 16), Technical Specification (TS) 22.186, 3rd Generation Partnership Project (3GPP), version 16.2.0, 06 2019.
- [6] A. Pfadler, C. Ballesteros, J. Romeu, L. Jofre, Hybrid massive MIMO for Urban V2I: sub-6 GHz vs mmWave performance assessment, *IEEE Trans. Veh. Technol.* 69 (5) (2020) 4652–4662.
- [7] F. Maschietti, D. Gesbert, P. de Kerret, H. Wymeersch, Robust location-aided beam alignment in millimeter wave massive MIMO, in: *GLOBECOM 2017-2017 IEEE Global Communications Conference*, IEEE, 2017, pp. 1–6.
- [8] S. Kaul, K. Ramachandran, P. Shankar, S. Oh, M. Gruteser, I. Seskar, T. Nadeem, Effect of antenna placement and diversity on vehicular network communications, in: *2007 4th Annual IEEE Communications Society Conference on Sensor, Mesh and Ad Hoc Communications and Networks*, IEEE, 2007, pp. 112–121.
- [9] E. Whalen, A. Elfrgani, C. Reddy, R. Rajan, Antenna placement optimization for vehicle-to-vehicle communications, in: *2018 IEEE International Symposium on Antennas and Propagation & UNSC/URSI National Radio Science Meeting*, IEEE, 2018, pp. 1673–1674.
- [10] N. Adhikari, S. Noghianian, Capacity measurement of multiple antenna systems for car to car communication, in: *2014 IEEE Antennas and Propagation Society International Symposium (APSURSI)*, IEEE, 2014, pp. 603–604.
- [11] 5GAA, Distributed Vehicular Antenna Systems, Technical Report (TR), 5G Automotive Association, version 1.0, 01 2022.
- [12] T. Abbas, J. Karedal, F. Tufvesson, Measurement-based analysis: the effect of complementary antennas and diversity on vehicle-to-vehicle communication, *IEEE Antennas Wirel. Propag. Lett.* 12 (2013) 309–312, <https://doi.org/10.1109/LAWP.2013.2250243>.
- [13] A. Thiel, O. Klemp, A. Paiera, L. Bernadó, J. Karedal, A. Kwoczek, In-situ vehicular antenna integration and design aspects for vehicle-to-vehicle communications, in: *Proceedings of the Fourth European Conference on Antennas and Propagation*, 2010, pp. 1–5.
- [14] J. Yang, J. Li, S. Zhou, Study of antenna position on vehicle by using a characteristic modes theory, *IEEE Antennas Wirel. Propag. Lett.* 17 (7) (2018) 1132–1135, <https://doi.org/10.1109/LAWP.2018.2829718>.
- [15] L. Huang, Y. Lu, A switchable or MIMO antenna for V2X communication, in: *2019 IEEE International Conference on Computational Electromagnetics (ICCEM)*, 2019, pp. 1–2.
- [16] K. Srivastava, A.K. Dwivedi, A. Sharma, Circularly polarized dielectric resonator-based multiple input multiple output antenna with pattern and polarization diversity for vehicular applications, *Int. J. Circuit Theory Appl.* 49 (10) (2021) 3421–3433.
- [17] A. Zandamela, K. Schraml, S. Chalermwisutkul, D. Heberling, A. Narbudowicz, Digital pattern synthesis with a compact MIMO antenna of half-wavelength diameter, *AEÜ, Int. J. Electron. Commun.* 135 (2021) 153728.
- [18] Z. Wang, S. Liu, Y. Dong, Compact wideband pattern reconfigurable antennas inspired by end-fire structure for 5G vehicular communication, *IEEE Trans. Veh. Technol.* (2022).
- [19] Third Generation Partnership Project (3GPP), R1-1805259. V2X NR Evaluation Methodology - Suggestion for the incorporation of realistic vehicle antenna patterns, 2018.
- [20] J.-J. Park, J. Lee, K.-W. Kim, K.-C. Lee, M.-D. Kim, Vehicle antenna position dependent path loss for millimeter-wave V2V communication, in: *2018 11th Global Symposium on Millimeter Waves (GSMM)*, IEEE, 2018, pp. 1–3.
- [21] M. Ko, H. Lee, J. Choi, Planar LTE/sub-6 GHz 5G MIMO antenna integrated with mmWave 5G beamforming phased array antennas for V2X applications, *IET Microw. Antennas Propag.* 14 (11) (2020) 1283–1295.
- [22] Y.-X. Sun, K.W. Leung, K. Lu, Compact dual microwave/millimeter-wave planar shared-aperture antenna for vehicle-to-vehicle/5G communications, *IEEE Trans. Veh. Technol.* 70 (5) (2021) 5071–5076.
- [23] A. Nasr, K. Sarabandi, M. Takla, Multi-beam dual-polarized windshield antenna with wide elevation coverage for 5G V2X applications, in: *2020 IEEE International Symposium on Antennas and Propagation and North American Radio Science Meeting*, 2020, pp. 1333–1334.
- [24] Third Generation Partnership Project (3GPP), TR 36.885 V14.0.0. Study on LTE-based V2X Services, 2016, (Release 14).
- [25] Third Generation Partnership Project (3GPP), TR 22.886 V16.2.0. Study on enhancement of 3GPP Support, for 5G V2X Services, 2018, (Release 16).
- [26] Y. Bandy, G.M. Rather, G.R. Begh, Effect of atmospheric absorption on millimetre wave frequencies for 5G cellular networks, *IET Commun.* 13 (3) (2018) 265–270.
- [27] S. Sun, T.S. Rappaport, R.W. Heath, A. Nix, S. Rangan, MIMO for millimeter-wave wireless communications: beamforming, spatial multiplexing, or both? *IEEE Commun. Mag.* 52 (12) (2014) 110–121.
- [28] M. Giordani, A. Zanella, T. Higuchi, O. Altintas, M. Zorzi, On the feasibility of integrating mmWave and IEEE 802.11p for V2V communications, in: *2018 IEEE 88th Vehicular Technology Conference (VTC-Fall)*, IEEE, 2018, pp. 1–7.
- [29] F. Henschke, Beamforming - how does it work, [Online]. Available: [https://www.emf.ethz.ch/fileadmin/redaktion/public/downloads/3\\_angebot/veranstaltungen/AA\\_Henschke.pdf](https://www.emf.ethz.ch/fileadmin/redaktion/public/downloads/3_angebot/veranstaltungen/AA_Henschke.pdf), Nov 2019. (Accessed 13 August 2021).
- [30] 3GPP, Technical Specification Group Radio Access Network, NR, Physical Layer Procedures for Data, (Release 16), Technical Specification (TS) 38.214, 3rd Generation Partnership Project (3GPP), version 16.3.0 (09 2020).
- [31] T.S. Rappaport, S. Sun, R. Mayzus, H. Zhao, Y. Azar, K. Wang, G.N. Wong, J.K. Schulz, M. Samimi, F. Gutierrez, Millimeter wave mobile communications for 5G cellular: it will work! *IEEE Access* 1 (2013) 335–349.
- [32] P.A. Lopez, M. Behrisch, L. Bieker-Walz, J. Erdmann, Y.-P. Flötteröd, R. Hilbrich, L. Lücken, J. Rummel, P. Wagner, E. Wießner, Microscopic traffic simulation using SUMO, in: *The 21st IEEE International Conference on Intelligent Transportation Systems*, IEEE, 2018, pp. 2575–2582, <https://elib.dlr.de/124092/>.
- [33] S. Jaekel, L. Raschkowski, K. Börner, L. Thiele, QuaDRiGa: a 3-d multi-cell channel model with time evolution for enabling virtual field trials, *IEEE Trans. Antennas Propag.* 62 (6) (2014) 3242–3256.
- [34] Third Generation Partnership Project (3GPP), TR 37.885 V15.3.0. Study on evaluation methodology of new Vehicle-to-Everything (V2X) use cases for LTE and NR, Release 15 (2019).
- [35] P.W. Fütter, L. Scialacqua, L.J. Foged, J. Soler, Combining measurement with simulation for automotive antenna placement and EMC analysis, in: *2018 IEEE 4th Global Electromagnetic Compatibility Conference (GEMCCON)*, 2018, pp. 1–4.
- [36] M. Rüttschlin, D. Tallini, Simulation for antenna design and placement in vehicles, in: *Antennas, Propagation RF Technology for Transport and Autonomous Platforms 2017*, 2017, pp. 1–5.
- [37] D. Kornek, M. Schack, E. Slotkne, O. Klemp, I. Rolfes, T. Kürner, Effects of antenna characteristics and placements on a vehicle-to-vehicle channel scenario, in: *2010 IEEE International Conference on Communications Workshops*, 2010, pp. 1–5.
- [38] K. Nono, M. Fujimoto, R. Yamaguchi, K. Tomimoto, A study on location of vehicle-mounted antennas for single-frequency full-duplex communication, in: *2021 International Symposium on Antennas and Propagation (ISAP)*, 2021, pp. 1–2.
- [39] Z. Wang, G. Wu, M.J. Barth, A review on cooperative adaptive cruise control (CACC) systems: architectures, controls, and applications, in: *2018 21st international conference on intelligent transportation systems (ITSC)*, in: *2018 21st International Conference on Intelligent Transportation Systems (ITSC)*, 2018, pp. 2884–2891.
- [40] A. Araghi, M. Khalily, P. Xiao, R. Tafazolli, Study on the location of mmWave antenna for the autonomous car's detection and ranging sensors, in: *2020 14th European Conference on Antennas and Propagation (EuCAP)*, 2020, pp. 1–4.
- [41] Á. Cardama, J. Romeu, J.M. Rius, L. Jofre, S. Blanch, M. Ferrando, *Antenas*, Univ. Politèc. de Catalunya, 2004.
- [42] L. Zhou, Y. Ohashi, Efficient codebook-based MIMO beamforming for millimeter-wave WLANs, in: *2012 IEEE 23rd International Symposium on Personal, Indoor and Mobile Radio Communications-(PIMRC)*, IEEE, 2012, pp. 1885–1889.
- [43] Y. Huang, C. Liu, Y. Song, X. Yu, DFT codebook-based hybrid precoding for multiuser mmWave massive MIMO systems, *EURASIP J. Adv. Signal Process.* 2020 (1) (2020) 1–13.
- [44] Third Generation Partnership Project (3GPP), R1-1612661, Advanced CSI Codebook Structure, 2018.
- [45] H. Seo, B.G. Lee, A proportional-fair power allocation scheme for fair and efficient multiuser OFDM systems, in: *IEEE Global Telecommunications Conference, GLOBECOM'04*, Vol. 6, 2004, IEEE, 2004, pp. 3737–3741.
- [46] 5GAA, Working Group Standards and Spectrum, Study of Spectrum Needs for Safety Related Intelligent Transportation Systems - Day 1 and Advanced Use Cases, version 1.0, Technical Report (TR) TR S 200137 5G Automotive Association, 06 2020.
- [47] V. Va, J. Choi, R.W. Heath, The impact of beamwidth on temporal channel variation in vehicular channels and its implications, *IEEE Trans. Veh. Technol.* 66 (6) (2017) 5014–5029.



# ASSESSMENT OF MMWAVE BEAMFORMING HANDSETS IN PRESENCE OF THE USER

---

This chapter is devoted to mobile pedestrian users. In particular, the impact of the human body on the radiation of mmWave handsets is studied with numerical and experimental campaigns. The resulting manuscript from this work is contained at the end of the chapter. First, some related references and insights on the methodology of the study, the simulation procedure, and the manufacturing of the human phantom are detailed.

## 6.1 Motivation and Related Work

There is a growing interest in studying the impact of the human body on the radiation of mobile terminals operating at frequency bands higher than conventional sub-6 GHz. It is particularly important when dealing with multi-element architectures and array geometries, which appear as the enabling technology for mmWave 5G communications. The effect of the phone antennas on the user body is also a matter of interest in this framework given the necessity of clarifying how the population will be exposed to this new types of radiation. New metrics and methodologies are required to study mmWave radiation when dealing with biological tissues.

During the last years, several numerical and experimental studies have been proposed. Wu, Rappaport and Collins lit the path in [104] with a discussion on current and new methods of evaluating the radiation with human bodies. They also compare different models of the skin dielectric properties and study its exposure under different conditions. The

## 6. ASSESSMENT OF MMWAVE BEAMFORMING HANDSETS IN PRESENCE OF THE USER

---

safety margins defined by the International Commission on Non-Ionizing Radiation Protection (ICNIRP) above 10 GHz imply power density ( $\text{W}/\text{m}^2$ ) measurements rather than typical specific absorption rate (SAR) ( $\text{W}/\text{kg}$ ). In particular, the limits are established according to this organization to  $10 \text{ W}/\text{m}^2$  for general public and  $50 \text{ W}/\text{m}^2$  for the occupational group. Further details about electromagnetic field (EMF) exposure at mmWave frequencies can be found in [104–106].

More recent works focused on the shadowing effect of the user and the impact in the coverage for mobile array structures [107–110]. Typical solutions include phased array antenna (PAA) architectures. The aforesaid publications detail the performance degradation in terms of spherical coverage and shadowed power. Most results are simulated and some experiments are carried out in presence of real users. Other studies tried to model the shadowing effect of the human body using a knife-edge approach based on real human measurements [111, 112]. The main drawback of such studies is the repeatability and the difficulty of modeling the dynamic movement as it is the main goal of this chapter. Additionally, those measurements are performed in indoor environments. In the literature, it is also possible to find models for near-field effects of fingers close to mobile antennas as in [113, 114]. The rest of the body is omitted and the impact of the finger in the antenna detuning is only noticeable for very short distances (less than two wavelengths from the antenna).

Human body phantoms are becoming a widely used tool in order to test real antennas in presence of biological tissues. In practice, the use of real bodies presents two main issues: as previously said, there is a lack of repeatability, as the person is not able to perfectly adopt the same pose for all measurements, and, secondly, some tests require the integration of certain parts inside the body, e.g., implants and embedded devices. In summary, the increasing research in the realistic replication of the dielectric properties of human tissue has allowed the use of body-like synthetic models. In that regard, Gustafson and Tufvesson introduced some simple phantoms in [115] to characterize reflection and shadowing effects of human bodies.

The study of the body dynamics when the user interacts with the mobile terminal is the last mile to fully model a realistic communication in a cellular environment. The introduction of beamforming capabilities to the mobile antennas relies on the proper shaping of the radiation pattern under any circumstance. In consequence, not only the shadowing due to the presence of a dielectric body must be studied but also the effect of the user movement, which surely will have critical implications in the distribution of the fields when beamforming techniques are applied.

Cotton already tried in [116] to understand the human body shadowing in movement for D2D communications. A statistical model is provided and then validated in a real outdoor urban environment, but the entire study is carried out for frequencies below 1 GHz. In a second manuscript [117], a similar analysis at 28 GHz can be found. It describes the angular dynamics of a beamforming device in presence of moving pedestrians. In this case, all human effects are present in the far-field region because there is no user holding the antennas, which remain static during the measurements.

## 6.2 Methodology

The work presented in this chapter pretends to provide some useful insights on how the interaction of the user, considering different postures, can modify the coverage of mobile handset arrays in the mmWave region for 5G communications. For that purpose, a set of numerical simulations are carried out and validated with two human-like phantoms for two distinct grip modes.

The use of mmWave frequencies in the next generation of cellular networks is expected to be devoted to short-range high-throughput communications, also called eMBB. This kind of requirements are expected to be needed in very demanding applications such as ultra high definition (UHD) multimedia streaming, augmented reality (AR) or cloud gaming. In these cases, the user is regularly holding the phone in front of his or her face with one or two hands. This can be called browsing mode, different from call mode in which the user holds the phone next to his or her ear. In the latter case, lower frequency and bandwidth requirements are needed to be fulfilled, so it is not a matter of interest to study its performance when dealing with mmWave bands. Figure 6.1 depicts the two user postures considered in the study.

### 6.2.1 Numerical Modeling

The numerical evaluation of the human bodies use as starting point the work related in [118] in which a human model for a simulated environment is proposed. The model is created using the MakeHuman software [119] and then the specific pose is applied in Blender [120]. The 3D object is then exported to the EM simulation software, CST Studio Suite [121] in this case. The prototype uses a male human with the MakeHuman default parameters and 170 cm height. A flow diagram of the modeling steps is depicted in Fig. 6.2.

The mobile terminal includes a perfect electric conductor (PEC) chassis of  $150 \text{ mm} \times 75 \text{ mm} \times 8 \text{ mm}$ . Different antenna configurations are to be tested but all of them include

## 6. ASSESSMENT OF MMWAVE BEAMFORMING HANDSETS IN PRESENCE OF THE USER

---

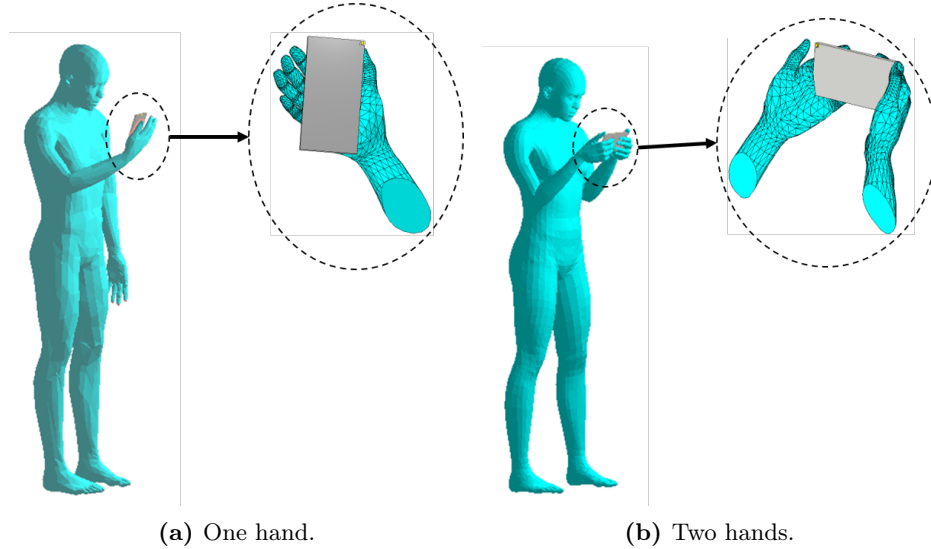


**Figure 6.1:** Models of the two grip modes.

as elementary radiator a dual-polarized patch antenna. The chosen substrate is 0.127 mm thick Rogers 5880 ( $\epsilon_r=2.2$ ) and metal layers are 17  $\mu\text{m}$  of copper. The antenna is matched at 26 GHz, corresponding to the central frequency of lowest European band of 5G FR2.

Given the large dimensions of the body, up to  $147\lambda \times 43\lambda \times 42\lambda$ , at 26 GHz, volume meshing starts to become unfeasible. Human skin dielectric properties extracted from [104] are  $\epsilon_r=16.55$  and  $\sigma=25.82\text{ S/m}$ , which make the body even electrically bigger for the simulator. In this case, the surface impedance equivalence is considered in order to obtain a surface mesh model. The human body is assumed as a metallic object with a dielectric coating whose properties correspond to the skin material. The penetration depth ( $\delta_p$ ) at this frequency is considered to be 1 mm [122, 123] and the surface impedance is calculated as follows:

$$Z = \sqrt{\frac{i\omega\mu_0}{\sigma + i\omega\epsilon_r\epsilon_0}}, \quad (6.1)$$

where  $\mu_0 = 4\pi \times 10^{-7}\text{ H/m}$ ,  $\epsilon_0 = 8.854 \times 10^{-12}\text{ F/m}$  and  $\omega = 2\pi f$  is the angular frequency. Using the dielectric properties previously described, the skin surface impedance turns to be  $Z_{skin}=69.98 + j30.55$  at 26 GHz.

The modeling of the radiating source, i.e., the phone, is performed in a previous step in which the user hands are also included. They are located in the near field region of the phone, so it is a good practice to simulate them together with the actually radiating structure. In this case, volume meshing is used in a time domain (TD) simulation. An

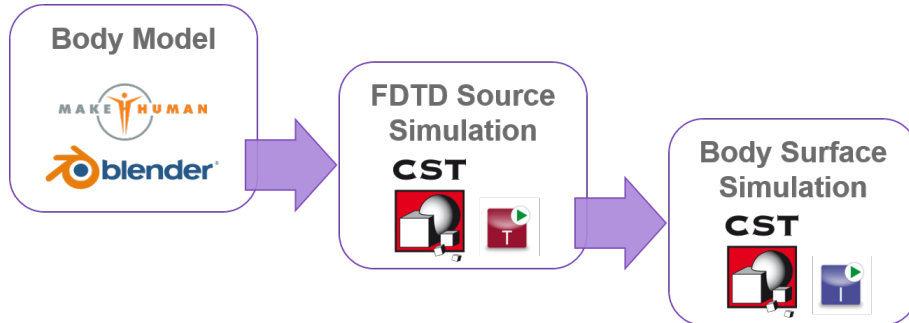


**Figure 6.2:** Human body modeling and simulation steps.

equivalent field source is obtained for the near field boundaries and imported as radiating source in the full human body model.

The numerical study of human body dynamics implies a large amount of complex and time consuming simulations. In consequence, it is needed an initial validation of the models under different assumptions and simplifications. It is essential to make an efficient use of the calculation time to perform a thorough analysis of the body poses and their impact in multi-antenna mobile systems.

The evaluation of the different models is based in the far-field radiation properties of the phone antennas in presence of the human body. Each model is compared with a reference case in which the full body is simulated for every position under study. The figure of merit is the mean average error (MAE) of the far-field gain 3D pattern, calculated as:

$$MAE = \frac{1}{N} \sum_{n=1}^N |x_n - \tilde{x}_n| \quad (6.2)$$

where  $x_n$  is the n-th gain sample using the original full body model,  $\tilde{x}_n$  is the sample of the simplified model under study, both in linear scale, and N is the total amount of points in the 3D space.

Given the radiation of patch antennas like the ones mounted on the phone structure, most part of the fields are concentrated on the body when facing towards the user. Nevertheless, it seems reasonable to avoid some parts which are far from the broadside direction. In order to analyse the effect of those parts, it is decided to cut the body at different levels and compare the far-field radiation with respect to the full body model. In this case, a single hand grip is assumed and one dual-polarized patch is placed on the top right corner of the phone. Three models are analysed and compared to the reference case with the full body. Figure 6.3 shows the different cuts made in the human model to reduce the complexity of the simulation. First, the body is cut on the knees and only the upper parts is considered.

## 6. ASSESSMENT OF MMWAVE BEAMFORMING HANDSETS IN PRESENCE OF THE USER

---

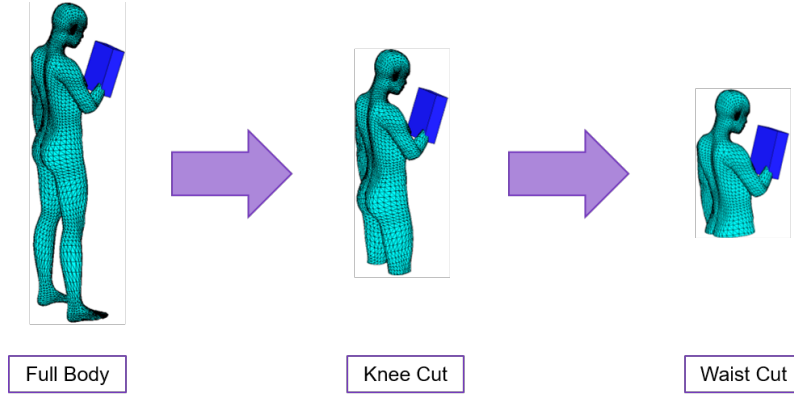


**Figure 6.3:** Different cuts in human body model.

In a second stage, only those parts over the waist are included in the simulation. These two cases, as well as the full body model, use the default CST mesh settings in which 5 cells per wavelength are used. Finally, a third case considers the body cut on the knees using a thicker mesh (4 cells per wavelength).

Given the results in Table 6.1, it is decided to cut the body model on its knees and reduce the mesh size to 4 cells per wavelength. From this point forward, all results are computed with this assumption.

**Table 6.1:** Metrics of the body simulations for different cut levels.

	Full body	Knee cut	Waist cut	Knee cut (thick mesh)
<b>Mesh size</b>	1.12M surfaces	915k surfaces	688k surfaces	600k surfaces
<b>Mesher time</b>	9m 40s	6m 26s	4m 01s	6m 15s
<b>Solver time</b>	4h 14m	2h 28m	2h 12m	1h 49m
<b>RAM</b>	30.12 GB	30.03 GB	28.77 GB	22.74 GB
<b>MAE 3D Farfield Port 1</b>	N/A	0.20 dB	7.75 dB	0.30 dB
<b>MAE 3D Farfield Port 2</b>	N/A	0.17 dB	9.46 dB	0.29 dB

### 6.2.2 Experimental Validation

Once the numerical evaluation procedure is defined, the experimental campaign must be detailed. At this stage, the simulated results must be verified with enough realism. Based on the criteria described in Section 6.1, a phantom model with the shape similar to the simulated human user is used.

For that purpose, a material mimicking the EM properties of the skin is prepared. The authors in [124] propose a mixture based on distilled water and polyethylene at 60 GHz. In [125], the recipe is tuned and proven to work at lower bands like the one to be tested in this work. Table 6.2 details the exact amount of each component for 100 g of distilled water.

**Table 6.2:** Skin phantom composition per 100 g of water.

Material	Quantity (g)
Distilled water	100
Polyethylene	35
Agar	3.8
TX-151	3.5

In order to validate the dielectric properties, a small sample of the resulting material is tested. By means of an open-ended coaxial probe, the complex dielectric constant is measured using the reflection parameter [126]. Due to practical limitations, the sample is only measured up to 20 GHz. Several measurements are performed with the same sample, since the positioning of the probe strongly determines the measured results. The actual properties of the sample are approximated as the average of the entire set of measurements.

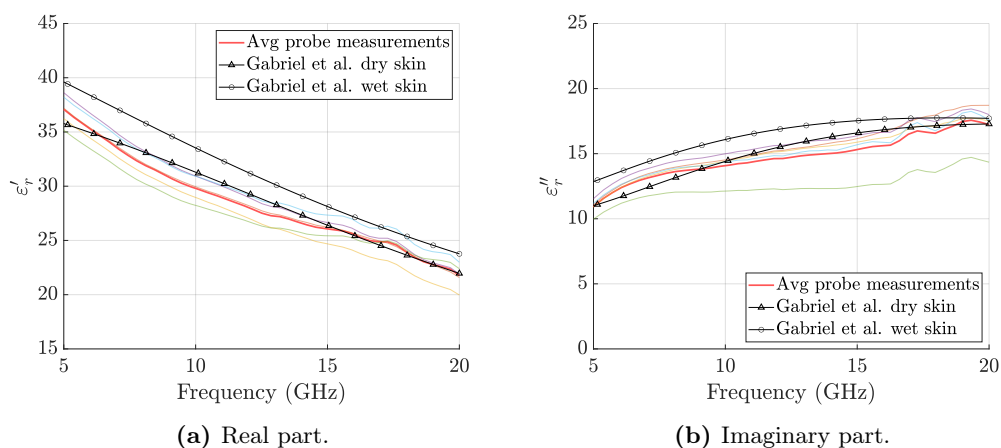


**Figure 6.4:** Measured complex permittivity of a phantom sample up to 20 GHz.

In Figure 6.4, the real and imaginary part of the permittivity measured with the probe are compared to those obtained from the Cole-Cole relaxation model [127] when Gabriel's wet and dry skin measurements [128] are used as input parameters. The sample presents

## 6. ASSESSMENT OF MMWAVE BEAMFORMING HANDSETS IN PRESENCE OF THE USER

---

good agreement when approaching the region of interest despite some small oscillations.

In any case, the precise value of the dielectric constant is not as relevant for the study as the effect of this change of the material properties with respect to the background produces on the propagation of waves (i.e., shadowing effect). Then, the reflection coefficient at the interface between a slab of phantom material and the air is calculated from the measured properties. This value is compared to those obtained from Gabriel's experiments [128] and good agreement is found as seen in Figure 6.5.

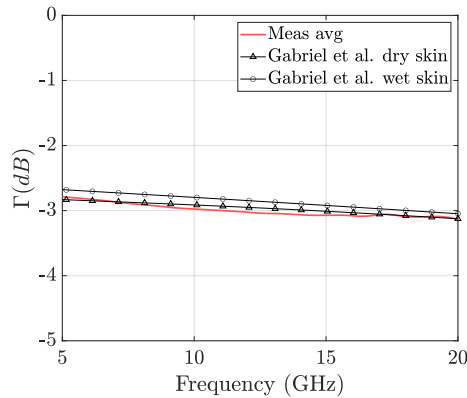


**Figure 6.5:** Reflection coefficient between air and the phantom material up to 20 GHz.

The authors in [124] used sodium azide for preservation purposes but it has been removed from the formula used in this work for safety reasons. Due to this fact, the phantom must be carefully preserved and handled, avoiding long-time exposures to contaminated air. In good conditions, the material can be kept up to 3 months with valid dielectric properties.

The skin material can be then applied to a human-like shape. In this case, as for the numerical simulations, only the torso is considered due to the lower impact of the legs in the radiation when the phone antennas face the user chest. As mentioned above, two models are used according to the two grip types for browsing: one and two hands. The first model uses the existing shape from the authors in [125], whereas a new model is built for the two-hand user. Figure 6.6 shows the manufactured phantom. A wooden pole in its core is used to get all the pieces together and hold the entire structure to the measurement rotor in the chamber. Each part of the torso and head is made of polystyrene foam and covered with 5 mm of skin material.

Finally, the prototype of the mmWave handset has to be prepared. As seen in the publication later introduced, different types of phone arrays are to be studied. They include a set of distributed patch antennas on the corners or edges of the chassis. To make





**Figure 6.6:** Two-hand phantom ready to mount in the anechoic chamber.

sure that most positions can be covered with the same design, it is proposed a hybrid model. It includes four dual-polarized patches, two on the top corners and two at the center of the long edges of the phone. During the design stage, only vias through the entire structure were allowed. The grounded coplanar waveguide (GCPW) feeding lines required some vias very close to the radiating element and a perforated version of the patch antenna is used (the *Gruyère* patch). Figure 6.7 shows the radiating element and printed circuit board (PCB) stackup of the prototype.

The finally manufactured model is presented in Figure 6.8. To provide enough thickness and robustness to the structure, the board containing the antennas is attached to a 1 mm FR-4 board and a 5 mm piece of polystyrene foam in between. To avoid the effect of surface waves, some conducting foil is used to cover the edges of the structure.

### 6.3 Publication

[J3] C. Ballesteros, L. Vähä-Savo, K. Haneda, C. Icheln, J. Romeu and L. Jofre, "Assessment of mmWave Handset Arrays in the Presence of the User Body," in *IEEE Antennas and Wireless Propagation Letters*, vol. 20, no. 9, pp. 1736-1740, Sept. 2021, doi: 10.1109/LAWP.2021.3095352.

## 6. ASSESSMENT OF MMWAVE BEAMFORMING HANDSETS IN PRESENCE OF THE USER

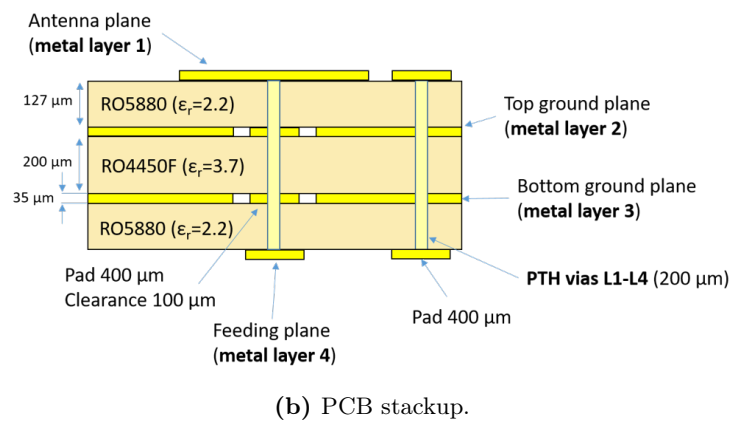
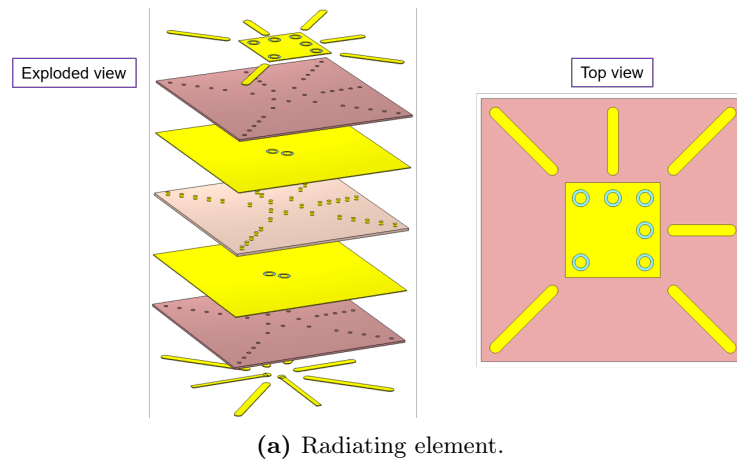


Figure 6.7: Design of the mmWave mobile handset.

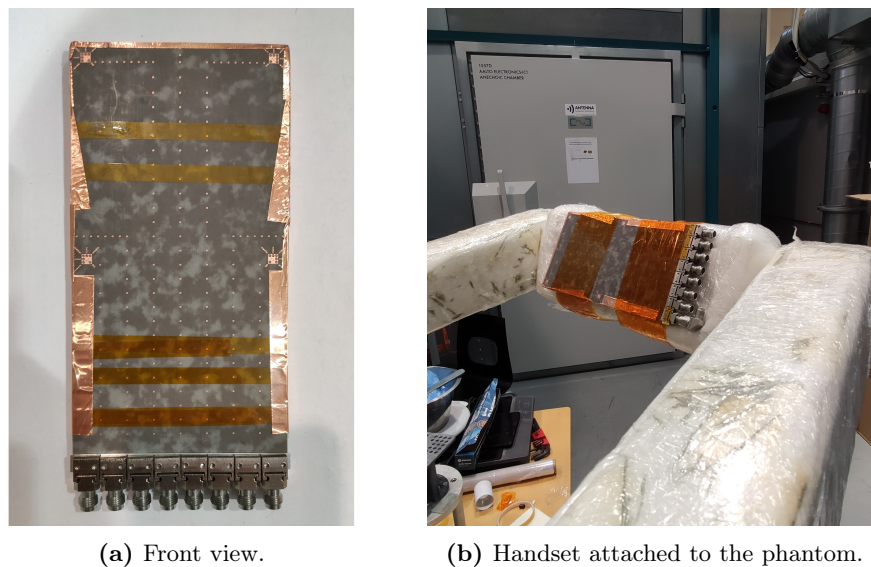








Figure 6.8: Manufactured prototype of the mmWave handset.

# Assessment of mmWave Handset Arrays in the Presence of the User Body

Christian Ballesteros , *Student Member, IEEE*, Lauri Vähä-Savo , Katsuyuki Haneda , *Member, IEEE*, Clemens Icheln , Jordi Romeu , *Fellow, IEEE*, and Lluís Jofre , *Fellow, IEEE*

**Abstract**—The emergence of mobile terminals operating at millimeter-wave frequencies necessitates the ability to evaluate the effect the environment, and in particular, users have on their radiation properties. Some studies evaluated the shadowing effects of a hand or an entire body for simple antenna configurations. This letter proposes a method for reliably predicting the performance of different array geometries in the presence of the users when they operate the mobile with one or with two hands. In practice, the way a mobile is operated is varying strongly between users, and hence, it is of great interest to draw a methodology to both numerically and experimentally evaluate any handset design in a large number of use cases in a repeatable manner. The use of numerical models and realistic phantoms allow high repeatability when evaluating the terminal radiation under real use conditions. Both the simulated body and the human phantom are used to study the field scattering from the handset arrays subject to the user interaction, yielding consistent results between them. Results suggest that shadowing by the user's torso usually decreases gain between 20–30 dB close to the region of the user. The user posture largely affects the spherical coverage, particularly for those antennas close to the corners in a two-hand mode.

**Index Terms**—5G handset, millimeter-wave (mmWave) arrays, user modeling.

## I. INTRODUCTION

THERE is a growing interest in studying the impact of the human body on the radiation of mobile terminals operating at frequency bands higher than the conventional sub-6 GHz. The body impact is particularly important when dealing with multiple-element antenna architectures and array geometries, which appear as the enabling technology for millimeter-wave (mmWave) 5G communications [1] to overcome issues such as greater losses of diffraction around blocking objects as the frequency increases.

Over the last years, several numerical and experimental studies have been proposed. Wu *et al.* [2] lit the path with methods

to evaluate the radiation in the presence of the human body and to evaluate the absorption of radiation. More recent works focused on the shadowing effect of the user and the coverage for phased antenna arrays on mobile phones [3]–[6]. These publications detail the performance degradation in terms of spherical coverage. They analyzed the radiation of one particular antenna array type and/or are limited to a single user position. Most results are from numerical simulations, while few experiments were carried out in the presence of real users holding the phone with one hand. At a channel (far-field) level, the shadowing effect of the human body compared to a simplified geometric model is evaluated in [7] with a comprehensive study on the blockage loss. The evolution of the received power from a handset when it is held with one hand by a real user is also measured in [8]. The main drawback of previous studies is the lack of repeatability or generalization of the conclusions to other grip positions or antenna arrays, i.e., usage conditions. The 3rd Generation Partnership Project (3GPP) introduced in Rel-14 a model to cope with those issues related to repeatability and general applicability by proposing a 30 dB gain drop due to self-blockage, i.e., signal shadowing due to the user on its own handset. Nevertheless, other effects such as the reflection from the torso toward the back side of the phone (back radiation) are excluded [9].

In [10], a realistic phantom of a one-hand human body is proposed for the study of mmWave 5G terminals, where only the one-hand browsing mode is considered. The present work benefits from that methodology to provide a comprehensive study in the 28 GHz (n257 NR) band for two operation modes and three different array geometries both numerical and experimentally. Given the large bandwidth available in 5G FR2, which is mainly devoted to high-data-rate delivery to a mobile phone [11], only data browsing operation mode is considered from now on, thus no voice calls (phone close to the user's head) are assumed.

The main contributions of this work related to the aforesaid issues are, therefore, summarized as follows.

- 1) Extend the proposed antenna evaluation methodology in [10] to more handset use cases and to different antenna arrays. Therefore, it is possible to find the most robust solution for relevant user postures according to the location and interelement distance of the antennas.
- 2) Use of realistic human models in simulation and phantoms in measurements to provide a large degree of repeatability as in [10]. The impact of the user and antenna geometry is also compared to state-of-the-art findings.

Manuscript received June 10, 2021; accepted July 2, 2021. Date of publication July 7, 2021; date of current version September 3, 2021. This work was supported in part by the Spanish Ministry of Economy under Projects MDM2016-0600 and 2019-107885GB-C31. The work of Christian Ballesteros was supported by the Ministry of Education under pre-doctoral under Grant FPU17/05561. (Corresponding author: Christian Ballesteros.)

Christian Ballesteros, Jordi Romeu, and Lluís Jofre are with the Antenna Laboratory, Polytechnic University of Catalonia, 08034 Barcelona, Spain (e-mail: christian.ballesteros@upc.edu; romeu@tsc.upc.edu; luis.jofre@upc.edu).

Lauri Vähä-Savo, Katsuyuki Haneda, and Clemens Icheln are with the Department of Radio Science and Engineering, Aalto University, 02150 Espoo, Finland (e-mail: lauri.vaha-savo@aalto.fi; katsuyuki.haneda@aalto.fi; clemens.icheln@aalto.fi).

Digital Object Identifier 10.1109/LAWP.2021.3095352

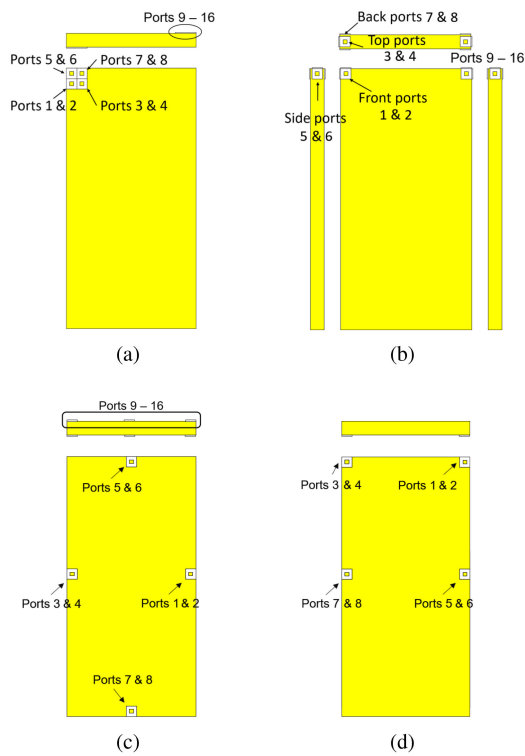


Fig. 1. UE handset array geometries. Arrays (a), (b) are used both in the simulated and experimental study, whereas (c) is only used in simulations (see Section III) and (d), in the experimental campaign (see Section IV). Ports 9–16 are pairwise equivalent to 1–8 on the second module.

- 3) All situations are evaluated in terms of the figures of merit defined by the 3GPP standard [12] to be comparable to the industry requirements.

## II. FRAMEWORK OF THE STUDY

In this section, the framework to study the interaction between the user and the mobile handset is described.

### A. Handset Mmwave Array Configurations

The antennas must be placed so that the radio link maintains its robust performance under the presence of a mobile user that affects antennas' radiation properties. Three antenna array configurations are considered, all composed of eight dual-polarized patch elements, as shown in Fig. 1(a)–(c). The first configuration is called colocated array (CA), already introduced in [10], consisting of two  $2 \times 2$  patch arrays, one on the front and one on the back side, at the top corners of the phone. The second array is called as distributed array (DA), where four antenna elements are arranged around each top corners of the phone as a three-dimensional (3-D) array geometry. The edge array (EA) encompasses patch elements placed at the center of each edge of the phone, four per side. A metal cuboid, assumed as a perfect electric conductor, with the dimensions  $150 \times 75 \times 8$  mm models the phone chassis.

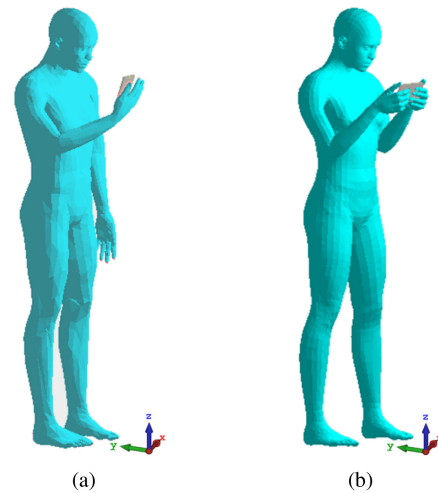


Fig. 2. Human postures modeling a realistic handset usage. (a) One-hand mode. (b) Two-hand mode.

### B. User Body Modeling

The methodology used to numerically model the human body of a user is detailed in [13]. The scattering of the body is computed by means of the surface integral method. As a source, the near-field radiated fields of the handset array in the presence of the hands are used, which are computed by means of finite-difference time-domain (FDTD) and a complete 3-D mesh of the hands. The skin properties defined by [2] are sufficient to model the scattering of the human body,  $\epsilon_r = 16.55$  and  $\sigma = 25.82$  S/m, since the penetration depth at 28 GHz is only about 1 mm [14], [15].

The user holds the phone with one or two hands, in front of his or her face, in browsing (multimedia) mode. Thus, two operation modes are assumed, with one- or two-hand grip (see Fig. 2). The phone is tilted  $20^\circ$  away from the zenith direction in both cases.

### C. Performance Evaluation

Beam scanning is for the three arrays performed with one 3 bit phase shifter per port in computer simulations, and in each direction, the maximum gain of the available 1024 beams is determined to analyze spherical coverage statistics.

Spherical coverage is usually analyzed by means of the cumulative distribution function (CDF) of the effective isotropic radiated power (EIRP) (in the transmission mode) or the effective isotropic sensitivity (EIS) (in reception) across different pointing angles. The 3GPP specifies the over-the-air (OTA) radio characteristics that the user equipment (UE) must satisfy in the free space [12]. It is found relevant to investigate the degradation in those figures when the user is present. The requirements for power class 3, corresponding to mobile handsets, are detailed in Table I. The impact is equivalent in downlink or uplink, and hence, we analyze only the EIRP of the handset.

## III. NUMERICAL RESULTS

The three handset array configurations are studied in two operation modes, i.e., one- and two-hand grip in terms of their

TABLE I  
TRANSMITTER AND RECEIVER SPECIFICATIONS FOR POWER CLASS-3 UE IN  
THE N257 NR BAND

Min peak EIRP	Max EIRP	Min EIRP at 50%-tile CDF
22.4 dBm	43 dBm	11.5 dBm
<b>REFSENS<sup>1</sup></b>	<b>EIS at 50%-tile CCDF</b>	
-88.3 dBm	-77.4 dBm	

<sup>1</sup> Values for 50 MHz bandwidth, 3 dB must be successively added for 100/200/400 MHz.

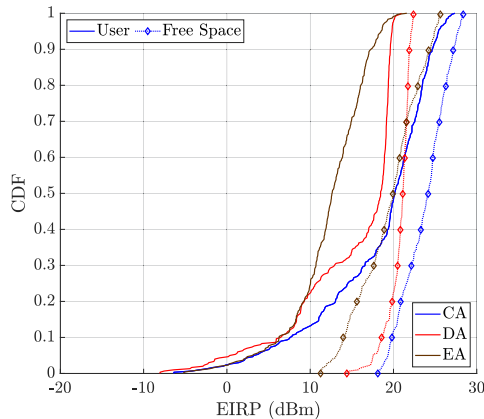


Fig. 3. Comparison of the EIRP CDF for the three arrays in one-hand mode.

TABLE II  
VARIATION OF THE EIRP DUE TO A HUMAN BODY FOR THE THREE ARRAY  
GEOMETRIES UNDER ONE-HAND OPERATION

	CA	DA	EA
$\Delta$ peak EIRP (dB)	-1.0	-1.4	-4.1
$\Delta$ 50%-tile EIRP (dB)	-4.0	-2.7	-7.3

EIRP. The transmit power is set to 10 dBm so the minimum peak EIRP of the three arrays in free space conditions fulfills the requirements from the 3GPP standard (see Table I).

#### A. One-Hand Operation

The user's palm mainly affects the antennas mounted on the back side of a mobile phone case in one-hand data mode. Also the effect of the torso is significant, mainly on the front far-field radiation. Fig. 3 shows the CDF of the EIRP for the one-hand operation mode compared to the free-space case. The signal from the dual-polarized antennas is coherently combined. For all three array configurations, there is a clear degradation on the realized EIRP.

This degradation is summarized in Table II with the variation of the peak and median EIRP with respect to the free space. Negative values mean a degradation of the EIRP with the human body and positive values imply an improvement compared to the free-space radiation. The most affected geometry is the EA, in which back antennas are partially covered by the hand palm. The top corner arrays like CA and DA are able to radiate across the head and the self-blockage effect is somehow mitigated.

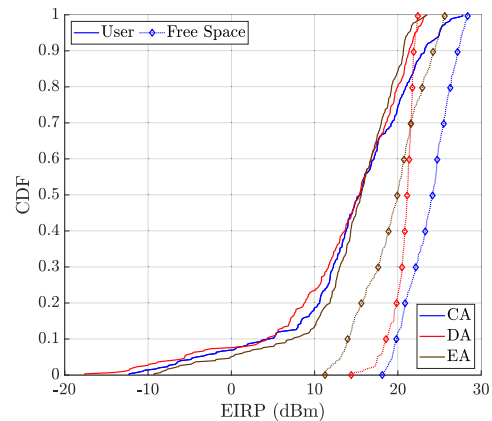


Fig. 4. Comparison of the EIRP CDF for the three arrays in the two-hand mode.

TABLE III  
VARIATION OF THE EIRP DUE TO A HUMAN BODY FOR THE THREE ARRAY  
GEOMETRIES UNDER TWO-HAND OPERATION

	CA	DA	EA
$\Delta$ peak EIRP (dB)	-0.6	1.1	-2.2
$\Delta$ 50%-tile EIRP (dB)	-8.7	-5.8	-4.4

#### B. Two-Hand Operation

The same analysis is carried out for the two-hand mode. The phone structure is now rotated by 90° in a plane parallel to the screen. The palm covers the antennas on the short edges and corners, which is even translated in a slight detuning of the resonant frequency, also considered in the simulation. Fig. 4 represents the CDF of the EIRP in a two-hand mode for the three aforementioned array configurations. The results show a noticeable loss with respect to free-space radiation and the tendency is similar for all arrays. Only the CA has a clear higher peak gain when the phone is held with two hands.

Table III details the loss in the spherical coverage for each case. The overall coverage is degraded due to the fact that both hands cover the phone and all antennas are right in front of the torso. Nevertheless, the peak gain is not that much affected compared to the one-hand operation. This is mainly due to the back radiation that reinforces those angles opposite to the user. Despite the larger degradation of the CA coverage, this geometry still appears to be the one reaching larger gain values both for one- and two-hand operation modes. However, in a two-hand mode, the gain up to the 70%-tile for all geometries is practically the same.

## IV. EXPERIMENTAL VALIDATION

The performance of the handset antennas in the presence of the user is now assessed through measurements in order to validate the numerical approach. Two human phantoms are built as in Fig. 5 to mimic the scattering effect of the human body when the user holds the mobile with one hand or with two hands, similarly to the two posture models in Fig. 2. The human phantom with one hand is used to measure the CA and DA configurations,

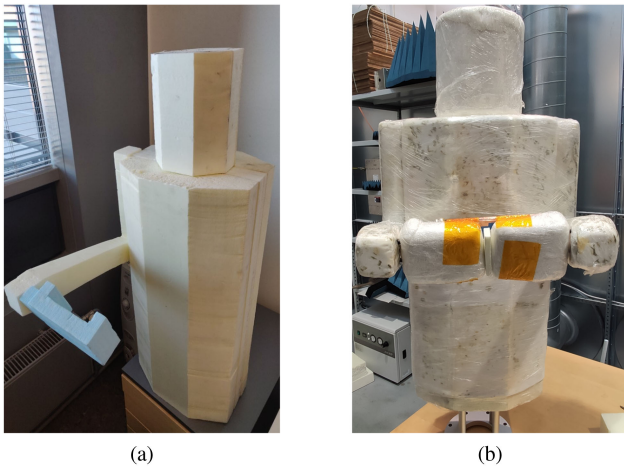


Fig. 5. Human phantoms representing a mobile user. (a) One-hand phantom polystyrene body foundation before coating with skin material. (b) Two-hand phantom once covered with skin material.

TABLE IV

DIFFERENCE OF THE HANDSETS' EIRP BETWEEN MEASUREMENTS AND SIMULATIONS OF USER'S POSTURES REPRESENTED IN FIG. 5 AND FIG. 2, RESPECTIVELY

	One hand		Two hands
	CA	DA	Mixed Array
$\Delta$ peak EIRP (dB)	-0.1	4.9	-0.6
$\Delta$ 50%-tile EIRP (dB)	-0.1	-1.3	1.3

where all the antennas are on the top corners of the phone. A prototype of mixed array [in Fig. 1(d)] with both edge and corner antennas is used with the two-hand phantom. The two types of antenna configurations are compared to provide further understanding of the actual effect of the hands close to the short edges. The EA design is not considered in this section. These results extend the methodology in [10] to two grip modes and three different handset arrays. The phantom does not include the effect of the lower legs, and polar angles greater than  $150^\circ$  are removed because of the shadowing of the mast holding the phantom in the chamber. The measurements are performed with  $1^\circ$  and  $10^\circ$  resolution in polar and azimuth angles, respectively.

The far-field radiation of the measured arrays with the two phantom models is compared to the numerical results in terms of the EIRP CDF. Table IV depicts the difference between the measured and simulated EIRP and the three aforementioned geometries. The results agree with small variance. The largest difference is for the DA, in which assembly inaccuracies and surface currents on the metal cuboid representing the phone chassis affect the actual performance of the prototype.

For illustration, Fig. 6 shows the EIRP difference between free-space radiation and the coverage in the presence of the human phantom for the mixed array geometry in a two-hand mode. As expected, the user shadows the region in front of the phone, whereas some back radiation is reinforced, reaching higher values than those in free space (particularly high for the CA and mixed arrays).

The spherical coverage is then compared to the simplified model of the 3GPP [9], which specifies the additional loss to

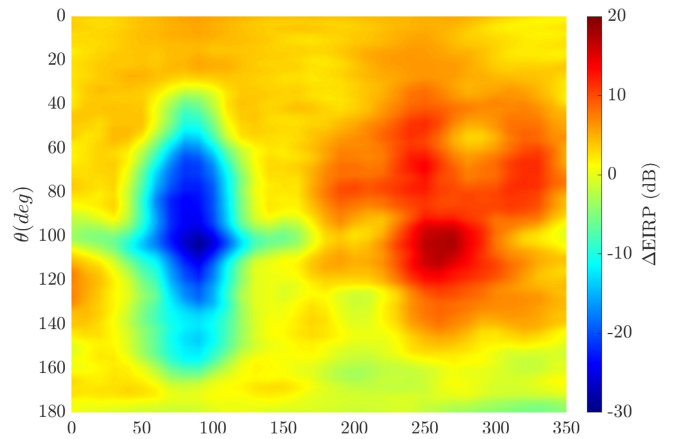


Fig. 6. Difference of EIRP between measured free-space and two-hand human phantom for the mixed array.

TABLE V

STATISTICS OF THE MEASURED HUMAN BODY SHADOWING (LOSS IN EIRP) COMPARED TO FREE-SPACE RADIATION

	One hand		Two hands	3GPP TR 38.901	
	CA	DA	MA	Portrait	Landscape
Min $\Delta$ EIRP (dB)	-29.1	-28.3	-28.2	-30	-30
$x_{sb}$ ( $^\circ$ )	40	60	50	120	160
$y_{sb}$ ( $^\circ$ )	99	97	57	80	75

As a reference, the parameters of the blockage model from the 3GPP are shown [9].

those propagation paths within the self-blocking region. These results are also in line with those found in the literature as in [3] and [13]. The effect of the body shadowing is then summarized in Table V in terms of the shadowing depth and its extent along the azimuth ( $x_{sb}$ ) and elevation ( $y_{sb}$ ) dimensions. The maximum additional loss agrees with the models of the 3GPP, while the 0-dB gain to other directions than the self-blocking region would not be true because of the existence of the back-radiation. In addition, the azimuth and elevation spans do not completely agree. In the experimental results, those are calculated by assuming self-blockage when losses are greater than 20 dB within the shadowed region as previously stated.

## V. CONCLUSION

This letter proposes a method to assess the performance of mmWave handset-antenna designs in the presence of a human user. The shadowing and scattering properties of the body are compared for two operation modes, holding the handset with one or with two hands. The study presents the achievable coverage of representative array geometries. A good agreement in the antenna radiation characteristics is found in terms of the CDF of the EIRP under the presence of a human body, both simulated and measured with a phantom.

It demonstrated a high dependence between the array geometry, the operation mode, and the self-blockage shadowing effect. The effect of the human phantom is compared to those blockage models defined by the 3GPP with small discrepancies. None of the arrays is found most robust for both one- and two-hand scenarios in terms of coverage. More dual-polarized antennas could be beneficial in this sense.

## REFERENCES

- [1] W. Hong, K. Baek, Y. Lee, Y. Kim, and S. Ko, "Study and prototyping of practically large-scale mmWave antenna systems for 5G cellular devices," *IEEE Commun. Mag.*, vol. 52, no. 9, pp. 63–69, Sep. 2014.
- [2] T. Wu, T. S. Rappaport, and C. M. Collins, "The human body and millimeter-wave wireless communication systems: Interactions and implications," in *Proc. IEEE Int. Conf. Commun.*, Jun. 2015, pp. 2423–2429.
- [3] K. Zhao, J. Helander, D. Sjöberg, S. He, T. Bolin, and Z. Ying, "User body effect on phased array in user equipment for the 5G mmWave communication system," *IEEE Antennas Wireless Propag. Lett.*, vol. 16, pp. 864–867, 2017.
- [4] I. Syrytsin, S. Zhang, and G. F. Pedersen, "User impact on phased and switch diversity arrays in 5G mobile terminals," *IEEE Access*, vol. 6, pp. 1616–1623, 2018.
- [5] R. Rodríguez-Cano, S. Zhang, K. Zhao, and G. F. Pedersen, "User body interaction of 5G switchable antenna system for mobile terminals at 28 GHz," in *Proc. 13th Eur. Conf. Antennas Propag.*, Mar. 2019, pp. 1–4.
- [6] S. Zhang, X. Chen, I. Syrytsin, and G. F. Pedersen, "A planar switchable 3-D-Coverage phased array antenna and its user effects for 28-GHz mobile terminal applications," *IEEE Trans. Antennas Propag.*, vol. 65, no. 12, pp. 6413–6421, Dec. 2017.
- [7] U. T. Virk and K. Haneda, "Modeling human blockage at 5G millimeter-wave frequencies," *IEEE Trans. Antennas Propag.*, vol. 68, no. 3, pp. 2256–2266, Mar. 2020.
- [8] J. Hejlselbæk, J. Ø. Nielsen, W. Fan, and G. F. Pedersen, "Measured 21.5GHz indoor channels with user-held handset antenna array," *IEEE Trans. Antennas Propag.*, vol. 65, no. 12, pp. 6574–6583, Dec. 2017.
- [9] 3GPP, "Study on channel model for frequencies from 0.5 to 100 GHz (release 16)," ETSI TR 38.901 (V16.1.0), Dec. 2019.
- [10] L. Vähä-Savo *et al.*, "Empirical evaluation of a 28 GHz antenna array on a 5G mobile phone using a body phantom," *IEEE Trans. Antennas Propag.*, to be published, doi: [10.1109/TAP.2021.3076535](https://doi.org/10.1109/TAP.2021.3076535).
- [11] A. Narayanan *et al.*, "A first look at commercial 5G performance on smartphones," in *Proc. Web Conf.*, 2020, pp. 894–905.
- [12] 3GPP, "User equipment (UE) radio transmission and reception, Part 2: Range 2 Standalone (Release 16)," TS 38.101-2 (V16.7.0), Apr. 2021.
- [13] M. Heino, C. Icheln, and K. Haneda, "Self-user shadowing effects of millimeter-wave mobile phone antennas in a browsing mode," in *Proc. 13th Eur. Conf. Antennas Propag.*, Mar. 2019, pp. 1–5.
- [14] O. P. Gandhi and A. Riazi, "Absorption of millimeter waves by human beings and its biological implications," *IEEE Trans. Microw. Theory Techn.*, vol. 34, no. 2, pp. 228–235, Feb. 1986.
- [15] P. A. Hasgall *et al.*, "IT'IS Database for thermal and electromagnetic parameters of biological tissues," IT'IS Foundation, version 4.0, May 2018. [Online]. Available: <https://www.itis.ethz.ch/virtual-population/tissue-properties/overview/>

# CONCLUSION

---

The last chapter of this thesis is devoted to discuss the main outcomes of the work previously detailed, as well as future lines of research to further develop those concepts and introduce them in later releases of mobile communications.

## 7.1 Summary

By the time this thesis began, 5G and mmWaves started to appear on the horizon of future mobile communications. The fast development of technology and the frenetic pace of research on that regard forced me to shape this work and progressively steer its scope as it was developed. However, the foundational principles that served as the basis to further elaborate the project remain valid.

The trend in wireless communications towards higher frequency bands entails several challenges to overcome. In particular, two main cases with unsolved issues prior to their real implementation were identified: V2X and beamforming handsets. The former is associated to high mobility scenarios where the channel response varies rapidly and the solutions provided by current standards should be tailored to the actual challenges of such use cases. Beam determination and user tracking represent a major concern in the telecommunications industry for a successful delivery of large data packets in crowded environments, where medium- and short-range mmWave links are expected to thrive. Secondly, the impact of the users on mobile handsets, also considering their dynamics and mobility patterns, is paramount to successfully implement adequate beamforming techniques with DASs.

The evaluation of such situations, under the umbrella of 5G networks, needs a robust simulation environment. For that purpose, a system-level simulator is created to emulate multiple simultaneous links between mobile users (and fixed stations), i.e., the SLoBMo.



It makes use, in its ultimate version, of Matlab objects representing the different entities that participate in the system (antenna arrays, mobile users, the wireless channel...) and QuaDRiGa to extract the channel impulse response for each link. The latter is a GB-SCM tool that integrates the potential of well-known stochastic models and the physical propagation of waves of ray tracing. This goes in line with the first of our hypotheses in section 1.3.1. The validation of urban or highway scenarios with extremely random user trajectories and links goes against deterministic approaches, but purely stochastic tools sometimes lack of physical meaning at their outcome.

Both vehicular platforms and mobile handsets represent a major challenge due to the interaction of external entities (a vehicle, a human user or the environment) with the antenna systems proposed by engineers. An appropriate usage of the information concerning those entities represent the success or failure of beamforming and, hence, mmWave bands in 5G networks and beyond. For that reason, this thesis proposes the study of multi-element DAS together with the related environment in three challenging situations:

- V2I highway links, where a cellular station must optimize the use of spatial resources according to the vehicle speed and position information,
- the design of an optimum distributed multi-panel system for vehicles to provide good coverage for any V2X link, considering both elevation and azimuth radiation as well as the interaction with other vehicles and an urban environment,
- and the assessment of multi-antenna geometries at different locations of a mobile handset to minimize the impact of the human user according to typical usage patterns.

In [J1], the first case is addressed. First, a certain knowledge of the vehicular user is assumed, since positioning and speed information is expected to be available in future connected vehicles. By knowing the precision of that information, the optimum beam size of a cellular station is obtained thanks to the analytical expression derived in the manuscript. This expression includes the estimation of the SINR under Doppler effects for high-speed scenarios such as highways and positioning errors. The results demonstrate that not only the signal quality is enhanced but the probability of outage is reduced when compared to current beam sweeping strategies with same periodicity of the beam update. As in our initial guess in section 1.3.1, side-band information enables an accurate prediction of beams to outperform conventional beam sweeping strategies. However, its feasibility is

## 7. CONCLUSION

---

still under discussion due to the dependence of data which is external to the communication link itself.

When considering the vehicle side, the number of antennas is also growing with the emergence of advanced V2X use cases. The work in [J2] describes the methodology to design a tailored beam according to the new needs of vehicular communications. The coverage in elevation is ensured with a minimum impact of the scattering on the bodywork, which benefits the use of beam sweeping strategies. In azimuth, full coverage is achieved with up to four panels distributed on the roof edges. Our initial hypotheses about the distribution of the antenna panels was partially true. Locating the antennas on the edges reduces the impact of the bodywork, but it is not negligible yet. Besides, the amount of antennas per panel cannot be arbitrarily large, since the performance in terms of achievable data rate and outage probability is not always improving. Three radiating elements in elevation and four in azimuth (per panel) ensures an adequate performance when the system is mounted on realistic vehicles interacting with each other in an urban scenario. Despite not proved, the reduced impact of the bodywork and the full azimuthal coverage also make this DAS proposal suitable for V2N situations like the one described above and it is in line with current developments within the industry and standardization bodies [129]. The unequal distribution of links on the azimuth plane also allows some flexibility in the design and location of the panels. Beams pointing towards the vehicle sides take much less time to be uncorrelated and faster updates should be needed. Then, wider beams (obtained from less horizontal elements per array) can be used to ensure the tracking in those less probable and rapidly changing situations.

Finally, the case of a pedestrian user is also studied in [J3]. In particular, the different grip modes (with one or two hands) are considered to assess the impact of the body under realistic operation conditions for different distributed multi-antenna geometries. For that purpose, two numerical and phantom models of a standard user are created and validated through simulations and measurements. High dependency between the array geometry and the achievable coverage is proven. The loss in the achievable effective isotropic radiated power (EIRP) of antennas distributed on the mobile corners is smaller in average for the given postures when compared to co-located arrays or antennas located on the edges. The attenuation of the user torso is specially critical when focusing towards the normal direction from the screen of the phone, reaching self-shadowing values greater than 20 dB and covering between 40 and 60 degrees in azimuth (less than the simplified models from the 3GPP in [93]). This information can be critical when proposing new alternative geometries given the actual influence of the user and designers can target to a reduced impact on

radiation, despite the final performance is somehow unpredictable and tightly dependent on the particular user characteristics.

## 7.2 Open Research and Future Work

The world of mobile technologies and wireless systems is a source of endless challenges and, thanks to the growth of research centers and related industries, the limits of knowledge are constantly pushed forward. This thesis was born when 5G was far from being a reality and, by its end, many new and exciting issues appear.

The solutions proposed in the previous chapters to deal with mmWave multi-antenna systems, despite standard-compliant, are probably meant to be implemented in evolved versions of the current generation, especially the beam adaptation of cellular stations that require frequent update of the vehicle dynamics. Car manufacturers are also reluctant to the inclusion of complex antenna systems into their vehicles, mainly for cost and aesthetic reasons. However, it is expected an escalation of advanced automotive use cases demanding larger bandwidth and, hence, higher frequency bands. From that point forward, the proposed multi-panel design with shaped radiation in both azimuth and elevation may be a plausible alternative.

To further complement the work related above and keep this project alive, some particular tasks are open to be investigated:

- Since V2P communications will also be an essential enabler of safe roads in future cities, link quality and stability of such situations can be studied in realistic scenarios using the given software platform. There, the radiation diagrams of mmWave handsets in presence of pedestrian user can be included to enhance the realism of such results.
- The impact of dynamic of pedestrians in real movement is also an open topic to be studied. The variability of coverage may be very large with small movements of the phone. Also, the investigation of other effects such as micro-Doppler could be of interest.
- In [J1], the algorithm for beam adaptation is based on the use of sharp radiation diagrams in LOS condition, like the one found in highway scenarios. The strategy can be then extended to NLOS situations, where mmWave signals experience severe degradation.

## 7. CONCLUSION

---

- The proposal of DAS for vehicles is numerically validated in urban scenarios and a prototype is tested in a controlled environment. The next step, if an industry partner finds the design interesting enough, is to perform field trials of real V2X communications and compare the performance of such systems when compared to conventional ones.

## REFERENCES

---

- [1] TILEMACHOS DOUKOGLOU, VELISSARIOS GEZERLIS, KONSTANTINOS TRICHIAS, NIKOS KOSTOPOULOS, NIKOS VRAKAS, MARIOS BOUGIOUKOS, AND RODOLPHE LEGOUABLE. **Vertical Industries Requirements Analysis Targeted KPIs for Advanced 5G Trials**. In *2019 European Conference on Networks and Communications (EuCNC)*, pages 95–100, 2019. 1
- [2] DAVID J TEECE. **5G Mobile: Impact on the Health Care Sector**. In *Working paper.*, pages 1–17. Haas School of Business, 2017. 1
- [3] GEORGE DIMITRAKOPOULOS. **Sustainable mobility leveraging on 5G mobile communication infrastructures in the context of smart city operations**. *Evolving Systems*, **8**(2):157–166, 2017. 1
- [4] KAREN CAMPBELL, JIM DIFFLEY, BOB FLANAGAN, BILL MORELLI, BRENDAN O’NEIL, AND FRANCIS SIDECO. **The 5G economy: How 5G technology will contribute to the global economy**. *IHS Economics and IHS Technology*, **4**:16, 2017. 1
- [5] ERIK G. LARSSON, OVE EDFORS, FREDRIK TUFVESSON, AND THOMAS L. MARZETTA. **Massive MIMO for next generation wireless systems**. *IEEE Communications Magazine*, **52**(2):186–195, 2014. 2
- [6] E SO ROSENBLUM. *Atmospheric Absorption of 10-400 KMcps Radiation: Summary and Bibliography to 1960*. Massachusetts Institute of Technology, Lincoln Laboratory, 1960. 2, 3, 23
- [7] H. T. FRIIS. **A Note on a Simple Transmission Formula**. *Proceedings of the IRE*, **34**(5):254–256, May 1946. 2

## REFERENCES

---

- [8] SRIDHAR RAJAGOPAL, SHADI ABU-SURRA, AND MEHRZAD MALMIRCHEGINI. **Channel Feasibility for Outdoor Non-Line-of-Sight mmWave Mobile Communication.** In *2012 IEEE Vehicular Technology Conference (VTC Fall)*, pages 1–6, 2012. 2
- [9] ABDELBASSET BEDDA ZEKRI, RIADH AJGOU, ALI CHEMSA, AND SAID GHENDIR. **Analysis of Outdoor to Indoor Penetration Loss for mmWave Channels.** In *2020 1st International Conference on Communications, Control Systems and Signal Processing (CCSSP)*, pages 74–79, 2020. 2
- [10] LAURI VÄHÄ-SAVO, ALEJANDRA GARRIDO ATIENZA, CHRISTIAN CZIEZERSKI, MIKKO HEINO, KATSUYUKI HANEDA, CLEMENS ICHELN, XIAOSHU LÜ, AND KLAUS VILJANEN. **Passive Antenna Systems Embedded into a Load Bearing Wall for Improved Radio Transparency.** In *2020 50th European Microwave Conference (EuMC)*, pages 424–427, 2021. 2
- [11] ÁNGEL CARDAMA, JORDI ROMEU, JUAN MANUEL RIUS, LLUÍS JOFRE, SEBASTIÁN BLANCH, AND MIGUEL FERRANDO. *Antenas.* Univ. Politèc. de Catalunya, 2004. 2
- [12] R.W. SAUNDERS, T.J. HEWISON, S.J. STRINGER, AND N.C. ATKINSON. **The radiometric characterization of AMSU-B.** *IEEE Transactions on Microwave Theory and Techniques*, **43**(4):760–771, 1995. 3
- [13] D.M. SHEEN, D.L. MCMAKIN, AND T.E. HALL. **Three-dimensional millimeter-wave imaging for concealed weapon detection.** *IEEE Transactions on Microwave Theory and Techniques*, **49**(9):1581–1592, 2001. 3
- [14] MARTIN SCHNEIDER. **Automotive Radar – Status and Trends.** In *German microwave conference*, pages 144–147, 2005. 3
- [15] 3GPP. **Technical Specification Group Radio Access Network; NR; Base Station (BS) radio transmission and reception (Release 16).** Technical Specification (TS) 38.104, 3rd Generation Partnership Project (3GPP), Sep 2020. Version 16.5.0. 4, 18, 19
- [16] C. F. MECKLENBRAUKER, A. F. MOLISCH, J. KAREDAL, F. TUFVESSON, A. PAIER, L. BERNADO, T. ZEMEN, O. KLEMP, AND N. CZINK. **Vehicular**

- Channel Characterization and Its Implications for Wireless System Design and Performance.** *Proceedings of the IEEE*, **99**(7):1189–1212, July 2011. 4
- [17] GRUPO DEL ESPECTRO DEL COIT. **Modulación y multiacceso en 5G.** Technical report, Colegio Oficial de Ingenieros de Telecomunicación, 2018. 4
- [18] ALI ZAIDI, FREDRIK ATHLEY, JONAS MEDBO, ULF GUSTAVSSON, GIUSEPPE DURISI, AND XIAOMING CHEN. *5G Physical Layer: Principles, Models and Technology Components.* Academic Press, 2018. 4
- [19] JINGXIAN WU AND PINGZHI FAN. **A Survey on High Mobility Wireless Communications: Challenges, Opportunities and Solutions.** *IEEE Access*, **4**:450–476, 2016. 5
- [20] CHEN-NEE CHUAH, D. N. C. TSE, J. M. KAHN, AND R. A. VALENZUELA. **Capacity scaling in MIMO wireless systems under correlated fading.** *IEEE Transactions on Information Theory*, **48**(3):637–650, Mar 2002. 5
- [21] GERARD J FOSCHINI AND MICHAEL J GANS. **On limits of wireless communications in a fading environment when using multiple antennas.** *Wireless personal communications*, **6**(3):311–335, 1998. 5
- [22] IRFAN AHMED, HEDI KHAMMARI, ADNAN SHAHID, AHMED MUSA, KWANG SOON KIM, ELI DE POORTER, AND INGRID MOERMAN. **A Survey on Hybrid Beamforming Techniques in 5G: Architecture and System Model Perspectives.** *IEEE Communications Surveys & Tutorials*, **20**(4):3060–3097, 2018. 6
- [23] ANDREAS PFADLER, CHRISTIAN BALLESTEROS, JORDI ROMEU, AND LLUIS JOFRE. **Hybrid Massive MIMO for Urban V2I: Sub-6 GHz vs mmWave Performance Assessment.** *IEEE Transactions on Vehicular Technology*, **69**(5):4652–4662, 2020. 6
- [24] P. PETRUS, J. H. REED, AND T. S. RAPPAPORT. **Effects of directional antennas at the base station on the Doppler spectrum.** *IEEE Communications Letters*, **1**(2):40–42, 1997. 6

## REFERENCES

---

- [25] S. J. NAWAZ, N. M. KHAN, M. N. PATWARY, AND M. MONIRI. **Effect of Directional Antenna on the Doppler Spectrum in 3-D Mobile Radio Propagation Environment.** *IEEE Transactions on Vehicular Technology*, **60**(7):2895–2903, 2011. 6
- [26] K. GUAN, B. AI, B. PENG, D. HE, G. LI, J. YANG, Z. ZHONG, AND T. KÜRNER. **Towards Realistic High-Speed Train Channels at 5G Millimeter-Wave Band—Part I: Paradigm, Significance Analysis, and Scenario Reconstruction.** *IEEE Transactions on Vehicular Technology*, **67**(10):9112–9128, Oct 2018. 6
- [27] J. LORCA, M. HUNUKUMBURE, AND Y. WANG. **On Overcoming the Impact of Doppler Spectrum in Millimeter-Wave V2I Communications.** In *2017 IEEE Globecom Workshops (GC Wkshps)*, pages 1–6, Dec 2017. 6
- [28] INDIAN NATIONAL SCIENCE ACADEMY. *Pursuit and Promotion of Science: The Indian Experience.* Indian National Science Academy, 2001. 10, 11
- [29] A. K. SEN. **Sir J.C. Bose and millimeter waves.** In *TENCON '98. 1998 IEEE Region 10 International Conference on Global Connectivity in Energy, Computer, Communication and Control*, **2**, pages 288–290 vol.2, 1998. 10
- [30] JAMES CLERK MAXWELL. **II. A dynamical theory of the electromagnetic field.** *Proceedings of the Royal Society of London*, (13):531–536, 1864. 10
- [31] HEINRICH HERTZ. *Electric waves: being researches on the propagation of electric action with finite velocity through space.* Dover Publications, 1893. 10
- [32] D. T. EMERSON. **The Work of Jagadis Chandra Bose: 100 Years of MM-Wave Research.** In *International Microwave Symposium Digest*, **2**, pages 553–556. IEEE MTT-S, 1997. 11
- [33] EF NICHOLS AND JD TEAR. **Short electric waves.** *Physical Review*, **21**(6):587, 1923. 11
- [34] JD TEAR. **The optical constants of certain liquids for short electric waves.** *Physical Review*, **21**(6):611, 1923. 11
- [35] CLAUD EDWIN CLEETON AND NEIL HOOKER WILLIAMS. **Electromagnetic waves of 1.1 cm wave-length and the absorption spectrum of ammonia.** *Physical Review*, **45**(4):234, 1934. 11



- 
- [36] JW DEES, JL KING, AND JC WILTSE. **A millimeter wave propagation experiment from the ATS-E spacecraft.** *Technical Report*, 1968. 12
- [37] PD CURTIS, GD PESKETT, AND CD RODGERS. **Remote sounding of atmospheric temperature from satellites V. The pressure modulator radiometer for Nimbus F.** *Proc. R. Soc. Lond. A*, **337**(1608):135–150, 1974. 12
- [38] EUROPEAN COMMISSION. **The Future of Cities.** [Online]. Available: <https://urban.jrc.ec.europa.eu/thefutureofcities/mobility> [Accessed: Aug. 08, 2021]. 12
- [39] EIT URBAN MOBILITY. **‘Mobility Talks’ episode 5: Mobility as a Service, disrupting mobility in the cities!** [Online]. Available: <https://www.eiturbanmobility.eu/events/mobility-talks-episode-5-mobility-as-a-service-disrupting-urban-mobility-in-the-cities> [Accessed: Aug. 08, 2021]. 12
- [40] OBSERVATORIO DEL TRANSPORTE Y LA LOGÍSTICA EN ESPAÑA. **Movilidad Urbana y Metropolitana: Un gran reto de las ciudades del siglo XXI.** Technical report, Ministerio de Transportes, Movilidad y Agenda Urbana, Jan 2020. 12
- [41] EUROSTAT. **Majority commuted less than 30 minutes in 2019 .** [Online]. Available: <https://ec.europa.eu/eurostat/web/products-eurostat-news/-/DDN-20201021-2> [Accessed: Aug. 08, 2021]. 12
- [42] EUROSTAT. **Energy, Transport and Environment Statistics .** Technical report, European Commission, Oct 2020. 12
- [43] M ALONSO RAPOSO, M GROSSO, J DESPRÉS, E FERNÁNDEZ MACÍAS, C GALASSI, A KRASENBRINK, J KRAUSE, L LEVATI, A MOURTZOUCHOU, B SAVEYN, ET AL. **An analysis of possible socio-economic effects of a Cooperative, Connected and Automated Mobility (CCAM) in Europe.** *European Union*, 2018. 13
- [44] ANASTASIOS TSAKALIDIS AND CHRISTIAN THIEL. **Electric vehicles in Europe from 2010 to 2017: is full-scale commercialisation beginning.** *Joint Research Centre*, 2018. 13
- [45] 3GPP. **Technical Specification Group Services and System Aspects; Enhancement of 3GPP support for V2X scenarios; Stage 1 (Release 16).**

## REFERENCES

---

- Technical Specification (TS) 22.186, 3rd Generation Partnership Project (3GPP), Jun 2019. Version 16.3.0. 14
- [46] MATE BOBAN, APOSTOLOS KOUSARIDAS, KONSTANTINOS MANOLAKIS, JOSEF EICHINGER, AND WEN XU. **Connected roads of the future: Use cases, requirements, and design considerations for vehicle-to-everything communications.** *IEEE vehicular technology magazine*, **13**(3):110–123, 2018. 14
- [47] 5GAA. **C-V2X Use Cases: Methodology, Examples and Service Level Requirements.** White Paper 102 638, 5G Automotive Association (5GAA), Jun 2019. Version 1.0. 14
- [48] GMDT FORECAST ET AL. **Cisco visual networking index: global mobile data traffic forecast update, 2017–2022.** *Update, 2017:2022*, 2019. 14, 15
- [49] SUNDEEP RANGAN, THEODORE S RAPPAPORT, AND ELZA ERKIP. **Millimeter-Wave Cellular Wireless Networks: Potentials and Challenges.** *Proceedings of the IEEE*, **102**(3):366–385, 2014. 15
- [50] JAE-HYUN LEE, JEONG-SIK CHOI, AND SEONG-CHEOL KIM. **Cell Coverage Analysis of 28 GHz Millimeter Wave in Urban Microcell Environment Using 3-D Ray Tracing.** *IEEE Transactions on Antennas and Propagation*, **66**(3):1479–1487, 2018. 15
- [51] MURTAZA AHMED SIDDIQI, HEEJUNG YU, AND JINGON JOUNG. **5G Ultra-Reliable Low-Latency Communication Implementation Challenges and Operational Issues with IoT Devices.** *Electronics*, **8**(9), 2019. 15, 16
- [52] RADIOCOMMUNICATION SECTOR OF ITU (ITU-R). **IMT Vision — Framework and Overall Objectives of the Future Development of IMT for 2020 and Beyond.** May 2020. 17
- [53] GSM ASSOCIATION. *The 5G Guide – A Reference for Operators*, Apr 2019. 17
- [54] 3GPP. **Technical Specification Group Radio Access Network; NR; Physical channels and modulation (Release 16).** Technical Specification (TS) 38.211, 3rd Generation Partnership Project (3GPP), Jun 2021. Version 16.6.0. 17, 18, 19, 24, 25

- 
- [55] 3GPP. **Technical Specification Group Radio Access Network; NR; User Equipment (UE) radio transmission and reception; Part 1: Range 1 Standalone (Release 16)**. Technical Specification (TS) 38.101-1, 3rd Generation Partnership Project (3GPP), Sep 2020. Version 16.5.0. 19
- [56] 3GPP. **Technical Specification Group Radio Access Network; NR; Base Station (BS) radio transmission and reception; Part 2: Range 2 Standalone (Release 16)**. Technical Specification (TS) 38.101-2, 3rd Generation Partnership Project (3GPP), Sep 2020. Version 16.5.0. 19
- [57] EUROPEAN COMMISSION. **Action Plan for the Deployment of Intelligent Transport Systems in Europe, COM(2008) 886**. Technical report, European Union, Dec 2008. 19
- [58] FCC. **Report and Order FCC 03-324**. Technical report, Federal Communications Commission (FCC), Dec 2003. 20
- [59] YUMING GE, XIAOMAN LIU, LIBO TANG, AND DARRELL M WEST. **Smart transportation in China and the United States**. *Center for Technology Innovation*, Dec 2017. 20
- [60] ETSI EN ETSI. **302 665 v1. 1.1: Intelligent transport systems (its), communications architecture**. Technical report, Sep 2010. 20
- [61] VT/ITS INTELLIGENT TRANSPORTATION SYSTEMS COMMITTEE. **IEEE 1609.0-2019 - IEEE Guide for Wireless Access in Vehicular Environments (WAVE) Architecture**, 2019. 20
- [62] LUCA MONTERO. **V2X Communications for Connected and Automated Vehicles: an application-centered review**. Aug 2018. 20
- [63] 3GPP. **Technical Specification Group Services and System Aspects; Study on enhancement of 3GPP Support for 5G V2X Services (Release 16)**. Technical Report (TR) 22.886, 3rd Generation Partnership Project (3GPP), Dec 2018. Version 16.2.0. 21
- [64] GAURANG NAIK, BIPLAV CHOUDHURY, AND JUNG-MIN PARK. **IEEE 802.11bd amp; 5G NR V2X: Evolution of Radio Access Technologies for V2X Communications**. *IEEE Access*, 7:70169–70184, 2019. 21

## REFERENCES

---

- [65] RADIOCOMMUNICATION SECTOR OF ITU (ITU-R). **Intelligent transport systems - Dedicated short range communications at 5.8 GHz**. Jun 2005. 22
- [66] JUNSUNG CHOI, VUK MAROJEVIC, CARL B. DIETRICH, JEFFREY H. REED, AND SEUNGYOUNG AHN. **Survey of Spectrum Regulation for Intelligent Transportation Systems**. *IEEE Access*, 8:140145–140160, 2020. 22
- [67] SOHAN GYAWALI, SHENGJIE XU, YI QIAN, AND ROSE QINGYANG HU. **Challenges and solutions for cellular based v2x communications**. *IEEE Communications Surveys & Tutorials*, 2021. 22
- [68] 5G AUTOMOTIVE ASSOCIATION. **Petition For Waiver to Allow Deployment of Intelligent Transportation System Cellular Vehicle to Everything (C-V2X) Technology**, Nov 2018. Proceeding GN 18-357. 22
- [69] SEBASTIAN EULER, ANDREAS PFADLER, LUIS FERNÁNDEZ FERREIRA, AND HONGXIA ZHAO. **Spectrum Needs of Cooperative, Connected and Automated Mobility**. In *2021 IEEE 93rd Vehicular Technology Conference (VTC2021-Spring)*, pages 1–6, 2021. 22
- [70] MARCO GIORDANI, ANDREA ZANELLA, AND MICHELE ZORZI. **Millimeter wave communication in vehicular networks: Challenges and opportunities**. In *2017 6th International Conference on Modern Circuits and Systems Technologies (MOCAST)*, pages 1–6, 2017. 22, 23
- [71] BALDOMERO COLL-PERALES, MARCO GRUTESER, AND JAVIER GOZALVEZ. **Evaluation of IEEE 802.11ad for mmWave V2V communications**. In *2018 IEEE Wireless Communications and Networking Conference Workshops (WCNCW)*, pages 290–295, 2018. 23
- [72] WOOSEONG KIM. **Experimental demonstration of MmWave vehicle-to-vehicle communications using IEEE 802.11 ad**. *Sensors*, 19(9):2057, 2019. 23
- [73] YASAMAN GHASEMPOUR, CLAUDIO R. C. M. DA SILVA, CARLOS CORDEIRO, AND EDWARD W. KNIGHTLY. **IEEE 802.11ay: Next-Generation 60 GHz Communication for 100 Gb/s Wi-Fi**. *IEEE Communications Magazine*, 55(12):186–192, 2017. 23

- 
- [74] OMID SEMIARI, WALID SAAD, MEHDI BENNIS, AND MEROUANE DEBBAH. **Integrated Millimeter Wave and Sub-6 GHz Wireless Networks: A Roadmap for Joint Mobile Broadband and Ultra-Reliable Low-Latency Communications.** *IEEE Wireless Communications*, **26**(2):109–115, 2019. 23
- [75] JUNIL CHOI, VUTHA VA, NURIA GONZALEZ-PRELCIC, ROBERT DANIELS, CHANDRA R. BHAT, AND ROBERT W. HEATH. **Millimeter-Wave Vehicular Communication to Support Massive Automotive Sensing.** *IEEE Communications Magazine*, **54**(12):160–167, 2016. 23, 24
- [76] TUNCER BAYKAS, CHIN-SEAN SUM, ZHOU LAN, JUNYI WANG, M. AZIZUR RAHMAN, HIROSHI HARADA, AND SHUZO KATO. **IEEE 802.15.3c: the first IEEE wireless standard for data rates over 1 Gb/s.** *IEEE Communications Magazine*, **49**(7):114–121, 2011. 23
- [77] SOOYOUNG HUR, TAEJOON KIM, DAVID J. LOVE, JAMES V. KROGMEIER, TIMOTHY A. THOMAS, AND AMITAVA GHOSH. **Millimeter Wave Beamforming for Wireless Backhaul and Access in Small Cell Networks.** *IEEE Transactions on Communications*, **61**(10):4391–4403, 2013. 23
- [78] IFTIKHAR RASHEED, FEI HU, YANG-KI HONG, AND BHARAT BALASUBRAMANIAN. **Intelligent Vehicle Network Routing With Adaptive 3D Beam Alignment for mmWave 5G-Based V2X Communications.** *IEEE Transactions on Intelligent Transportation Systems*, **22**(5):2706–2718, 2021. 23
- [79] YIJIA FENG, DAZHI HE, YUNFENG GUAN, YIHANG HUANG, YIN XU, AND ZHIYONG CHEN. **Beamwidth Optimization for Millimeter-Wave V2V Communication Between Neighbor Vehicles in Highway Scenarios.** *IEEE Access*, **9**:4335–4350, 2021. 23
- [80] NIL GARCIA, HENK WYMEERSCH, ERIK G. STRÖM, AND DIRK SLOCK. **Location-aided mm-wave channel estimation for vehicular communication.** In *2016 IEEE 17th International Workshop on Signal Processing Advances in Wireless Communications (SPAWC)*, pages 1–5, 2016. 24
- [81] FLAVIO MASCHIETTI, DAVID GESBERT, PAUL DE KERRET, AND HENK WYMEERSCH. **Robust location-aided beam alignment in millimeter wave massive MIMO.** In *GLOBECOM 2017-2017 IEEE Global Communications Conference*, pages 1–6. IEEE, 2017. 24

## REFERENCES

---

- [82] FAN LIU, WEIJIE YUAN, CHRISTOS MASOUIROS, AND JINHONG YUAN. **Radar-assisted predictive beamforming for vehicular links: Communication served by sensing.** *arXiv preprint arXiv:2001.09306*, 2020. 24
- [83] JUNYI WANG, ZHOU LAN, CHANG WOO PYO, T. BAYKAS, CHIN SEAN SUM, M.A. RAHMAN, JING GAO, R. FUNADA, F. KOJIMA, H. HARADA, AND S. KATO. **Beam codebook based beamforming protocol for multi-Gbps millimeter-wave WPAN systems.** *IEEE Journal on Selected Areas in Communications*, **27**(8):1390–1399, 2009. 24
- [84] P. XIA AND C. NGO. **System and method for multi-stage antenna training of beamforming vectors**, Apr. 2012. U.S. Patent 8 165 595 B2. 24
- [85] IEEE. **IEEE Standard for Information Technology – Telecommunications and Information Exchange between Systems – Local and Metropolitan Area Networks – Specific Requirements. Part 15.3: Wireless Medium Access Control (MAC) and Physical Layer (PHY) Specifications for High Rate Wireless Personal Area Networks (WPANs) Amendment 2: Millimeter-Wave-Based Alternative Physical Layer Extension**, Oct. 2009. 24
- [86] SUNG-EN CHIU, NANCY RONQUILLO, AND TARA JAVIDI. **Active Learning and CSI Acquisition for mmWave Initial Alignment.** *IEEE Journal on Selected Areas in Communications*, **37**(11):2474–2489, 2019. 24
- [87] HOSSEIN SOLEIMANI, RAUL PARADA, STEFANO TOMASIN, AND MICHELE ZORZI. **Fast Initial Access for mmWave 5G Systems with Hybrid Beamforming Using Online Statistics Learning.** *IEEE Communications Magazine*, **57**(9):132–137, 2019. 24
- [88] IRMAK AYKIN AND MARWAN KRUNZ. **Efficient Beam Sweeping Algorithms and Initial Access Protocols for Millimeter-Wave Networks.** *IEEE Transactions on Wireless Communications*, **19**(4):2504–2514, 2020. 24
- [89] TAKAYUKI SHIMIZU, VUTHA VA, GAURAV BANSAL, AND ROBERT W HEATH. **Millimeter wave V2X communications: Use cases and design considerations of beam management.** In *2018 Asia-Pacific Microwave Conference (APMC)*, pages 183–185. IEEE, 2018. 24

## REFERENCES

---

- [90] LUCA MONTERO, CHRISTIAN BALLESTEROS, CESAR DE MARCO, AND LUIS JOFRE. **Beam management for vehicle-to-vehicle (V2V) communications in millimeter wave 5G.** *Vehicular Communications*, page 100424, 2021. 24
- [91] MARIO H. CASTAÑEDA GARCIA, ALEJANDRO MOLINA-GALAN, MATE BOBAN, JAVIER GOZALVEZ, BALDOMERO COLL-PERALES, TAYLAN ŞAHIN, AND APOSTOLOS KOUSARIDAS. **A Tutorial on 5G NR V2X Communications.** *IEEE Communications Surveys Tutorials*, **23**(3):1972–2026, 2021. 25
- [92] KATSUYUKI HANEDA, JIANHUA ZHANG, LEI TAN, GUANGYI LIU, YI ZHENG, HENRIK ASPLUND, JIAN LI, YI WANG, DAVID STEER, CLARA LI, TOMMASO BALERCIA, SUNGUK LEE, YOUNGSUK KIM, AMITAVA GHOSH, TIMOTHY THOMAS, TAKEHIRO NAKAMURA, YUICHI KAKISHIMA, TETSURO IMAI, HARALABOS PAPADOPOULOS, THEODORE S. RAPPAPORT, GEORGE R. MACCARTNEY, MATHEW K. SAMIMI, SHU SUN, OZGE KOYMEN, SOOYOUNG HUR, JEONGHO PARK, CHARLIE ZHANG, EVANGELOS MELLIOS, ANDREAS F. MOLISCH, SAEED S. GHASSAMZADEH, AND ARUN GHOSH. **5G 3GPP-Like Channel Models for Outdoor Urban Microcellular and Macrocellular Environments.** In *2016 IEEE 83rd Vehicular Technology Conference (VTC Spring)*, pages 1–7, 2016. 28
- [93] 3GPP. **Study on channel model for frequencies from 0.5 to 100 GHz (release 16).** TR 38.901 (V16.1.0), 3rd Generation Partnership Project (3GPP), Dec. 2019. 28, 82
- [94] R. HADANI, S. RAKIB, M. TSATSANIS, A. MONK, A. J. GOLDSMITH, A. F. MOLISCH, AND R. CALDERBANK. **Orthogonal Time Frequency Space Modulation.** In *2017 IEEE Wireless Communications and Networking Conference (WCNC)*, pages 1–6, 2017. 28
- [95] ANDREAS PFADLER, PETER JUNG, TOM SZOLLMANN, AND SLAWOMIR STANCZAK. **Pulse-Shaped OTFS over Doubly-Dispersive Channels: One-Tap vs. Full LMMSE Equalizers.** In *2021 IEEE International Conference on Communications Workshops (ICC Workshops)*, pages 1–6, 2021. 28
- [96] P. BELLO. **Characterization of Randomly Time-Variant Linear Channels.** *IEEE Transactions on Communications Systems*, **11**(4):360–393, 1963. 28

## REFERENCES

---

- [97] PABLO ALVAREZ LOPEZ, MICHAEL BEHRISCH, LAURA BIEKER-WALZ, JAKOB ERDMANN, YUN-PANG FLÖTTERÖD, ROBERT HILBRICH, LEONHARD LÜCKEN, JOHANNES RUMMEL, PETER WAGNER, AND EVAMARIE WIESSNER. **Microscopic Traffic Simulation using SUMO**. In *The 21st IEEE International Conference on Intelligent Transportation Systems*. IEEE, 2018. 30
- [98] STEPHAN JAECKEL, LESZEK RASCHKOWSKI, KAI BÖRNER, AND LARS THIELE. **QuaDRiGa: A 3-D multi-cell channel model with time evolution for enabling virtual field trials**. *IEEE Transactions on Antennas and Propagation*, 62(6):3242–3256, 2014. 31
- [99] 3GPP. **Technical Specification Group Radio Access Network; Study on Evaluation Methodology of New Vehicle-to-Everything (V2X) Use Cases for LTE and NR; (Release 15)**. Technical Report (TR) 37.885, 3rd Generation Partnership Project (3GPP), June 2019. Version 15.3.0. 31
- [100] MIUREL TERCERO, PETER VON WRYCZA, ADITYA AMAH, JOERG WIDMER, MARIA FRESIA, VALERIO FRASCOLLA, JAVIER LORCA, TOMMY SVENSSON, MARIE-HÉLÈNE HAMON, SANDRINE DESTOUET ROBLLOT, ET AL. **5G systems: The mmMAGIC project perspective on use cases and challenges between 6–100 GHz**. In *2016 IEEE Wireless Communications and Networking Conference Workshops (WCNCW)*, pages 200–205. IEEE, 2016. 31
- [101] X. YIN AND X. CHENG. *Propagation Channel Characterization, Parameter Estimation, and Modeling for Wireless Communications*. John Wiley & Sons, 1st edition, 2015. 32
- [102] FRAUNHOFER HEINRICH HERTZ INSTITUTE. *Quasi Deterministic Radio Channel Generator User Manual and Documentation*, July 2021. Document Revision v2.6.1. 34, 39
- [103] HANBYUL SEO AND BYEONG GI LEE. **A proportional-fair power allocation scheme for fair and efficient multiuser OFDM systems**. In *IEEE Global Telecommunications Conference, 2004. GLOBECOM'04.*, 6, pages 3737–3741. IEEE, 2004. 41



- 
- [104] T. WU, T. S. RAPPAPORT, AND C. M. COLLINS. **The human body and millimeter-wave wireless communication systems: Interactions and implications.** In *2015 IEEE International Conference on Communications (ICC)*, pages 2423–2429, June 2015. 65, 66, 68
- [105] ICNIRP. **Guidelines for limiting exposure to time-varying electric, magnetic, and electromagnetic fields (up to 300 GHz).** *Health phys*, **74**(4):494–522, 1998. 66
- [106] D. COLOMBI, B. THORS, AND C. TÖRNEVIK. **Implications of EMF Exposure Limits on Output Power Levels for 5G Devices Above 6 GHz.** *IEEE Antennas and Wireless Propagation Letters*, **14**:1247–1249, 2015. 66
- [107] K. ZHAO, J. HELANDER, D. SJÖBERG, S. HE, T. BOLIN, AND Z. YING. **User Body Effect on Phased Array in User Equipment for the 5G mmWave Communication System.** *IEEE Antennas and Wireless Propagation Letters*, **16**:864–867, 2017. 66
- [108] I. SYRYTSIN, S. ZHANG, AND G. F. PEDERSEN. **User Impact on Phased and Switch Diversity Arrays in 5G Mobile Terminals.** *IEEE Access*, **6**:1616–1623, 2018. 66
- [109] R. RODRÍGUEZ-CANO, S. ZHANG, K. ZHAO, AND G. F. PEDERSEN. **User Body Interaction of 5G Switchable Antenna System for Mobile Terminals at 28 GHz.** In *2019 13th European Conference on Antennas and Propagation (EuCAP)*, pages 1–4, March 2019. 66
- [110] S. ZHANG, X. CHEN, I. SYRYTSIN, AND G. F. PEDERSEN. **A Planar Switchable 3-D-Coverage Phased Array Antenna and Its User Effects for 28-GHz Mobile Terminal Applications.** *IEEE Transactions on Antennas and Propagation*, **65**(12):6413–6421, Dec 2017. 66
- [111] X. CHEN, L. TIAN, P. TANG, AND J. ZHANG. **Modelling of Human Body Shadowing Based on 28 GHz Indoor Measurement Results.** In *2016 IEEE 84th Vehicular Technology Conference (VTC-Fall)*, pages 1–5, Sep. 2016. 66
- [112] J. HEJSELBÆK, J. Ø. NIELSEN, W. FAN, AND G. F. PEDERSEN. **Measured 21.5 GHz Indoor Channels With User-Held Handset Antenna Array.** *IEEE Transactions on Antennas and Propagation*, **65**(12):6574–6583, Dec 2017. 66

## REFERENCES

---

- [113] M. HEINO, C. ICHELN, AND K. HANEDA. **Finger effect on 60 GHz user device antennas.** In *2016 10th European Conference on Antennas and Propagation (EuCAP)*, pages 1–5, April 2016. 66
- [114] R. KHAN, A. A. AL-HADI, AND P. J. SOH. **User effect on the efficiency of 4-port mobile terminal antenna at 28 GHz.** In *2017 International Symposium on Antennas and Propagation (ISAP)*, pages 1–2, Oct 2017. 66
- [115] C. GUSTAFSON AND F. TUFVESSON. **Characterization of 60 GHz shadowing by human bodies and simple phantoms.** In *2012 6th European Conference on Antennas and Propagation (EUCAP)*, pages 473–477, March 2012. 66
- [116] S. L. COTTON. **Human Body Shadowing in Cellular Device-to-Device Communications: Channel Modeling Using the Shadowed  $\kappa - \mu$  Fading Model.** *IEEE Journal on Selected Areas in Communications*, **33**(1):111–119, Jan 2015. 67
- [117] T. CHOI, C. U. BAS, R. WANG, S. HUR, J. PARK, J. ZHANG, AND A. F. MOLISCH. **Measurement Based Directional Modeling of Dynamic Human Body Shadowing at 28 GHz.** In *2018 IEEE Global Communications Conference (GLOBECOM)*, pages 1–6, Dec 2018. 67
- [118] M. HEINO, C. ICHELN, AND K. HANEDA. **Self-user shadowing effects of millimeter-wave mobile phone antennas in a browsing mode.** In *2019 13th European Conference on Antennas and Propagation (EuCAP)*, pages 1–5, March 2019. 67
- [119] MakeHuman. *MakeHuman 1.1.1*, 2017. 67
- [120] Blender Foundation. *Blender 2.79b*, 2017. 67
- [121] Dassault Systèmes. *CST Studio Suite 2019*, 2019. 67
- [122] O. P. GANDHI AND A. RIAZI. **Absorption of Millimeter Waves by Human Beings and its Biological Implications.** *IEEE Transactions on Microwave Theory and Techniques*, **34**(2):228–235, Feb 1986. 68
- [123] P.A. HASGALL, F. DI GENNARO, C. BAUMGARTNER, E. NEUFELD, B. LLOYD, M.C. GOSSELIN, D. PAYNE, A. KLINGENBÖCK, AND N. KUSTER. **IT’IS Database for thermal and electromagnetic parameters of biological tissues**, May 2018. Version 4.0. 68

## REFERENCES

---

- [124] NACER CHAHAT, MAXIM ZHADOBOV, STANISLAV ALEKSEEV, AND RONAN SAULEAU. **Human skin-equivalent phantom for on-body antenna measurements in 60 GHz band.** *Electronics letters*, **48**(2):67–68, 2012. 71, 72
- [125] LAURI VÄHÄ-SAVO, CHRISTIAN CZIEZERSKI, MIKKO HEINO, KATSUYUKI HANEDA, CLEMENS ICHELN, ALI HAZMI, AND RUIYUAN TIAN. **Empirical evaluation of a 28 GHz antenna array on a 5G mobile phone using a body phantom.** *IEEE Transactions on Antennas and Propagation*, **69**(11):7476–7485, 2021. 71, 72
- [126] RADIM ZAJICEK, LADISLAV OPPL, AND JAN VRBA. **Broadband Measurement of Complex Permittivity using Reflection Method and Coaxial Probes.** *Radioengineering*, **17**(1):14–19, 2008. 71
- [127] KENNETH S. COLE AND ROBERT H. COLE. **Dispersion and Absorption in Dielectrics I. Alternating Current Characteristics.** *The Journal of Chemical Physics*, **9**(4):341–351, 1941. 71
- [128] S GABRIEL, R W LAU, AND C GABRIEL. **The dielectric properties of biological tissues: III. Parametric models for the dielectric spectrum of tissues.** *Physics in Medicine and Biology*, **41**(11):2271–2293, nov 1996. 71, 72
- [129] 5GAA. **Distributed Vehicular Antenna Systems.** Technical Report (TR), 5G Automotive Association, 01 2022. Version 1.0. 82